Distribution Agreement

In presenting this thesis or dissertation as a partial fulfillment of the requirements for an advanced degree from Emory University, I hereby grant to Emory University and its agents the non-exclusive license to archive, make accessible, and display my thesis or dissertation in whole or in part in all forms of media, now or hereafter known, including display on the world wide web. I understand that I may select some access restrictions as part of the online submission of this thesis or dissertation. I retain all ownership rights to the copyright of the thesis or dissertation. I also retain the right to use in future works (such as articles or books) all or part of this thesis or dissertation.

Signature:

_____ _____

Satya Spandana Boddu Date

Identifying the Sources of Variation in Host-Associated Microbiomes Using *Caenorhabditis elegans*

By

Satya Spandana Boddu
Doctor of Philosophy

Physics

Nic Vega, Ph.D.
Co-Advisor

Ilya Nemenman, Ph.D.
Co-Advisor

Minsu Kim, Ph.D.
Committee Member

Hang Lu, Ph.D.
Committee Member

Daniel Weissman, Ph.D.
Committee Member

Accepted:

Kimberly Jacob Arriola, Ph.D.
Dean of the James T. Laney School of Graduate Studies

Date

Identifying the Sources of Variation in Host-Associated Microbiomes Using *Caenorhabditis elegans*

By

Satya Spandana Boddu
B.S., Indian Institute of Science Education & Research, Mohali, 2017
M.S., Indian Institute of Science Education & Research, Mohali, 2017

Advisors: Nic Vega, Ph.D.and Ilya Nemenman, Ph.D.

An abstract of
A dissertation submitted to the Faculty of the
James T. Laney School of Graduate Studies of Emory University
in partial fulfillment of the requirements for the degree of
Doctor of Philosophy
in Physics
2024

Abstract

Identifying the Sources of Variation in Host-Associated Microbiomes Using *Caenorhabditis elegans*

By Satya Spandana Boddu

Microbiome, often referred to as the "forgotten organ", plays a significant role in the health and functionality of its hosts. These collectives of microbes show variation across different host species, among individuals in a population and even within individuals over time. This dissertation quantifies this variation in the gut bacterial load using *Caenorhabditis elegans* model system through experimental and mathematical approaches. The goal is to understand the dynamics and drivers of inter-individual variation in gut microbiome composition. First, I introduce a high-throughput protocol for accurate single-worm bacterial load measurement, revealing the hidden heterogeneity among worms exposed to the same bacterial inoculum. Then, I discuss the challenges in bacterial quantification using colony forming units (CFUs) by extending the Most Probable Number (MPN) method and providing a new formula for combining dilution counts improving accuracy. Finally, I investigate the inter-individual variation across hosts through mono-colonization of individual nematode worms by focusing on the *C. elegans* model. This research advances our understanding of the role of host-microbe interaction in variation in microbiome composition.

Identifying the Sources of Variation in Host-Associated Microbiomes Using *Caenorhabditis elegans*

By

Satya Spandana Boddu
B.S., Indian Institute of Science Education & Research, Mohali, 2017
M.S., Indian Institute of Science Education & Research, Mohali, 2017

Advisors: Nic Vega, Ph.D.and Ilya Nemenman, Ph.D.

A dissertation submitted to the Faculty of the
James T. Laney School of Graduate Studies of Emory University
in partial fulfillment of the requirements for the degree of
Doctor of Philosophy
in Physics
2024

"మండే కొలిమినడగందే – తెలియదే మన్నుకాదు ఇది స్వర్ణమంటూ చూపాలంటే..
పండే పాలము చెబుతుందే – పదునుగా నాటే నాగలి పోటే చేసిన మేలంటే"

"పసిడి పతకాల హారం కాదురా విజయ తీరం..
ఆటనే మాటకర్థం నిను నువ్వే గెలుచు యుద్ధం"

"అల్లాదీన్ అద్భుత దీపం అవసరమే లేదంట, చల్లారని నీ సంకల్పం తోడుంటే చాలంట"

– 'సిరివెన్నెల' సీతారామశాస్త్రి

"కాల్చొద్దు అంటే కాదు స్వర్ణం..
ఓడొద్దు అంటే లేదు యుద్ధం..
లేకుంటే కష్టం హాయి వ్యర్థం..
ఎవరి కోసం మారదర్థం"

– కృష్ణకాంత్

Acknowledgments

When I embarked upon my PhD in 2018 in a new country, I had no idea of the experiences and challenges that lay ahead. Now, as I am at the finish line, I realize that this long journey would not have been manageable without the support of many people to whom I am deeply grateful.

First, I want to thank my co-advisors, Nic Vega and Ilya Nemenman. When I first joined the Vega Lab, everything around me intimidated me. Nic's patience in answering every biology question I had and their encouragement during many failed experiments kept me going. Every scientific conversation with Ilya reminded me why I love physics in the first place and beyond the science, I am grateful for our personal conversations during tough times and his empathy. I also want to thank K. Michael Martini for his significant contributions to my research and mentorship throughout my PhD. I am grateful to my committee members: Minsu Kim, Hang Lu, and Daniel Weissman, for their time and diverse expertise on my dissertation.

I am thankful to the Vega Lab for making me a better biologist than I ever imagined. In particular, I want to thank Jason Chen and Carmen Alvarez for their contributions to my growth as a scientist and a person. I am beyond grateful for our Sunday brunches and coffee-shop rant sessions over the last few years. Even though we all worked on different projects, I always turned to them after every weird result or just about anything and never felt unheard. I cannot imagine getting through the final stages of my dissertation without their advice and camaraderie. I also want to thank the Nemenman Group: Eslam Abdelaleem, Sean Ridout, Arabind Swain, Zehui Zhao, and Ketuna Danelia for all their help with science, coding, and everything else.

I next want to thank my cohort for making me less homesick and my life in the US less scary, especially in the beginning. I want to thank Linnea Bavik and Sahand Emamian for always inspiring me and being a shoulder to lean on. It would not be an exaggeration to say that if not for Linnea's friendship, I would not have survived

Atlanta alone. I learned a lot from her, and I am so grateful to have gone through grad school alongside her. I appreciate being able to talk to Sahand about DEI in science and all the hardships of graduate school without a filter. Some of my most favorite Atlanta memories are the times spent playing Trivia at The Independent with Linnea and Sean on our team, 'All fries go to heaven'. I am thankful for these times away from research, which played a big role in balancing my life during PhD.

I want to thank my longtime friends Ketika Garg and Anuj Pennathur, who went through all this before, for having answers to all my questions and always having space for me at their place when I needed a break. I also want to thank my friends Hakesh Kolukonu, Shreshta Katkuri, Gowtham Malladi, Revanth Gudiseva, Murali Kilaru, Abhishek Biruduraju, Swaroop Nimmagadda and Vineeth Gaddam for supporting me, keeping me up to date with Telugu Cinema news and being my comfort one phone call away. I want to thank Nikhil Kiran Yeso for being an anchor in my life. He believed in me, especially when I didn't, and I am grateful for his cheerleading through two thesis writing stages in my life.

Next, I want to thank my family, particularly my cousins Madhurima Penumarthi, Aishwarya Penumarthi and Manish Babu Nandina, for always being there when I needed them. My nephews, Hasvith Jaii and Shreeyaansh, were a great support and entertainment in the most wholesome and cutest way possible. Finally, I want to thank my mother, Sujatha Gunnam and father, Subrahmanyeswara Rao Boddu for their love and constant support. I would not be here writing this if not for my parents. They sacrificed a lot to provide good education for me, allowing me to pursue my passions, including this degree. I am grateful that I kept going even when things seemed bleak, and I want to acknowledge myself for believing in me.

Contents

List of Figures

List of Tables

Chapter 1

Introduction

Most organisms, including humans, live in conjunction with complex microbial communities known as microbiomes. Microbiomes are composed of a diverse mix of microbes, including bacteria, viruses, fungi, and archaea, which interact with each other and with their host in various ways, including symbiosis and pathogenesis, and affect host health and function [1].

Host-associated microbiomes are complex, dynamic, and non-equilibrium systems [2]. They exhibit significant variation across different host species [3] and among individuals within a population [4, 5]. This variation can be observed in both the composition, which is a measure of the abundance of different microbes present, and the diversity, which refers to the variety of microbial species [4, 6, 7]. Factors contributing to this variation include genetic differences among hosts, environmental perturbations, and even random bacterial birth/death events [8, 9, 10, 11]. Even in the absence of these external factors, individual hosts exhibit variation in microbial composition and the fundamental drivers of this variation, during the microbiome assembly process, are still not completely understood.

Understanding the dynamics and structure of these host-associated microbial communities is crucial because they play a fundamental role in the health and functioning

of their hosts [12, 13, 14, 15]. How identical hosts and microbes collectively give rise to microbiomes that are varied by orders of magnitude and species diversity and yet stably existing is a fundamental question. This dissertation uses a multidisciplinary approach, incorporating concepts from microbiology, ecology, and physics, to bring us closer to solving this question.

1.1 Significance of the Intestinal Microbiome

Although host-associated microbiota can be associated with many body sites [13], here we focus on the intestinal microbiome. Gut microbiomes are associated with many aspects of host health and metabolism, ranging from immunity to behavioral development [12, 13, 14, 15, 16]. Changes in the gut microbiome are linked to several neurological diseases, such as Alzheimer's and Parkinson's, as well as mental health conditions like anxiety and depression [17, 18, 19]. This is thought to occur through the gut-brain axis, where microbial metabolites influence brain function [20, 21]. Furthermore, certain cancers are associated with pathogen-originated mechanisms and microorganism-associated molecular patterns (MAMPs) in the gut, which can trigger inflammation and other immune responses that contribute to disease progression [22]. The composition of the gut microbiome is known to shift with changes in host health, such as during infections or in conditions like obesity [23, 24].

The relationship of host and the intestinal microbiome is thus bi-directional: hosts influence the microbiome while the microbiome, in turn, influences host health as well. Understanding the dynamics of host-microbial communities is hence crucial for addressing dysbiosis (microbial imbalance) and improving host health through therapies such as probiotics, prebiotics, and fecal microbiota transplantation, which aim at restoring healthy microbiome composition [25, 26].

1.2 Structure and Patterns in Host-associated Microbial Communities

Composition of intestinal microbiomes is unique to a host yet variable across different sites within the host and among hosts in a population [6]. Factors such as diet, environmental exposures, and host genetics contribute to this variability [6, 2, 27]. The human gut microbiome, for example, is highly variable within individuals over time, influenced by dietary changes, antibiotic use, and other lifestyle factors [28, 29, 30]. It is also noteworthy that early environmental interactions significantly impact the colonization and development of the gut microbiome [31]. This ever-changing nature of microbiomes results in significant compositional variation among species, among individuals, and within individuals over time.

While the specific composition and abundance of microbial species vary widely between individuals, adding complexity to microbiome structures, there are various signs of host-association. In humans, the number of microbial cells in each microbiome outnumbers human cells, yet most bacterial species belong to a few major phyla, such as Firmicutes, Bacteroidetes, Actinobacteria, and Proteobacteria (Fig. 1.1.b) [5, 6, 28, 32]. The vast diversity and complexity of microbiomes, and how they change as a result of interactions between bacterial species and the host, makes it an interesting system to study.

Advancements in genome sequencing and metagenomic analysis using 16s rRNA data have revolutionized our understanding of microbiomes [32]. These techniques allow for the identification and classification of microbial taxa within microbiomes, as well as assessment of the metabolic potentials encoded within a community.

1.3 Inferring Microbiome Ecology From Data: Top -Down and Bottom-Up Approaches

Despite significant technological advancements in quantifying composition and measuring the diversity of microbiomes, many questions remain regarding the ecology of host-associated microbial communities. Understanding microbial interactions and their temporal dynamics, and how these interactions collectively influence community dynamics and assembly of a microbiome, are some challenges in this regard. To address this challenges, studies can be done in a "top-down" perspective to identify patterns and infer interactions by analyzing large-scale data from complex systems. These methods often use network-based models and statistical techniques to study how components of a system, such as microbial communities, interact and change over time based on observed data. On the other end, "bottom-up" perspective studies focus on studying simpler systems or direct interactions between individual bacterial species in controlled experiments. This method builds understanding from basic, fundamental interactions to infer larger system behaviors, often using experimental data to observe how species interact and affect each other within a community.

Understanding biological systems from large data sets often relies on networks biology. Big Data projects like The Human Genome Project continue to follow such systems biology approaches [33]. Network-based approaches have been implemented to also study disease-related genes and predict drug targets using gene expression data, advancing the treatment of human diseases [34]. Analyzing large datasets from various organisms using these approaches has become increasingly popular, providing meaningful and valuable insights on ecological networks and patterns.

In recent years, these kinds of "top-down" approaches have been used extensively to study microbial ecology and interactions using analysis and modeling approaches. Co-occurrence analysis using sequencing-based metagenomics data has enabled the

identification of ecological patterns where co-existing microbes tend to be phylogenitically closely related to each other across several environments around the world [35]. Time series sequence-based data also has been used to infer dynamics within microbial communities, helping to infer ecological patterns through correlations [36].

Within the umbrella of modeling approaches, the Generalized Lotka-Volterra (GLV) model is the standard for studying population dynamics in microbial communities, accounting for external perturbations and predicting temporal dynamics. GLV model is foundational and versatile for understanding complex ecological systems and can be used to model various types of bacterial interactions as it used current state of the system and interactions strengths to predict dynamics. Minimal models like the Microbial Consumer-Resource Model (MiCRM) are known to recapitulate observed ecological patterns [37]. While these models enable us to do this qualitatively, they lack quantitative comparison to real world microbiomes with higher order interactions and constant environmental changes.

However, understanding ecological dynamics in a microbiome is directly related to both direct interactions between species and indirect interactions among species and cannot be fully comprehended from compositional data alone. Applying modeling approaches to experimental data cannot directly confirm whether collective outcome of microbial composition is due to direct or indirect interactions between bacterial species. Information about individual interactions that lead up to this composite data are often lost in the large data collection and analysis methods.

While these top-down approaches are essential for extracting patterns and predicting dynamics in microbiomes, they have limitations. The large amounts of data used in these models are often collected as snapshot data across individuals with different genetic, diet and environmental backgrounds (e.g., Human Microbiome Project [28]). These kinds of data are not easily reproducible, cannot be altered under different conditions and contain a lot of inter-individual variation that is lost in the data [38].

Particularly, correlation-based inferred network approach provides information on a larger scale yet remains insufficient to understand all the details about functional interactions driving microbiome community dynamics [39]. Similarly, modeling methods are most effective only when applied to species competition models, like gLV, involving a set of bacterial species that are experimentally convenient to handle [40].

On the contrary, "bottom-up" approaches are also used to address questions related to microbial interactions using simple models and experimental data. These approaches involve measuring ecological parameters, including those associated with growth and with interactions between species in a given environment, to understand the dynamics in a microbial community. Interactions between microbes can be of different types and strengths and can be simplified to sign (+/-) depending on its affect on the host and other species. These direct microbial interactions can be quantified using a variety of experiments which can be used as fundamental information for bottom up microbiome assembly.

Traditional attempts to understand species-species interactions started with observation of growth curves of species grown separately and in a mixed culture. The growth curves were fitted to logistic population growth equations [41]. This class of models has persisted and has been developed into the present day. For example, a recent study showed that relative fitness of bacterial species in co-culture can be inferred by fitting simple growth and competition models to optical density time series of mono-cultures and co-cultures [42]. Such data can be easily obtained from *in vitro* experiments, and the ecological parameter predictions effectively improve our understanding of species-species interactions. However, this is still limited to the number of species used in a laboratory setting and its utility is limited to pairwise interactions.

Using ecological network models, interactions that control the stability of microbiomes can be predicted. For example, competition between bacterial species is understood to be useful for the host and increases the stability of microbial commu-

nity [43]. Studies show that community structure can be predicted from competition outcomes in small sub-sets (pairs to trios) of bacterial species in controlled environments, supporting a bottom-up approach [44, 45]. However, this approach may not be applicable to natural microbial community data. As the complexity increases (more bacteria and higher order interactions), the accuracy of null model predictions of community function decreases [46, 47]. Further, while *in vitro* studies outside the host with a minimal microbial community can be done easily, the assembly of that community into a microbiome is very dependent on host environment [48]. Hence despite being the first step to understand community structure, the information from *in vitro* experiments is not enough for superimposition and prediction of dynamics in a host. Mapping of bacterial interactions to microbiome composition and to properties of the host is difficult, but this can be accomplished in experiments using a simple model host with small sets of bacterial species. Using a simple tractable host, like *Caenorhabditis elegans*, also makes it possible to address the inter-individual variation in bacterial composition inside the gut.

1.4 *C. elegans* as a model host

Host models are frequently used in experimental studies of microbial community ecology and dynamics [6]. Model host systems range from invertebrates, like nematodes and fruit flies, to simple vertebrates, such as zebrafish, *Danio rerio*, and to mammalian systems, like mice. Model hosts provide experimentally tractable systems in which to study microbiome ecology.

Small host models have provided insight into the ecology of host-microbiome systems. For example, experimental studies in zebrafish have shown that higher order microbial interactions inside the host can shape and alter their microbiome [9, 49].

For this dissertation work, I used *Caenorhabditis elegans* as an experimental model

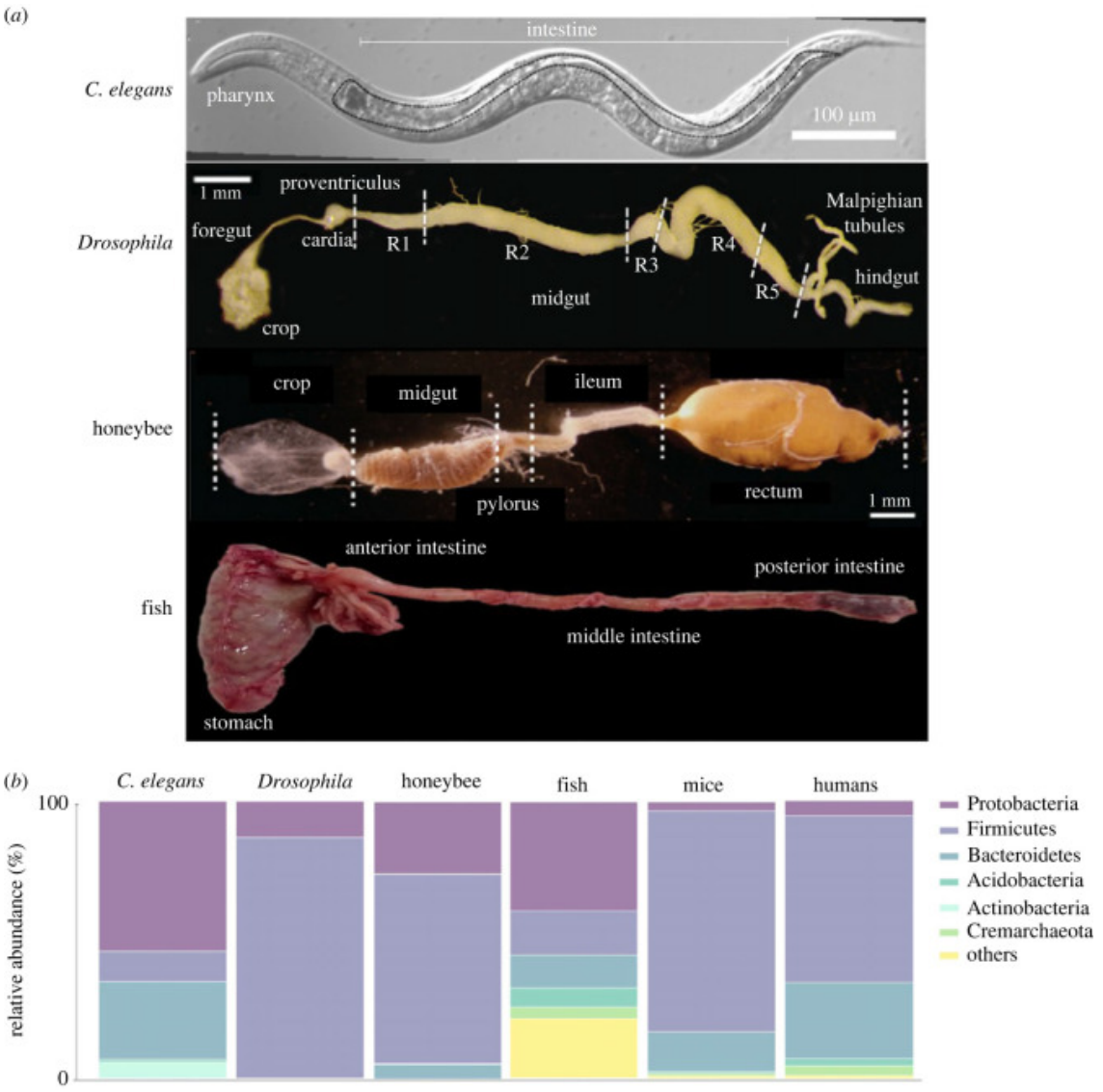

Figure 1.1: **Different model hosts and their intestinal bacterial composition** a) Microscopic images of model hosts (in order: *C. elegans* body, dissected guts of adult *Drosophila*, honeybee and *Seriola dumerilii*) with gut regions labelled b) Relative abundances of major bacterial phyla in different model host guts. Image reproduced with no changes from [6] under a Creative Commons Attribution 4.0 License (`https://creativecommons.org/licenses/by/4.0/`)

host (Figure 1.1a). *C. elegans* are bacterivorous soil-dwelling nematodes with androdioecious reproduction and a simple invertebrate body plan. These small worms ($\approx$ 1 mm length as adult hermaphrodites) can be easily maintained in the laboratory on agar plates with bacterial lawns as food. Worms mature rapidly ($\approx$ three days from

egg to adult), and a single adult hermaphrodite can produce 200-300 offspring over the first three days of adulthood, allowing large, highly homozygous populations with shared life history to be produced on convenient scales in time and space. These transparent worms are large enough to see by eye and manipulate by hand, and cellular and subcellular details can be visualized under microscopy [50]. The *C. elegans* intestinal epithelium is similar to that of higher animals making it convenient to study host-microbe association in a simple system. Accordingly, the worm has been used as a model system for understanding interactions with human pathogens [51, 52].

The nematode worm *C. elegans* is a convenient model for host-microbiome interactions. Several aspects in worms, ranging from immune response, to behavior, to utililty as a probiotic model, were studied by colonizing the "germ-free" gut with *E. coli*, *Bacillus subtilis* or pathogenic bacteria [53, 54]. However, until relatively recently, there was essentially no information available on interactions between *C. elegans* and microbes from its natural environment. Recent studies have shed light on the composition of the native *C. elegans* microbiome [55, 56]. Bacterial composition in both lab-enriched and natural worms is distinct from their substrates, and microbial community composition is conserved within a specific worm type across different geographical locations [55]. This suggests a characteristic native worm gut microbiome.

Bacterial species colonization in the nematode gut, however, is known to vary with the initial conditions, and the outcome of colonization is correlated and is dependent on species-species interactions. This highlights two things: stochasticity involved within this model host and the underlying conserved host-associated ecology despite the variability [10, 8]. Randomness in colonization also determines the community structure in an indirect way and needs to be considered. In *C. elegans*, the majority of bacterial cells get killed going through pharyngeal grinder, and that can result in randomness in this colonization process. But despite several environ-

mental perturbations and random events, microbiomes tend to be host-specific which indicates that there is host-associated filtering taking place. The composition of bacterial species in surroundings along with host genetics affects proliferation and functioning of worms living in that habitat while also contributing significantly to host-microbiomes [56, 57]. It is therefore essential to study the ecology and assembly rules of a host and its associated native microbiome.

Unlike that of other complex, vertebrate model organisms, the worm native microbiome is comparatively small (up to $\approx 10^5$ cells/worm), gathering data through experiments is convenient and reproducible. The data from experiments can be paired with mathematical approaches to understand host-microbe ecology. This tractable, low-maintenance model system has minimal limitations and a reasonable amount of data can be produced without losing control over the microbes involved and the host background. In other words, using *C. elegans* as a model host to understand the network structure of its native microbiome is both convenient and informative.

1.5 Dissertation Outline

In this dissertation, I present my work on quantifying variation in microbial association with the host *Caenorhabditis elegans* using experimental and mathematical approaches. Specifically, I focus on quantifying inter-individual variation in bacterial loads within a *C. elegans* population and on identifying drivers of this variation.

When data from individuals in a population are averaged, the biological variation of that population is lost resulting in an inaccurate representation of the data. In Chapter 2, the focus is on this hidden heterogeneity within isogenic populations of *C. elegans*. We present a detailed protocol for accurate and high-throughput single-worm disruption, facilitating bacterial load quantification. Significant heterogeneity in intestinal microbial populations is observed among worms colonized from the same

well-mixed solution with bacterial inoculum. This study mainly emphasizes the need for accurate individual-based measurements in studying host-microbe associations.

Measuring bacterial abundance in a culture or a host is usually done through serial dilution and recording colony-forming units (CFUs) in those dilutions, a part of the protocol described in Chapter 2. This widely used methodology is based on estimating density from suspensions of live bacterial cells, a problem complicated by sampling fluctuations, colony crowding, and technical errors. Chapter 3 addresses these challenges by examining existing point estimation methods and extending the applicability of the Most Probable Number (MPN) method to colony counts to get more accurate estimates. Additionally, a formula for combining counts from different dilutions (as opposed to counts from a single dilution) to obtain precise point estimates is given. This work provides practical recommendations for experimental design, contributing to reliable quantification of fluctuating microbial populations which is highly important in the study of microbiomes.

Chapter 4 presents work on the drivers of variation in microbiome composition within and between hosts. In *C. elegans*, isogenic, synchronized populations colonized with a homogeneous inoculum exhibit significant inter-individual variation in microbiome composition. This work combines experimental data with mathematical modeling to identify potential sources of this variation. By mono-colonizing worms with individual bacterial species from a minimal native microbiome, I show that microbe-microbe interactions are not essential to create this variation. Even with only one bacterial species colonizing the worm, gut we see significant inter-individual variation in host-associated bacterial load. This study also suggested the presence of alternative steady states in bacterial load, indicating that traditional Lotka-Volterra type models may not fully capture the dynamics of host-microbe systems.

Overall, my dissertation builds on the detailed examination of host-microbe interactions in *C. elegans*, presenting innovative experimental and quantifying methods

that advance the field of microbiome research. The protocols and models presented herein not only facilitate accurate microbial quantification but also reveal some underlying drivers of microbial community variation, paving the way for future studies focused on host-associated microbiomes.

Chapter 2

Using Single-Worm Data to Quantify Heterogeneity in *Caenorhabditis elegans* -Bacterial Interactions

This chapter is adapted from a previously published paper [58].

2.1 Summary

The nematode *Caenorhabditis elegans* is a model system for host-microbe and host-microbiome interactions. Many studies to date use batch digests rather than individual worm samples to quantify bacterial load in this organism. In this chapter, it is argued that the large inter-individual variability seen in bacterial colonization of the *C. elegans* intestine is informative, and that batch digest methods discard information that is important for accurate comparison across conditions. As describing the variation inherent to these samples requires large numbers of individuals, a con-

venient multi-well protocol for disruption and colony plating of individual worms is established. This chapter describes the above-mentioned 96-well disruption of individual bacterially-colonized *C. elegans* following cold paralysis and surface bleaching to remove external bacteria. The resulting suspension is plated on agar plates to allow accurate, medium-throughput quantification of bacterial load in large numbers of individual worms.

2.2 Introduction

Heterogeneity in host-microbe associations is observed ubiquitously, and variation between individuals is increasingly recognized as a contributing factor in population-level processes from competition and coexistence [59] to disease transmission [60, 61, 62]. In *C. elegans*, "hidden heterogeneity" within isogenic populations has been observed repeatedly, with sub-populations of individuals showing distinct phenotypes in heat shock response [63, 64] ageing and lifespan [65, 66, 67, 68, 69], and many other aspects of physiology and development [70]. Most analyses that attempt to identify sub-population structure provide evidence for two sub-populations in experimental populations of isogenic, synchronized worms [63, 65, 66] though other data suggest the possibility of within-population distributions of traits rather than distinct groups [65, 70, 71]. Of relevance here, substantial heterogeneity in intestinal populations is observed even within isogenic populations of worms colonized from a shared source of microbes [71, 48, 72, 73], and this heterogeneity can be concealed by the batch digest measurements that are widely used [8, 74, 75, 76] for bacterial quantification in the worm.

This work presents data suggesting a need for greater reliance on single-worm measurements in host-microbe association, as well as protocols for increasing accuracy and throughput in single-worm disruption. These protocols are designed to facilitate

mechanical disruption of large numbers of individual *C. elegans* for quantification of viable bacterial load, while providing better repeatability and lower effort per sample than pestle-based disruption of individual worms. A recommended gut-purging step, where worms are permitted to feed on heat-killed *E. coli* prior to preparation for disruption, is included to minimize contributions from recently ingested and other transient (non-adhered) bacteria. These protocols include a cold-paralysis method for cleaning the cuticle with a low-concentration surface bleach treatment; surface bleaching can be used as a preparatory step in single-worm disruption or as a method for preparing live, externally germ-free worms. This surface-bleaching method is sufficient to remove a wide range of external microbes, and cold treatment provides an alternative to conventional levamisole-based paralysis; while levamisole will be preferred for cold-sensitive experiments, cold paralysis minimizes contributions to hazardous waste streams and allows rapid resumption of normal activity. While the full protocol describes a laboratory experiment where worms are colonized with known bacteria, the procedures for cleaning worms and single-worm disruption can readily be applied to worms isolated from wild samples or colonized in microcosm experiments. The protocols described here will produce live bacteria extracted from the worm intestine, suitable for plating and quantification of colony forming units (CFUs) in individual worms; for sequencing-based intestinal community analysis, subsequent cell lysis and nucleic acid extraction steps should be added to these protocols.

2.3 Protocol

Worms used in these experiments were obtained from the *Caenorhabditis* Genetic Center, which is funded by NIH Office of Research Infrastructure Programs (P40 OD010440). Bristol N2 is the wild-type. DAF-2/IGF mutants *daf-16(mu86)* I (CGC CF1038) and *daf-2(e1370)* III (CGC CB1370) are used to illustrate differences in

intestinal bacterial load.

HT115(DE3) *E. coli* carrying the *pos-1* RNAi vector is from the Ahringer library [77]. The MYb collection of *C. elegans* native gut bacteria [55] was obtained from the Schulenburg lab. *Salmonella enterica* LT2 (ATCC 700720) *attB:GFP-KmR* is from this lab [78]. *Pseudomonas mosselii* was isolated in this lab. *Staphylococcus aureus* MSSA Newman pTRKH3-mGFP was obtained from the LaRock lab at Emory University.

All worm buffers and media are prepared according to formulations and protocols in Wormbook chapter "Maintenance of *C. elegans*" [79].

2.3.1 Preparation of synchronized sterile *C. elegans*

In this section, step-by-step procedures are described for generating a synchronized population of reproductively sterile adult worms. Feeding on *pos-1* RNAi plates is used here to prevent production of progeny because this interference is embryonic lethal; L1 larvae raised to adulthood on *pos-1* RNAi develop into egg-laying hermaphrodites, but these eggs are inviable [80]. The RNAi feeding protocol is as in the "Reverse genetics" chapter of Wormbook [81].

- Before synchronizing worms, ensure that fresh 10 cm NGM + *pos-1* RNAi plates will be available. Plates can be prepared fresh from concentrated induced liquid culture (+Amp + IPTG) or inoculated as lawns on NGM +100μg/mL ampicillin +1mM IPTG and allowed to grow at 25°C in the dark for one day [82].

  NOTE: Carbenicillin (25 μg/mL) is often used instead of ampicillin on RNAi plates. Ampicillin is less expensive but less stable; if using ampicillin, plates should be seeded immediately once dry and used as soon as possible (can be stored for $<$ 1 week at 4°C) [82]. The high antibiotic concentration recommended here will help to ensure adequate selection.

- Start with several (typically 2-4) NGM plates with large populations of gravid hermaphrodites. Isolate eggs using bleach- NaOH synchronization [79].

  - Wash worms off agar plates using 2 mL sterile ddH_2O per plate. Distribute the liquid evenly into 1.5 mL microcentrifuge tubes (one tube per plate or hermaphrodites).
  - Spin down for ~ 5 seconds in a benchtop minicentrifuge (2000xg) to pull adults to the bottom of the tubes. Pipet off supernatant and discard.
  - Wash with 1 mL sterile ddH2O; spin down as before and discard supernatant.
  - Repeat previous step to reduce remaining bacterial debris.
  - Resuspend the contents of each tube in 1 mL sterile ddH2O. Add to each tube 130μL commercial bleach (8.25% sodium hypochlorite) and 130μL5 N sodium hydroxide (NaOH, final concentration 0.5 N).
  - Vortex tubes vigorously for at least $10 - 15$ seconds every two minutes until adult bodies have broken up. Do not allow bleach- NaOH treatment to go longer than 5 minutes to avoid killing eggs.
  - Spin in a minicentrifuge for $30 - 60$ seconds at $2000 \times g$ to pellet the eggs; pipet off the supernatant and discard. There may or may not be a visible pellet, this is normal.
  - Add 1ml of M9 worm buffer; spin $30 - 60$ seconds at $2000\times$ g. Discard supernatant.
  - Repeat the previous rinse step 5X to thoroughly remove bleach- NaOH mixture, removing as much of the supernatant as possible without disturbing the egg pellet.
  - Transfer eggs to 10 mL of M9 worm buffer in a 50 mL conical tube or

30 mL culture tube with cap. If using conical tubes, leave the lid unscrewed slightly and use a bit of tape to keep it secure. Incubate with shaking overnight (16 hours) at 25°C and 200 RPM to allow larvae to hatch.

- Transfer synchronized L1 larvae to RNAi plates to grow to adulthood.
  - Add 2 mL sterile M9 buffer +0.01% Triton X-100 (henceforth M9TX-01) to each L1 tube and transfer the entire volume (12 mL) to a 15 mL screw-top conical tube.
  - Place 15 mL tubes with L1 worms at 4°C for 10 minutes to slow larval movement.
  - Spin down 15 mL conical tubes in a large tabletop centrifuge (1500xg at 4°C for 3 minutes; acceleration and deceleration should be no higher than 80% of maximum).
  - Carefully pipet off supernatant without disturbing the $L1$ pellet. Discard supernatant.
  - Add 12 mL cold M9TX-01 to each tube. Repeat the centrifugation; carefully pipet off and discard supernatant. Each tube should have $\sim 200\mu$L remaining.
  - . Rinse a 200μL pipet tip in M9TX-01 to keep worms from sticking to the plastic, then use this tip to resuspend the worm pellet. Transfer resuspended worms to prepared *pos-1* plates by pipetting drops of liquid onto the bacterial lawn.
  - Incubate the plates at 25°C until the first day of adulthood.

NOTE: If growing worms on *pos-1* RNAi plates, worms MUST feed *ad libitum* on the RNAi bacteria until they have fully transitioned to adulthood to ensure

high penetrance of the embryonic-lethal phenotype. Check the plates at 24 and 48 hours. If the plates appear starved or nearly starved, the worms will need to be moved to fresh plates to finish growing into full-sized adults. To avoid depleting plates before worms are grown, aim to add 250-500 L1 larvae to each 10 cm RNAi plate.

- Harvest adults and clear intestinal *E. coli* to create germ-free worms.
  - Rinse adult worms from plates using 5 mL M9TX-01 per plate. Transfer buffer + worms to a 15 mL conical tube and allow adults to settle to the bottom of the tube.
  - Rinse adults in changes of 10 mL fresh M9TX-01 buffer until no visible bacterial turbidity remains (typically 1-2X). Tubes can be centrifuged at 700xg for 30 seconds to pellet worms, or adults can be allowed to settle by gravity.
  - Perform one additional wash with 10 mL M9TX-01 to reduce external bacteria.
  - Transfer worms to 50 mL conical tubes or 30 mL culture tubes containing 5 mL S Medium $+2X$ heat-killed *E. coli* OP50 ($\sim 5 * 10^9$ killed cells /mL) + 200 μg/mL gentamycin +50 μg/mL chloramphenicol. If using conical tubes, leave the lid unscrewed slightly and use a bit of tape to keep it secure. Use glass pipets or rinse plastic pipets in M9TX-01 to keep the worms from sticking.
  - Incubate adults at 25°C with shaking at 200 RPM for $24 - 48$ hours to produce germfree adults.

NOTE: If the worms are to remain in antibiotics for $>$ 24 hours, more heat-killed OP50 may have to be added to ensure that the worms have an adequate

food source. Check tubes at 24 hours and supplement with heat-killed OP50 if turbidity is visibly reduced.

- Sucrose wash adults according to standard protocols [79] to obtain clean, reproductively sterile, synchronized adult-only stocks for bacterial colonization.
  - Ensure that cold volumes of 60% sucrose, M9 worm buffer, and M9TX-01 are ready for use. For simplicity, these can be left at 4°C the night before.
  - For each sample to be washed, create a labeled 15 mL conical tube containing 8 mL of M9TX-01 and set aside on ice. These will be needed later.
  - Add 5 mL M9TX-01 to each 50 mL tube containing L1 larvae. Transfer the entire volume (now 10 mL) to an empty 15 mL screw-top conical tube and allow adults to settle to the bottom of the tube.
  - Carefully pipet off the supernatant and discard.
  - Add 10 mL M9TX-01 to each tube and move tubes to an ice bucket for $5 - 10$ minutes. Starting at this point, worms and all buffers should be kept on ice.
  - Use the "fast temp" setting to cool a large tabletop centrifuge to 4°C.
  - Add 10 mL cold M9TX-01 to each tube to rinse off any remaining debris. Let worms settle on ice; remove supernatant and discard.
  - Sucrose float: Add 5 mL of cold M9 buffer and 5 mL of cold 60% sucrose solution to each tube, mixing thoroughly. Then - carefully! - float 1 mL of cold M9 buffer on top of the sucrose-buffer mixture in each tube. Do not mix after the float has been added.

    Move quickly for the next few steps - worms can desiccate if exposed to high concentrations of sucrose for too long!

- Centrifuge at 1500 × g for 3 minutes at 4°C. Live adult worms will be at the interface of the M9 and the sucrose, approximately 1 mL from the top of the tube.
- Use a glass 5 mL serological pipet to transfer the worm layer to prepared 15 mL conical tubes with cold M9TX-01 . Be very careful to get the layer of live worms without pipetting up too much of the sucrose.
- If necessary, add M9TX-01 to get equal volumes of $10 - 12$ mL/tube. Centrifuge at 1500xg at 4°C for 1 minute, then pipet off the supernatant.
- Worms can be returned to room temperature at this point. Repeat the previous wash step twice, reducing the speed to $700 \times g$ at 4°C and time to 30 seconds.

2.3.2 Feeding worms on live bacteria in liquid culture

This protocol is used to colonize worms with laboratory-grown bacteria in well-mixed conditions in liquid culture (2.1). Worms can be colonized with individual isolates from pure culture (e.g. pathogens such as *Enterococcus faecium* [83, 84]) or mixtures of isolates (e.g. minimal microbiome communities [48]).

- Start with sucrose washed synchronized adult worms in a 15 mL conical tube. Wash the worms once in 12 mL S buffer and discard supernatant.
- Resuspend the washed worms in the volume of S medium needed for the experiment. Consider the volume of experimental conditions, the number of conditions over which worms will be split, and the final concentrations of worms and bacteria.

  NOTE: Feeding in worms varies with bacterial availability [85] and worms can be stressed by crowding [86]. For colonization in liquid culture, < 1000 worms

/mL and $> 10^7$CFU/mL are recommended; 10^{11}CFU/mL is considered "*ad libitum*" feeding density on *E. coli* [87].

- Spin down bacterial cultures. Pour off supernatant; aspiration or pipetting can be used to remove supernatant for bacteria that form loose pellets.

  NOTE: For cultures > 5 mL, transfer to 15 mL tubes and spin at $\sim$ 2800xg in a large tabletop centrifuge for 8-10 minutes. Cultures < 5 mL can be transferred to 1.5 mL tubes and centrifuged at $9000 \times$ g for 1-2 minutes in a small tabletop centrifuge. Highly motile bacteria (e.g. many species of *Pseudomonas*) may need to be chilled at 4°C for $10 - 15$ minutes to facilitate formation of a stable pellet, and it may be better to centrifuge at 4°C.

- Resuspend bacterial cultures in 1 volume *S* buffer and centrifuge again to pellet. Remove and discard supernatant as before.

- Resuspend bacterial cultures in S medium at the desired density for the experiment, plus any antibiotics for selection. The antibiotics to be used, if any, will depend on the resistance profile of the bacteria used for colonization.

- Using a pipet tip coated in M9TX-01, pipet worms gently up and down until worms are thoroughly resuspended in S medium, then transfer to tubes or plate wells for bacterial colonization.

- Add bacterial suspension to each worm culture to reach the desired bacterial concentration and final volume.

- If using a multi-well plate for colonization, cover plate with a sterile 96 -well gas-permeable sealing membrane.

- Incubate with shaking at 200 RPM to prevent bacteria from settling during incubation.

2.3.3 Mechanical disruption of individual worms in a 96 -well format

This section describes a 96 -well plate format protocol for mechanical disruption of individual bacterially-colonized C. elegans. The first steps in the protocol describe a method for purging non-adhered bacteria from the worm intestine and cleaning the exterior of the worms using cold paralysis and surface-bleaching; these steps will produce clean, live adult worms that can be mechanically disrupted for quantification of bacterial contents or used for further experiments (2.1). This protocol can be adapted to quantify bacteria in worms colonized in liquid culture (Protocol 2.3.2), on agar plates, or from natural or microcosm soil.

- Place an aliquot of M9TX-01 on ice to chill (4-5X the number of samples in mL).
- Prepare an aliquot of M9TX-01 + bleach (6% sodium hypochlorite, 1:1000 or 1:2000 v/v, 1 mL per sample +1 mL extra) and place on ice to chill. This aliquot will be used later.
- Prepare 96 -well plates for serial dilution of disrupted worm samples.
  - Obtain sterile 300μL-capacity 96 well plates with lids; this protocol uses one dilution plate per 12 worms digested.
  - Use a 96 -well multichannel pipettor to fill rows B-D of each plate with 180μL of 1X PBS buffer. Leave the top row empty. Rows B-D will become 10X serial dilutions of the worm digests [0.1X, 0.01X, 0.001X].
  - Set plates aside. Dilution plates will be used in later steps.
- Resuspend each worm sample in 1 mL M9TX-01 in a 1.5 mL microcentrifuge tube.

- Spin tubes briefly ($2-3$ seconds) in a low-speed minicentrifuge ($2,000$xg) at 25°C to pellet adults. Pipet off supernatant and discard, being sure not to disturb the worm pellet.
- Using the centrifugation settings from previous step, rinse worms twice with 1 mL M9TX-01, then once with 1 mL M9 worm buffer, to reduce external bacteria.
- Purge non-adhered bacteria from the worm intestine.
  - Resuspend each sample of worms in 1 mL S- medium +2X heat-killed OP50 in a culture tube.
  - Incubate at 25°C for $20-30$ minutes to allow passage of any non-adhered bacteria from the gut. This will also purge any extracellular fluorescent protein from the lumen and allow clearer visualization of labeled bacteria adhered to the intestinal epithelium, particularly when acid-fast fluorophores (e.g. mCherry, dsRed) are used.
- Surface bleach worms to clear external bacteria.
  - Rinse purged worms twice with 1 mL cold M9TX-01 and discard the supernatant.
  - Allow tubes to chill for 10 minutes on ice (preferred) or at 4°C. This will paralyze worms and prevent ingestion of bleach.

    NOTE: Other protocols use a chemical paralysis agent such as levamisole; this is an established approach [88] which requires addition of a hazardous waste stream.
  - Add 1 mL ice-cold M9 worm buffer + unscented bleach (8.25% sodium hydroxide, 1 : 1000 or 1 : 2000v/v) to each tube. Allow tubes to sit on ice (preferred) or at 4°C for at least 10 minutes to kill external bacteria.

NOTE: DO NOT EXCEED 1:1000 CONCENTRATION OF BLEACH. Even in paralyzed worms, mortality can result.

- Pipet off bleach buffer and discard; return tubes to ice to ensure worms do not resume pumping until bleach is cleared.
- Add 1 mL cold M9TX-01 to each tube. Spin $\sim$ 5 seconds in a minicentrifuge ($2000 \times$ g at 25°C); return tubes to ice. Remove supernatant and discard.
- Repeat this rinse step with another 1 mL cold M9TX-01, discarding as much of the supernatant as possible.

NOTE: If using worms for further experiments, skip the permeabilization step and instead transfer freshly surface-bleached adults to ice-cold buffer in a 6 cm Petri dish and separate worms into experimental conditions as in Protocol 3.10. Keep worms cold to prevent motility from resuming, but work quickly - keeping worms for $>$ 30 minutes on ice can potentially result in $<$ 100% resumption of normal activity [89].

- Chemical permeabilization of worm cuticle with sodium dodecyl sulfate and dithiothrietol (0.25% SDS +300mM DTT) (based on [90]).

  CAUTION: DTT is a reducing agent and irritant. Wear PPE and work in a fume hood when handling dry stocks or solutions. A hazardous waste stream is required.

  - In the fume hood, prepare enough SDS/DTT solution to allow 100μL for each sample. For 1 mL, to 965μL M9 worm buffer or M9TX-01 in a 1.5 mL microcentrifuge tube, add 5μL of 5%(w/v) SDS and 30μL of 1M DTT.

    NOTE: 1M DTT solution (aqueous) should be prepared fresh or stored in aliquots at -20°C to ensure potency. Aliquots should be sized to be used

up in two to three experiments to avoid excessive freeze-thaw cycling.

- Move microcentrifuge tubes containing surface-bleached worms to a roomtemperature tube rack. Each tube should contain worms in $\sim 20\mu$L of buffer.
- Add 100μL SDS/DTT solution to each worm sample; dispose of any remaining SDS/DTT solution in the appropriate hazardous waste stream.
- Allow the treatment to proceed for up to 8 minutes on the bench to partially break down the resistant cuticle of the adult worms. Worms will die and settle to the bottom of the tube during this time.
- After permeabilization time is up, carefully pipet off the SDS/DTT supernatant and dispose of it in an appropriate SDS/DTT hazardous waste stream.
- Add 1 mL M9TX-01 to each tube. Spin briefly in a table-top centrifuge to pellet the worms, or allow worms to settle by gravity to the bottom of the tubes, then draw off the supernatant and dispose of it in a SDS/DTT hazardous waste stream.
- Resuspend worms in 1 mL M9 worm buffer +01% Triton X − 100 until ready to use.

- Separate worms into a deep 96 -well plate with silicon carbide grit for mechanical disruption.
  - Prepare the 96 -well disruption plate.
    * Obtain a sterile 2 mL deep-well 96 -well plate and a matching silicon 96 -well plate cover.

      NOTE: It is important to use plates that are compatible with the 96-well adaptors for the tissue disruptor. Tiny differences in external

dimensions make the difference between a plate that can be removed from the adaptors and one that cannot.

  * Using a sterile scoop spatula, add a small amount of sterile 36 -grit silicon carbide to each well of the plate that will receive a worm. Use enough grit to barely cover the bottom of the well - about 0.2 g per well. Excessive material will make it difficult to get a pipette tip to the bottom of the well when retrieving the contents.
  * Add 180μL M9 worm buffer to each well.
  * Label the columns or rows to indicate where each sample will go, then cover the plate loosely with the silicon 96 -well plate cover.

- Transfer individual worms to the 96 -well plate for disruption.
  - Move permeabilized worms carefully to a small (35 or 60 mm) petri dish containing sufficient M9TX-01 to fill the dish to a depth of $\sim$ 1 cm.

    NOTE: If a large number of worms are present, it may not be feasible to transfer the entire sample as the liquid will become crowded and it will be difficult to pipet individual worms.
  - Using a dissecting microscope or other low-magnification device, pipet off individual worms in 20μL volumes, and transfer these worms to individual wells of the 96 -well plate.

    NOTE: It is best to harvest only freshly killed worms. Avoid worms with a rigid linear shape, as these worms may have been dead for some time. Try to take worms that are curved or S-shaped, with normal gross physiology and an intact gut.
  - After transferring each volume, make sure that the selected worm was actually ejected into the well. To do this, pipet up 20μL of M9TX-01 from a clear area of the petri dish and release the full volume back into the dish;

this will normally eject the worm if it is stuck to the pipet. If the worm was stuck, remove 20μL from the well and try the transfer again.

- Once all worms have been transferred, cover the 96 -well plate with a sheet of commercially-available flexible paper-backed sealing film (2×2 squares), making sure that the paper-backed side of the sealing film is facing down onto the sample wells. Be careful not to stretch the sealing film too thin, or it will be very difficult to remove later.
- Place the silicon sealing mat lightly on top of the flexible sealing film; do not press the cover down into the wells at this time.
- Move the plate to 4°C to chill for $30 - 60$ minutes. This will prevent over-heating during disruption, which can damage the samples.

NOTE: This is a break point in the protocol. In most cases, the plate can be left at 4°C for up to four hours before grinding. Do not leave the worms overnight, as this will change the bacterial counts.

- Load 96-well plates onto a tissue disruptor to break up worm tissues and release intestinal bacteria.

  OPTIONAL: If using an odd number of 96 -well plates for digests, it is necessary to prepare a counterweight before proceeding. Use an empty deep 96 -well plate and fill wells with water until it weighs the same as the first plate.

  - Press the silicon sealing mat down firmly into the wells to create a seal, making sure the lid lies flat across the entire surface of the plate.

    NOTE: If the flexible sealing film is too thick after stretching, it will be difficult to secure the silicon lid such that it is lying flat in all wells. This will result in an insufficient seal and wellto-well contamination during shaking.

  - Secure plates in the tissue disruptor using the 96 -well plate adaptors. Shake plates for 1 minute at 30hz, then rotate plates 180° and shake again for 1 minute. This will help ensure even disruption in all wells of the plate.
  - Tap plates firmly on the bench 2-3 times to dislodge any grit from the flexible sealing film.
  - Using a large centrifuge with 2 × 96-well plate adaptors, spin the plates down at 2400 xg for 2 minutes to gather all material to the bottom of the wells.
  - Remove the silicon lid and carefully pull off the flexible sealing film.

  NOTE: If the flexible sealing film sticks in any of the wells, use a 200μL pipet tip to remove it. This is common when the flexible sealing film was stretched too thin.

- Serially dilute worm digest samples in 300μL96-well plates.
  - Using a multi-well pipettor set to 200μL, pipet up and down several times slowly and carefully to re-mix the contents of the wells, then draw off as much of the liquid as possible. Transfer this liquid to the top rows of the 96 -well plates prepared previously.
  - Using a 96 -well pipettor set to 20μL, remove this volume of liquid from the top row and dispense into row B. Pipet up and down 8-10X to mix. Discard tips.
  - Repeat this step, starting from the 0.1X samples in row B to create 0.01X dilution samples in row C.
  - Repeat the same step again, going from row C to row D.
  - Plate onto solid agar for bacterial quantification. For mono-colonized worms, it is generally sufficient to plate $10 - 20\mu$L drops of each dilu-

tion [1X-0.001X] on agar plates. For multi-species colonization, plate each dilution separately by pipetting 100μL onto a 10 cm agar plate; spread immediately using glass plating beads.

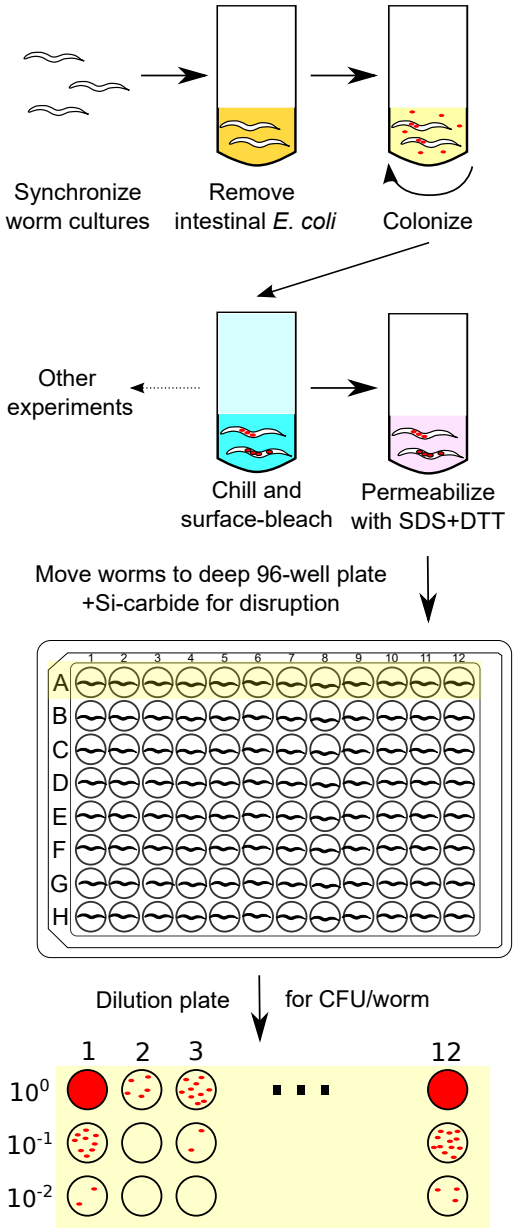

Figure 2.1: Overview of the Protocol. Here, synchronized adult worms are mono-colonized with red bacteria, surface-bleached, and permeabilized before mechanical disruption of individual worms in a 96-well format. Bacteria released from the intestine are dilution plated in 10X series for CFU/worm quantification; plates shown are typical for observed heterogeneity.

2.3.4 Cleaning silicon carbide grit for re-use

This procedure is used to clean and sterilize the grinding material, silicon carbide grit, for re-use after experiments. This protocol should be followed in its entirety before first use, as silicon carbide grit is an industrial product and does not come pre-sterilized. Si-carbide grit (3.2 g/cc) is a dense, rough-edged material that works efficiently to disrupt tough samples. However, the particles can wear down over repeated use and should be replaced when wear becomes apparent. Fortunately, the material is inexpensive, and the sizes typically sold ($\sim$ 1lb) are sufficient for many experiments.

- After removing samples for plating, add 10% bleach solution to all wells of the 96 -well plate and let sit for at least 10 minutes.
- Remove the bulk of the grit by rapidly inverting the 96 -well plate over a small high-sided tray or empty P1000 pipet tip container large enough to catch all the contents. The grit will sink immediately to the bottom of the tray. Pour off the bleach solution into a sink.
- Re-fill the 96-well plate with tap water and invert into the same tray to rinse out remaining grit. Pour the water off into the sink.
- Repeat one to three more times with tap water until plate is completely clear of grit.
- Rinse grit 2X in tap water, filling the tray each time.

  NOTE: The 96 -well deep well plate can be washed in a laboratory dishwasher, covered securely with foil, and autoclaved with other reusable plastics.

  NOTE: Grit does not need to be washed immediately and can be set aside at this point. Used grit is usually accumulated from multiple experiments before washing and autoclaving.

- Wash grit in a solution of laboratory detergent for 30 minutes, agitating occasionally by swirling or mixing with a metal spatula.
- Rinse away all traces of detergent in several (8-10) changes of tap water, then rinse 2X with distilled water.
- Spread grit in an open tray, such as a shallow polypropylene autoclave tray, and dry at 40-70°C for several hours.

  NOTE: If the grit is clumpy when dry, it was not cleaned or rinsed sufficiently. Repeat the cleaning protocol with additional rinses in previous step .
- Distribute clean, dry grit into screw-top autoclavable glass bottles to a maximum depth of 5-6 cm. Autoclave on prevac cycle for 30 minutes to sterilize.

2.4 Results

2.4.1 Bleach sterilization of live worms

Surface-bleached worms are effectively free of external bacteria until motility returns and excretion resumes. Under the conditions used here, rapid extinction of bacteria in buffer is observed (Figure 2.2A-C) without disturbing the gut-associated bacteria in cold-paralyzed worms (Figure 2.2D-F). These data indicate that surface bleaching can be used effectively to sanitize worms externally without compromising the intestinal contents (comparisons of surface-bleached vs no-bleach worm-associated CFU counts are non-significant, Wilcoxon rank-sum test $p>0.05$).

2.4.2 Variations on multi-sample mechanical disruption

The 96-well technique for mechanical disruption of worms is robust to the specific materials used, and practical considerations dictate the choice of grinding material.

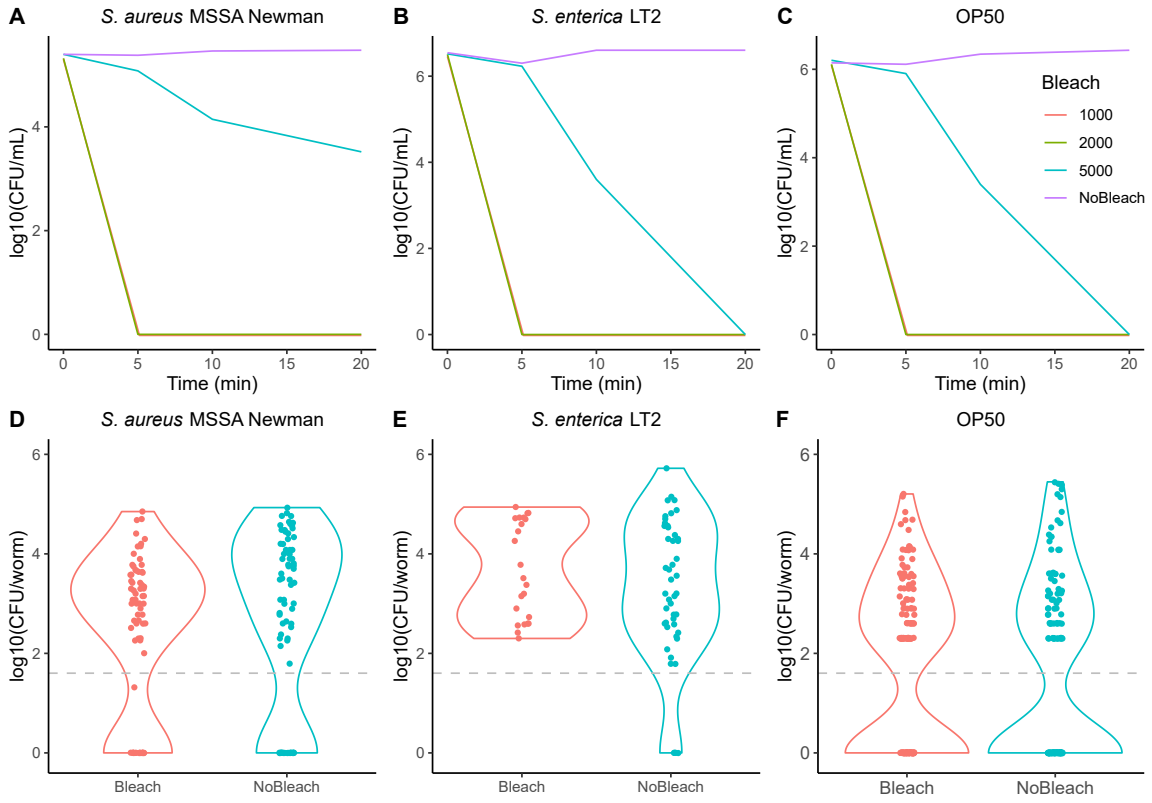

Figure 2.2: Low-concentration surface-bleaching treatment rapidly kills bacteria in buffer but does not disturb intestinal communities in cold-paralyzed worms. (A-C) Bacterial CFU/mL in M9 worm buffer during surface bleaching at three different concentrations (1:1000, 1:2000, 1:5000 v/v; unbleached control for comparison), targeting (A) S. aureus Newman, (B) S. enterica LT2, or (C) E. coli OP50. Samples were taken at indicated time points up to 20 minutes post-exposure and washed twice with sterile buffer to prevent bleach from killing colonies on plates. Data for the 1:1000 condition are offset slightly so that these data are visible on the plot. (D-F) Intestinal bacteria in individual N2 worms (n=24 worms per experiment, 2-3 independent runs on separate days). All comparisons of surface-bleached and no-bleach worm-associated CFU counts are non-significant (Wilcoxon rank-sum test $p>0.05$). Grey horizontal lines represent threshold of detection, defined as the density (40 CFU/worm) at which probability of observing at least one colony is 60%.

Similar to a previous report [88], manual disruption (Figure 2.3A) resulted in more heterogeneity than the standard 96-well protocol (silicon carbide grit, Figure 2.3B) (var(log_{10}CFU)=0.499 across all buffer conditions, as compared with 0.229 for Si-carbide, 0.243 for large glass beads (Figure 2.3C), and 0.227 for small glass beads (Figure 2.3D)). Nonetheless, most differences in CFU/worm distributions were not

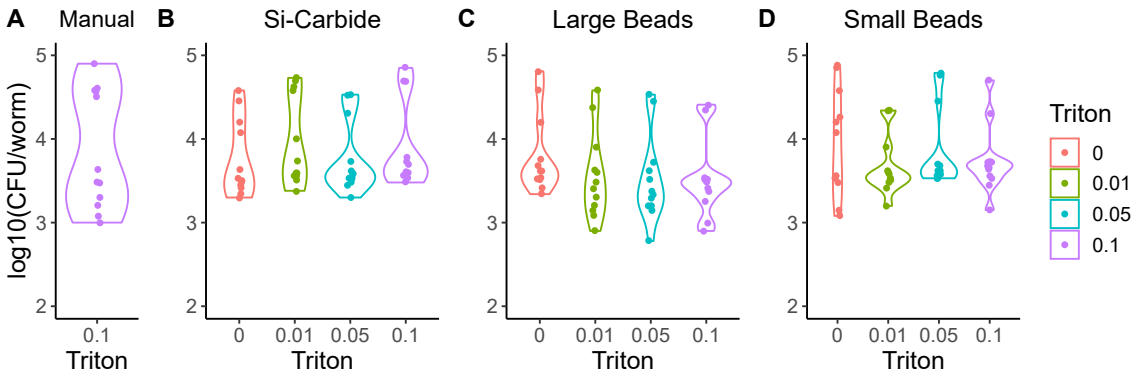

Figure 2.3: The 96-well disruption protocol produces consistent results and is robust to choice of materials. N2 adult worms colonized with a single bacterial species for 48 hours (P. mosselii) were surface bleached and permeabilized according to standard protocols, then individual worms (n=24 per condition) were mechanically disrupted for CFU plating using (A) manual disruption in individual 0.5 mL tubes, using a motorized pestle or (B-D) variations on the 96-well disruption protocol described in detail in the Protocol. Disruption was carried out in M9 worm buffer containing varying concentrations of Triton X-100 (x-axis, 0-0.1%,v/v) and one of (B) 36-grit silicon carbide, (C) small (425-600 µm) glass beads, (D) large (2.7 mm) glass beads. For all plots, data shown are log_{10}(CFU/worm), and each point is one individual worm.

significant (Kruskal-Wallace p=0.017 with df=3; significant post-hoc Wilcoxon tests for large beads vs. small beads p=0.021 and large beads vs. silicon carbide grit p=0.02). The use of Triton X-100 as a surfactant was not associated with any significant difference in yield when considered as an individual factor (Kruskal-Wallace p=0.94, df=3), although there is an apparent increase in yield in no-Triton vs. Triton-containing samples when large beads (2.7 mm) were used (Figure 2.3C), possibly attributable to the excessive "foaming" observed in these wells when Triton was present. These results indicate that large glass beads, while ideal for use in homogenization tubes [88], are not suitable for the 96-well technique. While small glass beads produced reasonable results (Figure 2.3D), they consistently clogged 200 µL pipet tips during mixing and plating. The standard material in this assay, silicon carbide grit, is inexpensive, too large to clog standard tips, and like glass beads can be washed and reused after autoclaving. The grit does release a small amount of "dust" into

the buffer, which does not interfere with plating but needs to be filtered off if the products of disruption are to be used for flow cytometry.

2.4.3 Heterogeneity in bacterial colonization in adult worms

Successful disruption of individual worms reveals heterogeneity in bacterial colonization. Individuals from isogenic synchronized populations of worms, colonized at the same time on the same pool of bacteria, consistently show 100-fold or greater range in intestinal bacterial load. This is observed for different bacterial colonists (Figure 2.4A) and during colonization on multi-species bacterial communities (Figure 2.4B). This heterogeneity is also evident in individual-worm measurements of fluorescence when worms are colonized with bacteria expressing a fluorescent protein (GFP) (Figure 2.4C-D). The properties of the host play a role in shaping this heterogeneity, as can be seen by comparing colonization of wild-type Bristol N2 worms to colonization by the same bacteria in DAF-2/IGF mutants; this daf-16 mutant supports larger populations of many bacteria as compared with N2, while daf-2 is resistant to colonization by a range of bacteria [91] (Figure 2.4B, D). This heterogeneity is characteristic, showing variation across different combinations of host and colonist(s), while retaining a consistent structure over different runs of the same experiment (Figure 2.4E-F).

2.4.4 Importance of individual heterogeneity for accurate comparison of groups

The importance of individual heterogeneity can be easily seen by considering how batch digests could alter the distributions of data. Colonization by native microbiome bacteria MYb53 (*Rhodococcus erythropolis*) and MYb120 (*Chryseobacteria spp.*) (Figure 2.4A, 2.5A) in N2 adults are used as examples. The individual worm data are

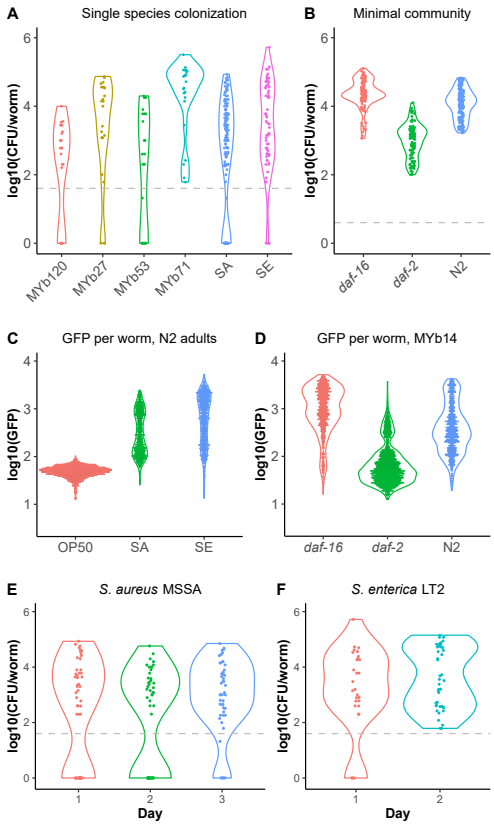

Figure 2.4: Heterogeneous bacterial colonization of the C. elegans intestine. (A) Single-species colonization of N2 adult hermaphrodites prepared as in Methods. Bacteria are four species from the MYb native worm microbiome collection ([55]) (n=24 worms, one experiment each) and two pathogens, *Staphylococcus aureus* MSSA Newman (SA) and *Salmonella enterica* LT2 (SE) (n=96-144 worms over 2-3 independent experiments). Colonization by native microbiome species was assessed after 48 hours' incubation at 25°C in liquid S medium + 10^8 CFU/mL bacteria; colonization by pathogens was assessed after incubation on lawns on NGM worm agar for 24 (SA) or 48 (SE) hours at 25°C. (At 48 hours, worms on *S. aureus* have mostly died.) (B) Total CFU/worm in N2, daf-16(mu86), and daf-2(e1370) adults colonized for four days in liquid media on an eight-species minimal native microbiome [48]. C-D) Green fluorescence in individual worms colonized with GFP-expressing bacteria, observed by large object flow cytometry. In (C), synchronized populations of N2 adults were colonized with OP50 (non-fluorescent, n=1908 individual adult worms), *S. aureus* (GFP, n=968), or *S. enterica* (GFP, n=1153) as described in (A); the OP50 control indicates typical levels of green-channel autofluorescence in day-3 adult N2 worms. In (D), synchronized populations of N2 (n=1165), daf-16(mu86) (n=1180), and daf-2(e1370) (n=2267) adults were colonized with commensal *Ochrobactrum* MYb14-GFP for two days on plates as described in (A).(E-F) Day-to-day variation in colonization by *S. aureus* (E) and *S. enterica* (F) (same data as in panel A and figure 2.2, n=48 worms per experiment). The x-axis indicates the day of sampling. Grey horizontal lines represent threshold of detection, defined as the density (40 CFU/worm for single-species colonization, 4 CFU/worm for multi-species colonization, due to different plating volumes) at which probability of observing at least one colony is 60%.

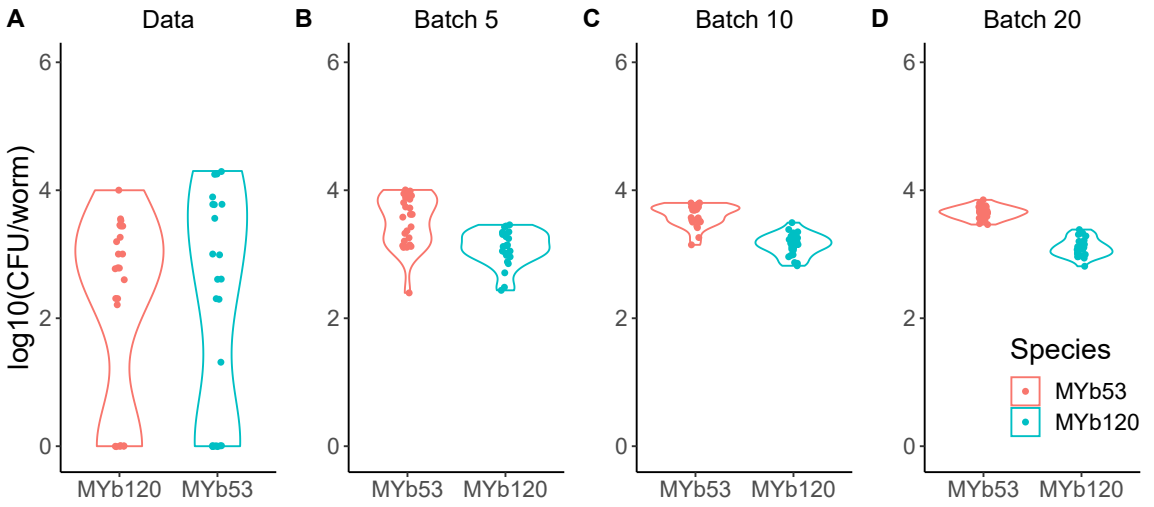

Figure 2.5: Batching erases biological variation in skewed log-scale data. CFU/worm data from Figure 3 were resampled with replacement to create n=25 replicate sets of simulated data for each batch size, where size is the number of individual worms per batch. CFU/worm is the total CFU in each simulated batch divided over the number of worms per batch. In the raw data (panel A), average CFU/worm for MYb53 is 4450.8 ($10^{3.648}$), and for MYb120, 1398.3 ($10^{3.146}$); the batch-inferred numbers converge to these values as batch size increases (B, 5 worms/batch; C, 10 worms/batch; D, 20 worms/batch), consistent with expectations from central limit theorem.

clearly similar in distribution (two-tailed t-test p=0.9, Wilcoxon rank sum p=0.59). When resampling these data to simulate the effects of batch digests, the batch extrapolated CFU/worm pulls toward the upper quantiles of the data due to the positive skew in these distributions (mean > median). As batching effectively averages over the individuals within a batch, batch-extrapolated CFU/worm will center around the arithmetic mean of the individual data, with decreasing distance to this mean as batches become large according to the central limit theorem (Figure 2.5B-D). Accordingly, signal from biological variation is quickly lost; batch-inferred CFU/worm measurements converge toward the average, which is not a representative metric of these log-scale-distributed data. Differences in inferred colonization by MYb53 vs MYb120 quickly become significant in simulated batch digests (t-test batch 5 p=0.049, batch 10 p=2.27e-4, batch 20 p=1.19e-15; Wilcoxon rank sum test batch 5 p=2.27e-4, batch 10 p=2.70e-06, batch 20 p=1.80e-09) as the original signal is obscured.

2.4.5 Effects of individual heterogeneity on microbial transmission

As individual worms show substantial heterogeneity in bacterial colonization, it is reasonable to ask whether this heterogeneity has downstream effects. For example, it is reasonable to expect that transmission might be a function of intestinal bacterial load. By transferring individual surface-bleached worms to a clean environment, it is possible to observe inoculation of the environment with excreted live bacteria. In these experiments, surface-bleached pre-colonized adults, carrying generally substantial populations ($10^3 - 10^5$ CFU/worm, Figure 2.6) of commensal *Ochrobactrum* MYb14-GFP or pathogenic S. aureus-GFP, were allowed to roam on heat-killed OP50 lawns on NGM agar for 1.5 hours. When these worms are re-harvested from excretion plates and disrupted for bacterial quantification, there is no significant relationship between bacterial load and excretion rate of live bacteria (Pearson correlations between log-transformed colonies/hr and CFU/worm: MYb14 rho=0.19, p=0.45; *S. aureus* rho=0.02, p=0.9) (Figure 2.6). Nor is there a significant relationship between presence/absence of colonies on a plate and intestinal bacterial load (binomial logistic regression with log-transformed CFU/worm as factor, p=0.15 with df=53). A substantial fraction of plates remained free of new growth (9/18 plates for MYb14, 10/36 plates for S. aureus), indicating low overall excretion rates.

When worms are allowed to excrete onto agar plates, the actual number of live excreted bacteria per worm is confounded by "farming", where worms pass through colonies and create trails of new growth (Figure 2.7) [92]. A plate with n colonies represents at least one, and at most n, events where live colony-forming bacteria were excreted. From this observation, it is not possible to know how many excretion events in (1,n) actually occurred, nor is it possible to know how many bacteria were excreted in each event. It is therefore not possible to precisely estimate excretion rates of live bacteria from the gut using these data. However, it is possible to infer some bounds.

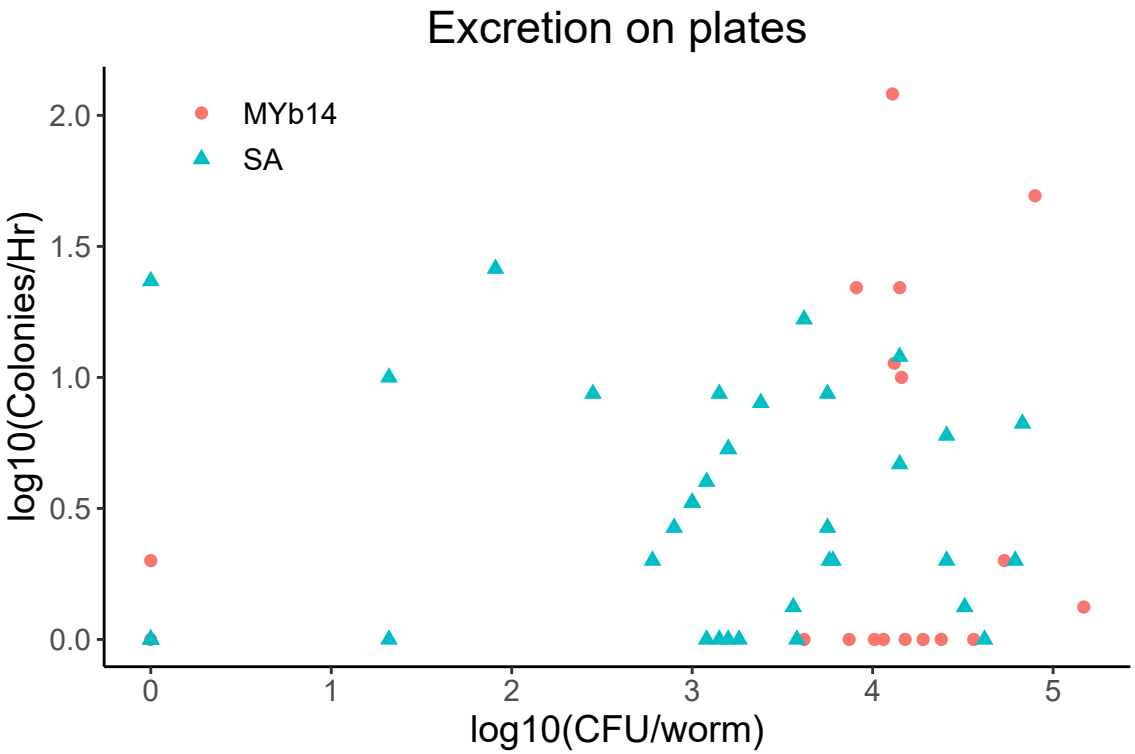

Figure 2.6: Excretion of live bacteria is poorly correlated with CFU load in the intestine of individual worms. Here, N2 adults were colonized by feeding for one or two days respectively on lawns of S. aureus-GFP or MYb14-GFP. Worms with detectable GFP fluorescence (total GFP >1.8 logs on large object flow cytometer) were sorted from the bulk population, surface bleached as described in Methods, and transferred individually to NGM + heat-killed OP50 plates. Pearson correlations between log-transformed colonies/hr and CFU/worm are non-significant (MYb14 rho=0.19, p=0.45; *S. aureus* rho=0.02, p=0.9).

Although the number of colonies per plate is not very informative, presence/absence data can be used for rough inference of excretion rates. For simplicity, if it is assumed that excretion rate of live bacteria is not a function of bacterial load and that excretion is a Poisson process, there is a ∼50% chance of observing at least 9 events in 18 trials when $\lambda \approx 0.33\ worm^{-1}hr^{-1}$ in MYb14. For *S. aureus*, similar plausible rates of $\lambda \approx\ 0.2\ worm^{-1}hr^{-1}$ are obtained. While these rough calculations suggest low rates of excretion of live bacteria, more precise quantification of this process over larger numbers of individual worms will be necessary to obtain reliable estimates.

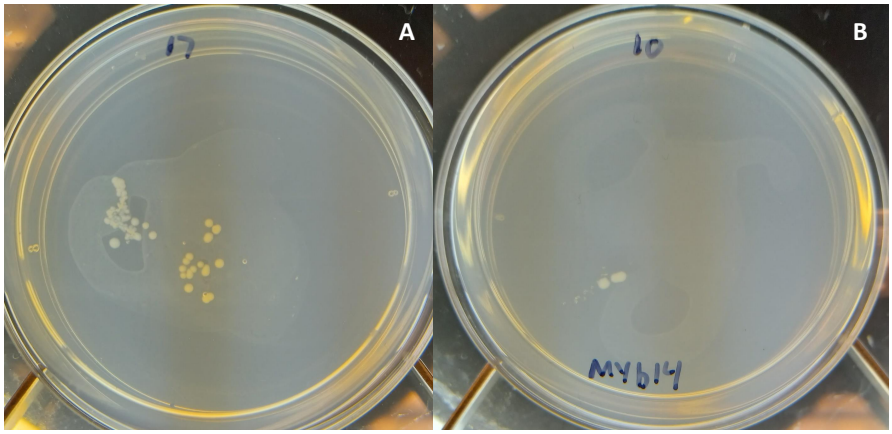

Figure 2.7: Bacterial "farming" obscures the number of excretion events on agar plates. Here are two plates with MYb14-GFP colonies from worm excreta. The first plate (A) has clear evidence of "farming" along worm paths and appears to represent at least two separate excretion events based on differences in GFP expression (visible as yellowish pigmentation) across colonies. While the second plate (B) is more ambiguous, farming cannot be ruled out based on the positions of the colonies. In these experiments, N2 adult worms were pre-colonized for 48 hours by feeding on agar plates containing lawns of MYb14-GFP. After colonization, worms were prepared and surface bleached according to Methods, then transferred in 5 µL aliquots of M9 worm buffer + 0.1% Triton X-100 to 6 cm NGM + heat-killed OP50 plates (prepared by allowing 50 µL spots of 5X concentrated heat-killed OP50 to dry on the surface). Worms were permitted to roam for 1.5 hours at 25°C, then picked from plates and disrupted for CFU/worm plating (manual disruption in 20 µL buffer in individual 0.5 mL tubes, using a motorized pestle). Plates were incubated at 25°C for two days before counting.

2.5 Discussion

Here data are presented on the advantages of single-worm quantification of bacterial load in C. elegans, along with a 96-well disruption protocol to allow the rapid and consistent acquisition of large data sets of this type. As compared with existing methods [88], these protocols allow higher-throughput measurement of intestinal microbial communities in the worm.

This approach has plating as a rate-limiting step and is not truly "high-throughput". Large-object flow cytometry (Figure 2.4B-C) is a useful high-throughput method for

quantifying fluorescently labeled bacteria in individual worms [73], although number of simultaneous fluorophores is a limitation in multi-species communities. Linking multi-well plate disruption with community sequencing is another way to increase throughput; however, the 96-well disruption procedure described here was optimized specifically to leave bacterial cells intact. Sequencing-based analysis, where thorough lysis of cells is desirable, will require addition of a nucleic acid extraction step or modification of the beating protocol to extract cell contents instead of live bacteria. Protocols for single-worm disruption and extraction of nucleic acids have been published elsewhere [93, 94].

Bacterial total abundance in the worm intestine is heterogeneous, and the data shown here suggest that batch-based measurement can produce erroneous results in comparisons between groups. However, other measures of bacterial communities in the worm may be less sensitive to the effects of batching. Of note, relative abundances in worm-associated communities seem to vary very little if at all with total intestinal population size, regardless of whether interactions among microbes are neutral [10] or not [48]. It is plausible that relative abundance measures will be less susceptible to the false-positive rate issue described here than are count data. Sequencing-based community analysis, which generates relative abundance data for community composition, may therefore not require measurement of single worms. Further investigation is needed on this point.

Here we use cold treatment to paralyze worms for surface bleaching. Other work has found that worms resume normal activity rapidly (<15 minutes) if time on ice is kept under 30 minutes, allowing immediate use in further assays, in contrast with chemical paralysis agents which can require extended periods before full recovery[89]. If worms are to be disrupted immediately for bacterial quantification, this feature is dispensable, and the main advantage of chilling vs. chemical paralysis is in avoiding the need for a controlled waste stream. Extended cold treatment should be used

with caution when investigating stress responses, particularly if there is a known connection to temperature. The cold paralysis protocols described here entail shorter acute cold exposure than used in experiments for cold stress (20-30 min vs 2+ hours at 2-4°C)[95, 96, 97], and a one-hour cold shock produces no apparent phenotype in wild-type worms[97]. Short-term (90 minutes) incubation at 4°C induces changes in cold-stress gene expression (measured by expression of a TMEM-135::GFP reporter), but expression returns to unstressed levels within minutes once worms are returned to room temperature[89]. However, the effects on stress-sensitive worm genotypes may be more severe than in wild-type. This procedure should be validated under the experimental conditions to be used.

The surface bleaching protocol described here can be used as a way to limit or eliminate passaging of external microbes in experiments. This method has additionally been used to clear fungal contaminants by surface bleaching and transferring only L1/L2 larvae to fresh plates (transfer of surface-bleached adults resulted in failure to clear the contaminant, presumably due to carriage in the intestines of the larger animals). It is critically important to ensure that bleach concentration does not exceed 1:1000 v/v, as damage to the worms and mortality will result. This procedure may be useful in experimental host-microbe evolution and host-pathogen interactions. For example, the low excretion rate of live bacteria observed here can help to explain the highly variable rates observed for bacterial transmission from hermaphrodites to offspring[72]. The lack of correlation between intestinal bacterial load and excretion rate observed here is interesting but requires further investigation; a larger number of data points across a range of conditions will be needed to determine where (or whether) this observation will hold.

It may not always be necessary to clean worms to the extent provided by surface bleaching. Multiple washes in sterile buffer are likely sufficient when worms are internally colonized with a single microbe if the minimum expected CFU/worm is much

higher (10-100 fold) than the concentration of bacteria in buffer supernatant, as this carryover will minimally affect counts (see Figure 2.2). Additionally, if the microbe(s) of interest primarily colonize the cuticle, surface bleaching should clearly be avoided. Thorough cleaning is more important to ensure accuracy when dealing with mixed microbial communities (to ensure that all colonies/reads in a sample are from worm-associated bacteria and not from the environment), when bacteria adhered to the cuticle interfere with reading the internalized population, when expected minimum CFU/worm is low, etc.

Chapter 3

Maximum Likelihood Estimators For Colony Forming Units

This chapter is adapted from a previously published paper [98].

3.1 Summary

Measuring the abundance of microbes in a sample is a common procedure with a long history, but best practices are not well-conserved across microbiological fields. Serial dilution methods are commonly used to grow bacterial colonies in small enough numbers to count and, from these counts, to infer bacterial concentrations measured in Colony Forming Units (CFUs). The most common methods to generate data for CFU point estimates involve plating bacteria on (or in) a solid growth medium and counting their resulting colonies, or counting the number of tubes at a given dilution that have growth. Traditionally, these types of data have been analyzed separately using different analytic methods. Here we build a direct correspondence between these approaches, which allows one to extend the use of the Most Probable Number (MPN) method from the liquid tubes experiments, for which it was developed, to the growth plates by viewing colony sized patches of a plate as equivalent to individual tubes. We

also discuss how to combine measurements taken at different dilutions, and we review several ways of analyzing colony counts, including the Poison and truncated Poison methods. We test all point estimate methods computationally using simulated data. For all methods, we discuss their relevant error bounds, assumptions, strengths, and weaknesses. We provide an online calculator for these estimators.

3.2 Introduction

Extrapolation of viable microbial counts from suspensions of live cells is a longstanding—and surprisingly complicated—problem, which here we will explore computationally. The fundamental problem is simple: there exists a sample with some unknown concentration of live microorganisms, which an experimentalist wants to measure. For simplicity, we will assume that the sample in question was taken as, or has been re-suspended into, some initial volume. That initial volume will be serially diluted (usually in a ten-fold series), and fixed-volume aliquots (or sub-samples) of the resulting suspensions will be cultured. If these aliquots are plated in or on agar, the resulting data will be in the form of colony counts (colony forming units, CFUs). Alternately, multiple aliquots may be taken from a single dilution and used to seed a number of wells or tubes of liquid culture, or a number of plates. Then the number of volumes showing growth when seeded from a particular dilution, as a fraction of the total number of volumes inoculated, can be used to calculate the Most Probable Number (MPN) of live agents in the initial volume [99, 100].

Best practice for this apparently simple and ubiquitous scenario has been the subject of debate for over a century [99, 101, 102, 103, 104, 105, 106, 107, 108, 109, 110, 111, 112, 113, 114]. CFU measurement is inherently subject to errors due to the stochastic nature of counts. This type of error is the primary concern in research settings, where microbes are grown in culture prior to quantification. For reasons

that are not clear, the substantial literature on microbial quantification in food and environmental samples is not well known in research laboratories, and the practices and estimators used vary considerably from lab to lab.

Counting error is related to the density and number of colonies. At one extreme, when the sample is too concentrated, the number of resulting colonies will be too numerous to count (TNTC; sometimes "too many to count", TMTC). At these high concentrations, colonies merge, breaking the assumption that each microbe corresponds to one colony [104, 115]. At the other extreme, when the sample is very diluted, the number of colony initiating bacteria in the sample is subject to small-number statistical (sampling) fluctuations, resulting in high relative error (ratio of the standard deviation to the mean) [116, 117]. Crowding error is widely acknowledged, and TMTC colonies or plates are generally simply excluded from analysis (although there are uses for these data, see for example [118]). However, understanding of small number errors is less common in wet-lab microbiology. Finally, experimental errors, such as inaccuracies in pipetting, can emerge and compound over the steps of a serial dilution. However, the latter source of error is expected to be negligible for equipment calibrated to usual standards, and technical replication further reduces effects of this variation [119].

Thus the problem at hand is: How can CFU density best be estimated from plate counts, given the error produced by sampling fluctuations, colony crowding, and (to a lesser degree) pipetting? These errors will contribute differently to different experimental designs. For a *single sample with initial volume V_0 which is represented by one count of colonies* n_k at one dilution d_k (because only one dilution was measured, or because only one spot or one plate in a series was countable), statistical error of counts (presumably but not necessarily [120, 121] Poisson) is inevitable, and pipetting error will contribute but may not be significant.

For a *single sample represented by more than one count of colonies* (representing

counts at different dilutions within a single dilution series, and/or technical replicates where one sample was measured multiple times), the same errors apply, but pipetting bias may not be constant across measurements (for example, one failing O-ring on a multichannel pipette can lead to bias in a single column of a 96-well plate). If technical errors are reasonably small, these measurements should conform to expectations for Poisson sampling error [122].

It is critical to note that for *multiple samples of the same type measured in parallel* (including biological replicates), we can no longer expect variation across samples to reflect a Poisson-distributed sampling error. Variation across samples will be biological (or otherwise inherent) and demographic (accumulating over time) in addition to that due to sampling. This was the basis for the Nobel-prize winning experiments of Luria and Delbrück, who used the distribution of fluctuations to distinguish Darwininan vs. Lamarckian evolution [123]. This is also frequently the case in environmental samples, where different samples from the same source (e. g., water samples from different parts of the same lake) will produce measurements that have super-Poisson variation (aka, over-dispersed). In such cases, a substantial part of the variation is "real" due to inhomogeneities in the source [124] and counts may be better represented by a lognormal or negative binomial distribution [120, 121] than by the Poisson [124].

These considerations are substantial. Sample inhomogeneity is known to be a major source of variation between measurements in environmental and food samples [125, 120]. Even apparently "well-mixed" samples, such as water samples or liquid cultures in a laboratory, can be very inhomogeneous especially if microbes have a tendency to clump [117]. However, such considerations are case-specific, and dealing with these is beyond the scope of the present work. The larger problem of microbiological estimation from varied and inhomogenous samples has been dealt with extensively elsewhere, for example Ref. [120, 116, 126].

Here we will focus on point estimation of CFU density within an individual, ho-

mogeneous sample, which may be represented by a single set of measurements or by technical replicates, in which one sample is measured multiple times. The main objective of this paper is to propose methods for accurately estimating colony forming units (CFUs), while taking into account the effects of crowding and sampling fluctuations, without losing valuable data from counts. Drawing from previous research [116, 115, 127, 117], we present simple analytical formulas that can be used to combine counts from different dilutions and to obtain precise CFU point estimates along with accurate error bars. First, we examine existing point estimate methods in the literature, assessing their strengths and weaknesses including pick-the-best, Poisson, and Poisson with a cutoff. We discuss the "Poisson with a cutoff" method, which clarifies the impact of crowding on CFU density estimation and demonstrates how to minimize the effects of sampling error by combining measurements of "uncrowded" counts. We explore the mathematical equivalence between different regimes of the common CFU estimators. Next, we introduce a crowding-explicit model to demonstrate the relationship between canonical plate-based counts and the Most Probable Number method for presence/absence of growth in liquid media. This is achieved by considering colony sized patches of the plate as equivalent to individual tubes. This extension of the domain of applicability of MPN to colony counts will potentially increase the accuracy of a whole class of experiments with no additional experimental costs. Finally we computationally evaluate and compare all the point estimators we discussed for their bias and standard errors. If experimentalists require estimates beyond point estimation such as full distributions or need to include experimental uncertainties in the counting process, more detailed methods are available in the literature[117]. However, if an experimentalist just requires a point estimate of the CFU density we provide practical recommendations for experimentalists on how to select appropriate dilution and replication schemes and how to combine data from multiple observations. We also have provided a calculator for these estimators available on `Hugging Face`

spaces, named `CFUestimator` [128].

3.3 Results

3.3.1 A Brief History of Counts

Colony Forming Units (CFUs) are a proxy for the concentration of microbes within a sample. A standard experimental procedure for estimating CFUs consists of serially diluting homogeneous samples in a sterile aqueous buffer, then plating aliquots of these dilutions on growth-supporting agar and later counting the resulting colonies. If an appropriate dilution has been reached, each microbe will form an independent colony that is countable by eye. We assume for simplicity that all plates or tubes used for growth have the same ability to support growth of the organism(s) being studied, and that the sample is sufficiently homogenized to ensure that microbes are free in solution and not adhered to one another or to a substrate [102]. (In practice, these assumptions should be tested before choosing an estimator [124, 116]; we discuss one such test in the next section.)

The simplest way of estimating CFUs is to multiply the number of colonies by the reciprocal of the dilution factor to find the concentration of colony-forming microbes in the original suspension [99, 103, 127]. For example, say there is a single sample represented by one countable 10 cm plate in a dilution series, where we observe 100 distinct colonies after plating 100 μL of a 1:100 dilution (dilution 2 in a ten-fold series) from the original sample. In this case, following this simple procedure, we would obtain:

$$\frac{\text{CFU}}{\text{Volume}} = \frac{\text{counts}}{\text{FracOriginalVolume}} = \frac{100}{0.1\text{mL} \cdot 0.01} = 100 \cdot 10^3 = 10^5\,\text{CFU/mL}. \quad (3.1)$$

This is exactly equivalent to multiplying the number of counts by a volume correction

factor (1/(size of aliquot in mL)) and multiplying by the base of the dilution series raised to the power of the number of dilution steps:

$$\frac{\text{CFU}}{\text{Volume}} = \frac{1}{0.1\text{mL}} \cdot 100\,\text{colonies} \cdot 10^2 = 100 \cdot 10^3 = 10^5\,\text{CFU/mL}. \tag{3.2}$$

This simple calculation follows from a more general Poisson model, explained below. This method works reasonably well under ideal conditions: all samples should be represented by a single count of colonies, and each count should be large enough to minimize small-number sampling fluctuations, and yet small enough to avoid crowding on the plate. When any of these conditions are not met, accurate estimation of CFU density becomes more complicated.

There is a broad literature of methods proposing to ensure that estimates of CFU density are "good". A *good* estimator should be accurate. Formally, this means that such estimators should have the true value of the CFU density as their expected value. In other words, they must be unbiased. *Good* estimators must also be precise, so that variance in the estimate is small and samples are repeatable. Therefore, an ideal solution to this problem should provide an estimator that is provably unbiased and with a minimal variance. The solution to this problem is well known in statistics: if we can assume that data follows a specific probability distribution, then the *maximum likelihood estimator (MLE)* for that distribution will have these properties[116]. While this is formally true only for very large samples, MLE estimators generally perform well even for relatively small samples. Further, an ideal method should be straightforward to use in the hands of researchers without advanced mathematics background. Unfortunately, many of the available methods fail one or the other of these requirements, being either simple to use, but statistically sub-optimal, or mathematically correct, but incomprehensible to many bench scientists.

Straight-forward to use methods focus largely on designing protocols that avoid

data in error-prone extremes. For example, the FDA recommends [129] that the best dilution range for coliform bacteria results in 25 to 250 colonies per 10-cm spread plate, with the ideal count closest to 250. Restriction on the high end limits counting errors due to growth limitation by nutrient depletion as well as outright merging of colonies, which would bias the number of counts downward. Conversely, restriction on the lower end limits the sampling error associated with small numbers of counts. Specifically, under the assumption that counts represent random draws from a given sample and are, therefore, Poisson-distributed, the error scales as the square root of the number of counts. Thus, for small counts, the error becomes an unacceptably large fraction of the mean. Within the example above, our dilution 2 count of 100 colonies should have a standard deviation (SD) of $\sqrt{100} = 10$, giving a coefficient of variation (CV) of 10%. At dilution 3, we might obtain 10 counts, with a SD of $\sqrt{10} \approx 3.16$, and a CV of 31.6%.

From here, the simplest approach that is often used in practice is to choose only the plate or spot that has the "best" count in the acceptable range, and to estimate CFU density based on that single count. Often only the dilution at the high end of the countable range is used since it has the smallest sampling fluctuations; all other measurements are discarded [127]. We call this the "pick-the-best" method for later reference. If counts in the acceptable range can be consistently achieved, this method is straightforward and reasonably accurate. However, discarding data is rarely advisable, and over- and under-crowded measurements can, in fact, be used to improve CFU estimates.

3.3.2 Simplest "Good" Estimator: Poisson

One simple and reasonably accurate model for calculating CFUs assumes that the number of colonies are Poisson distributed, with variation due to sampling. That is, for a particular dilution, the mean colony count for that dilution is the same as

the variance. By this model, the most likely estimator for the density of microbes is simply the ratio of the total number of colonies counted from all plates divided by the total amount of liquid used from the original sample in all plates (see *Supplementary Information*). If there is only one countable measurement for a given sample, this simplifies to "pick-the-best".

The Poisson model implicitly assumes that the original sample is well mixed and each microbe plated will result in its own separate and countable colony. It further assumes that experimental volume is spread uniformly across the agar surface, resulting in cells being randomly distributed, independent of the locations of where other cells landed. Formally, these assumptions mean that there is a uniform and well mixed population density r of microbes per unit volume in an initial volume of liquid V. The liquid is diluted by a factor $d_k = V_k/V$, where V_k is the volume of the liquid from the original sample used on the plate or the spot k. Plating will result in n_k colonies, where n_k is Poisson distributed with the parameter $\lambda = rd_kV = rV_k$. That is, the average number of colonies per experiment is rd_kV with variance rd_kV. Using these assumptions, the MLE estimator of the density of microbes r_{mle} and its standard error are:

$$r_{\text{mle}} = \frac{\sum_k n_k}{V \sum_k d_k} = \frac{\sum_k n_k}{\sum_k V_k}, \qquad \sigma = \frac{r_{\text{mle}}}{\sqrt{\sum_k n_k}}. \tag{3.3}$$

In other words, the best estimator for the concentration, r_{mle}, is the total number of colonies divided by the total amount of the original volume of liquid used. However, as noted earlier, this ignores crowding and counting errors. In practice, this method should be avoided unless all measurements are from well-dispersed, uncrowded plates, as crowding effects can make a large difference in the estimator, resulting in underestimating the microbial density as colonies merge and are under-counted.

If technical replicates exist (multiple measurements of the same sample; four or

more such measurements are recommended), it is straightforward to test whether the data adhere to a Poisson distribution using the following test, known as the dispersion index test. If there are j measurements of a given sample, with average number of counts $\bar{N}$ and variance of counts s_N^2, then the index of dispersion D^2 is:

$$D^2 = \frac{(j-1)s_N^2}{\bar{N}}, \tag{3.4}$$

which will be distributed as χ^2 with $j-1$ degrees of freedom [116, 130]. If D^2 is greater than the upper $1-\alpha$ quantile of that distribution, where α is the needed significance p-value, then we reject the null hypothesis that these replicates are drawn from the same Poisson distribution. This can indicate technical problems that are introducing an excess (or insufficiency) of variation, possibly by biasing replicates differently from one another (e. g., the failing O-ring example above), or biases due to a too-lenient cutoff for countability.

3.3.3 Combining Data: Common Bad Estimators

The primary reason for the "pick-the-best" approach is that it eliminates confusion over how to combine multiple measurements for a given sample, particularly when counts belong to more than one dilution. First notice that combining measurements from technical replicates that are taken at the same dilution is straightforward. For example, let's assume an original 200 μL volume V contains $r = 3 \cdot 10^8$ CFU. We can create simulated serial dilutions from this original volume by assuming that each pipetting step (ten-fold dilutions and plating onto agar) is a binomial sampling event [117] that comes with experimental noise. In one such simulation, triplicate plating 100 μL aliquots results in counts n_6 =(162, 141, 148), all from the sixth ten-fold dilution. The fraction of the original volume plated in each case is $V_6 = 0.5 \cdot 10^{-6} = 5 \cdot 10^{-7}$. These numbers can be combined via the Poisson method shown in the

previous section to estimate CFU density in V:

$$\text{CFU} = \frac{162+141+148}{5\cdot 10^{-7}+5\cdot 10^{-7}+5\cdot 10^{-7}} = \frac{162+141+148}{3\cdot 5\cdot 10^{-7}} = 3.007\cdot 10^{8}. \tag{3.5}$$

Alternately, counts taken from the same dilution can be averaged across technical replicates, then adjusted by the volume plated and the dilution read [131]:

$$\text{CFU} = 2\cdot\frac{162+141+148}{3}\cdot 10^{6} = 2\cdot\frac{162+141+148}{3\cdot 10^{-6}} = \frac{162+141+148}{3\cdot 0.5\cdot 10^{-6}} = 3.007\cdot 10^{8}. \tag{3.6}$$

Clearly, these two most common approaches are algebraically identical.

In contrast, combining counts across different dilutions is less straightforward. In fact, some commonly-used methods for combining measurements are statistically inadmissible. For example, if there are multiple measurements in the countable range, the USDA FSIS recommends [131] that researchers calculate the estimated CFU for each dilution separately using the average colony count across technical replicates at a given dilution and then average the results of the separate dilutions. If the two estimates are more than a factor of 2 apart, the researcher is instructed to instead only use the counts from the higher-density plates. This commonly used method incorrectly combines the data using a simple average, thus increasing the variance of the estimated CFU density. Indeed, continuing the example above, let's suppose that, on the plates corresponding to the seventh ten-fold dilution from these three technical replicates, we observe (13, 17, 20) colonies. The Poisson estimator gives us:

$$\text{CFU} = \frac{162+141+148+13+17+20}{3(5\cdot 10^{-7})+3(5\cdot 10^{-8})} = 3.036\cdot 10^{8}. \tag{3.7}$$

The USDA averaging method gives:

$$\begin{aligned} \text{CFU} &= \frac{1}{2}(2\frac{162+141+148}{3}\cdot 10^6 + 2\frac{13+17+20}{3}\cdot 10^7) \\ &= \frac{1}{2}(3.06\cdot 10^8 + 3.33\cdot 10^8) = 3.2\cdot 10^8. \end{aligned} \tag{3.8}$$

On these data, averaging was substantially less precise, with an error of 7% as compared with the Poisson method's error of 1% (recall that the true density in this example is $3.0\cdot 10^8$ CFU per 200 μL). The USDA method improperly averages across dilutions, amplifying fluctuations associated with small colony number counts, whereas the simple Poisson model properly combines measurements across dilutions by effectively re-weighting small counts by the small volumes with which they are associated. In a later section, we demonstrate that averaging across dilutions will, as a rule, increase the variance of CFU estimates.

3.3.4 Too Few and Too Many

Further, there is the problem of what to do with zero counts. These data are inevitably limited by some threshold of detection (TOD), representing the smallest CFU density at which counts can be detected. This "left-censoring" is a well-known issue [132, 133, 134] with many proposed work-arounds, including but not limited to: substituting zeros with a small value (which may be the average of the undetectable range, a maximum-likelihood inferred value, or some other small number), reporting zeros as "below TOD" or "<1" rather than as a value, and pretending they didn't happen (not generally recommended; although if zeros are rare, it won't make much difference) [132, 134]. Sometimes, a threshold of quantification (TOQ) representing the lowest "acceptable" (sufficiently precise) count is used along with or instead of TOD [127], with values below this threshold omitted from analysis.

The "best" approach to zero-contaminated count data depends on what else is

in the data and what the data will be used to do. We assume here that the goal is to obtain a point estimate of CFU density in the original sample (as opposed to, for example, determining the probability that this density is in excess of some threshold). If a sample is represented by zero and non-zero measurements, the Poisson model explicitly allows zero counts to be incorporated as outcomes of the random sampling process. For example, if a hypothetical $V = 200$ μL sample contains $5 \cdot 10^7$ CFU, one simulation of serial dilution and plating in triplicate with 100 μL per plate produces dilution-6 counts of (31, 26, 20) and dilution-7 counts of (4, 0, 0). Using just the dilution-6 counts, we estimate

$$\text{CFU} = \frac{31 + 26 + 20}{3(5 \cdot 10^{-7})} = 5.13 \cdot 10^7 \pm 0.59 \cdot 10^7. \tag{3.9}$$

If we use the lower dilution as well, we obtain

$$\text{CFU} = \frac{31 + 26 + 20 + 4 + 0 + 0}{3(5 \cdot 10^{-7}) + 3(5 \cdot 10^{-8})} = 4.91 \cdot 10^7 \pm 0.55 \cdot 10^7. \tag{3.10}$$

In this case, incorporating data from zeros (in the form of the additional volume that was plated but contained no counts) improved precision. Alternately, when zeros are common because the density in the original sample is close to the TOD, non-zero counts are useful for making a distinction between samples where no organisms are detectable (and density might be zero) and those where the density of organisms cannot be zero. Although the actual density cannot be estimated accurately or precisely from very low counts, the distinction between "<TOD" and ">1" for a given sample is important [134].

At the other end of the range, researchers must deal with crowding and set thresholds for "too many to count". Defining an optimal range for "countable" data is not always straightforward, and this determination is very important to ensure that CFU estimates are accurate. Since the sampling-based standard error of counts scales as

$\frac{n_k}{\sqrt{n_k}}$, the number of colonies counted n_k should be as large as reasonably possible.

However, there are consequences for pushing this too far. As cell density in the aliquot increases, counts will be biased downwards due to merging of colonies and colony stunting or failure to grow. These data are then "right-censored", with an upper limit past which the number of counts observed does not increase in proportion to an increase in the density in the original sample. Densities above this point result in "crowded" samples, with counts that are lower than the true number of colony forming units. Further, as the number of colonies per plate or spot increases, data collection becomes more time-consuming or requires expensive robots for automatic counting; it is common for researchers to minimize effort on plates near the top of the "acceptable" range by dividing plates into sections, counting colonies in one section, and multiplying this count by the number of sections to get an estimated final count for the whole plate. While this approach is sufficient for a rough estimate of CFU density, it introduces additional sampling variation due to both reduction in counts and imperfect division of plates, and it does not remove bias due to crowding. We will demonstrate the consequences later in this paper.

Previous works [115] have modeled crowding using shifted Poisson distributions. In these models, the variance of estimates from crowded data would be the same as if there was no crowding and the mean would be shifted down due to colonies merging together. However, this is *a priori* unlikely to be true. As we will show below, if colonies are crowded, both the mean and the variance will be shifted relative to the pure Poisson (uncrowded) distribution. The reason for this is that the variance of the large colony counts is shifted downward due to a "ceiling" effect—there is an upper bound to the total number of colonies, which limits upwards fluctuations. In other words, the use of a shifted Poisson distribution is a reasonable approximation, but the variance must also be modified.

3.3.5 Better Estimators: Poisson With Cutoff, aka What's Countable, Exactly?

The main problem with the naive Poisson model is that it does not account for counting errors due to crowding. The simplest way to take account of the crowding is to assume that there is a threshold of colonies, M, below which crowding is negligible, which in practice will often be smaller than the largest number of counts we are willing to attempt (TMTC). It is convenient to assume that this threshold M is the same as some TMTC threshold (e. g., the commonly referenced 250-300 colonies per plate for coliforms). However, this threshold will depend on colony size and morphology, which will vary across different bacteria and will change for a given bacterial strain depending on the media used, concentration of agar in a given batch of plates, incubation time and temperature, humidity, etc. To be certain of the validity of a chosen threshold within a standardized protocol, it is advisable to plate a finer-than-normal dilution series (two to five-fold, to ensure multiple dilutions with readable counts) and check that dispersion within and across different "countable" dilutions for a given sample is consistent with Poisson. For densities where crowding affects counts, the data will become "right-censored" and show a *decrease* in variation as compared with expectations for Poisson-distributed samples.

Once the threshold M is determined, we can then segment our data into two parts: plates/spots with counts above the threshold where crowding is important, and plates/spots with counts below this threshold for which crowding is not important. If we have identified our cutoffs well, for our theoretical homogeneous sample, the Poisson estimator is correct for all measurements k where the number of colonies counted $n_k \leq M$. The calculation is, therefore, exactly the same as for the naive Poisson estimator, with the caveat that only measurements $n_k \leq M$ are used. Here, the indicator function $I(n_k < M)$ is 1 when $n_k < M$, and 0 otherwise. Similarly, $I(n_k > M)$ is 1 when $n_k > M$, and 0 otherwise. Due to its balance between simplicity

and accuracy, this method is the easiest to use in practice.

$$r_{\text{mle}} = \frac{\sum_k I(n_k \leq M) n_k}{\sum_k I(n_k \leq M) V_k}, \qquad \sigma = \frac{r_{\text{mle}}}{\sqrt{\sum_k I(n_k \leq M) n_k}}. \tag{3.11}$$

If we want to incorporate data from measurements above this threshold M, the calculation becomes slightly more complicated. This method was first introduced in the literature as "averaging TNTC counts" [116, 118]. Using "crowded" measurements as if they were uncrowded will bias the naive Poisson estimator downward, resulting in under-estimation of CFU density (Figure 3.2). However, we can use the *number* of plates/spots that were above the crowding threshold M, along with the colony counts from plates/spots below this threshold at the same dilution, to estimate CFUs. This will be applicable when plate counts at a given dilution are toward the high end of the countable range, such that some technical replicates fall below this threshold and others above it by chance. To estimate the CFU density in the original sample r, the following equation should be solved numerically :

$$\sum_k I(n_k \leq N) \left(\frac{n_k}{r} - d_k V \right) + \sum_k I(n_k > N) \frac{d_k V (d_k r V)^N e^{-d_k r V}}{\int_0^{d_k r V} t^N e^{-t} dt} = 0. \tag{3.12}$$

The first term is equivalent to the simple Poisson model and uses the counts from uncrowded samples directly, whereas the second term reflects the probability of counts being above the threshold M. Inference of r can be done in Excel using SOLVER or using numerical solvers in R, Python, MATLAB, etc. An equivalent model is shown in [116, 118].

This model properly accounts for two error sources in counts from an individual sample: the sampling fluctuations and the crowding effect. The simple Poisson, using only counts from uncrowded plates, gives a good estimate for the CFU counts and properly combines multiple measurements at different dilution factors. The more sophisticated form of the model has greater precision, but the greater computational

effort may or may not be worth it to an investigator depending on the effect size and the structure of the experiment. In the next section, we present an alternate estimator based on the Most Probable Number approach, which we argue provides a better trade-off between effort and estimator performance when incorporating data from crowded samples.

3.3.6 Crowding and the Most Probable Number

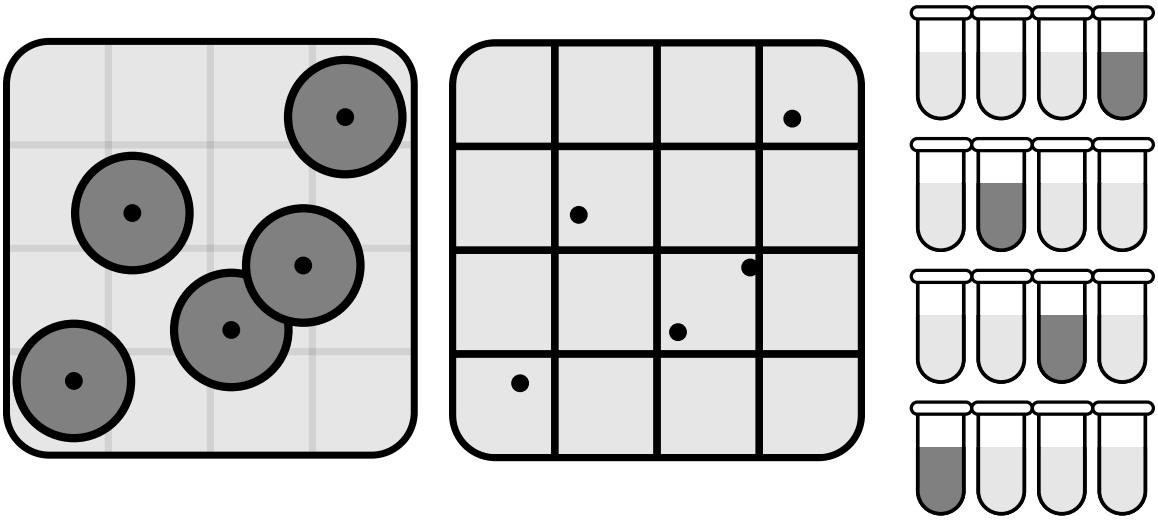

Figure 3.1: Visual equivalence between plate and tube based assays. The left panel is a cartoon of a typical plate containing colonies, where the growing colonies are shown as dark disks. In the middle panel, the plate is divided into N (here 16) approximately colony-sized regions. If a region contains one or more colony centers (black dots), this region can be mapped to a positive (dark) tube as shown in the right panel. Similarly regions containing no colony centers are mapped to negative (light) tubes. This demonstrates that plating is equivalent to a massive parallel version of a tube based assay with $N \approx \frac{A_{\text{plate}}}{A_{\text{colony}}}$ tubes. Furthermore it demonstrates that the MPN method can be used for plate data.

For the final model we consider the effects of crowding in space. To account for crowding, we will divide each plate into $N \approx \frac{A_{\text{plate}}}{A_{\text{colony}}}$ regions, each approximately the size of a full colony. We make the assumption that if more than one microbe lands in one of these regions, the colonies that form from these cells will grow together and be counted as one colony. For each region, the number of cells landing in that region

will be Poisson distributed with parameter $\lambda = \frac{d_k r V}{N}$.

These assumptions are equivalent to that of quantal-based methods for microbial quantification, such as the commonly used Most Probable Number (MPN) method. In the MPN assay, a known quantity (volume of original sample) is introduced into each of a series of N replicate tubes, and the dilution of the original sample is adjusted to find a region where some of the tubes contain viable growth and some do not. The results of this assay are therefore, for each dilution volume V_k from the original sample, out of the N_k tubes inoculated, a number n_k that is positive for growth.

A direct mapping to tube-based assays is possible if space on a plate (or within a spot) is considered as a set of colony-sized bins. Each of the N colony-sized regions on a plate or within a spot corresponds to one tube. The presence of colonies in a particular region corresponds to when a tube has growth. Hence a plate that is divided into N regions can be thought of as N tubes being tested in parallel (Figure 3.1).

Therefore, the probability of n_k successes in N colony-size regions on the agar surface can be described using a crowding-explicit model based on the binomial distribution. Assuming that the cells in the original sample are well-mixed, the probability of zero cells landing in a particular region is (from the Poisson) $p_0 = e^{\frac{-d_k r V}{N}}$ and the probability that at least one cell lands in that region is therefore $p_> = 1 - e^{\frac{-d_k r V}{N}}$. Assuming that the original sample is well mixed, each region is independent of all other regions in our crowding model, so that

$$p(n_k) = \binom{N}{n_k} p_>^{n_k} p_0^{N-n_k} = \binom{N}{n_k} (1 - e^{\frac{-d_k r V}{N}})^{n_k} e^{-d_k r V (N - n_k)}. \tag{3.13}$$

We can maximize this probability to find the MLE CFU density, r_{mle}). We can accomplish this by numerically solving the following equation for r:

$$\sum_k \frac{d_k n_k}{N(1 - e^{-r d_k V/N})} = \sum_k d_k. \tag{3.14}$$

This expression for r is the same as that of the MPN estimator[129, 135, 136]. In the limit where concentrations and colony counts are low, this model simplifies to the Poisson model. Outside the "uncrowded" regime, the mean and the variance of data from the crowding model are not the same as in the Poisson. Therefore, the two approaches are not equal to each other, though both are depressed due to the "ceiling" effect described earlier. We also find that the error associated with the maximum likelihood estimator r_{mle} of the MPN method can be minimized at an optimal dilution factor, which falls into the crowded regime.

The MPN procedure can generate biased estimates of the original sample density, and the precision and accuracy of results depend strongly on the number of tubes used [116]. The bias on the maximum likelihood estimator results in an over-estimate of 20-25% with 5 tubes, which is reduced to a few percent with 50 tubes. By back of the envelope calculation, an average 10 cm plate (inside diameter 86 mm, surface area 58 cm^2) can fit a maximum of approximately 5000 medium-sized (1 mm outside diameter) "tubes", whereas a single grid square on a 10 x 10 cm square plate (typically gridded 6 x 6) can fit 200 of these colony-sized spaces. All of these are well above the threshold where the bias in this estimator [137] makes much difference in the value. (Note that this refers to the number of *colony-sized spaces* available and is independent of the number of colonies observed.) This also means that the standard error of the estimator will, in theory, be minimized at a plating density that is much higher than the threshold for "uncrowded" plates and, in fact, is well into a range of densities where a minority of colonies will be distinct. Fortunately, the standard error is still well behaved over a broad space in fraction of regions occupied , meaning that plate counts into the "uncrowded" range will still produce good estimates with this method. In fact, this produces a result equivalent to that of the Poisson method in the fully uncrowded regime. However, the MPN method is most useful as plating densities encroach into the crowded regime, allowing precise and accurate estimation

of CFU density from plates that would provide severely biased estimates using a naive Poisson model.

3.3.7 Utility of the Models

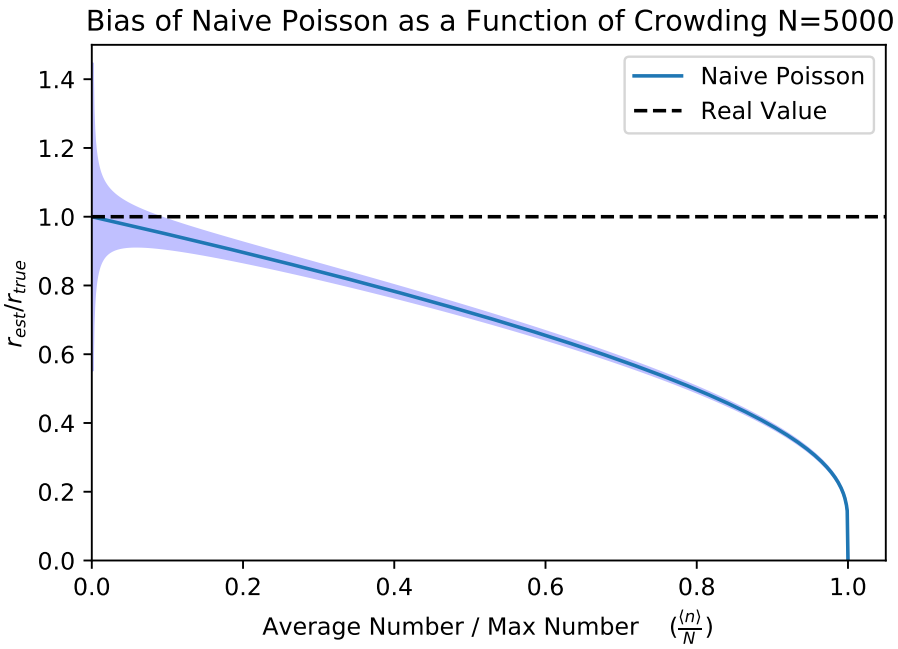

Figure 3.2: Bias and under-estimation of the true bacterial concentration as a function of crowding, illustrated using the Poisson estimator. We illustrate this by plotting the ratio of the estimated concentration (with the error bands denoting $\pm$ one s. e. m. at $N = 5000$) to the true concentration. Here crowding is measured by the ratio of the average number of colonies to the maximum number of colonies that can fit within a plate $f = \frac{\langle n \rangle}{N}$. At low crowding values (encompassing the conventionally recommended 25-250 colonies per plate), the naive estimator has low bias, but large uncertainty. At a crowding value of 0.2 ($\sim$1000 colonies on a 10 cm plate - an ambitious task, and not recommended) the naive-Poisson estimator underestimates the true concentration by about 10%, and many-fold underestimation is possible as crowding approaches 1.

Here we demonstrate the relative utility of each model for estimation of CFU density from simulated data. First, we can use the crowding-explicit binomial sampling model described in the previous section, to estimate bias due to crowding, and to demonstrate the importance of choosing an appropriate cutoff M, below

which plates are considered to be uncrowded and countable. To do so, we solve the crowded binomial model in Eq. 3.13 for dV with respect to the average number of colonies $\langle n \rangle$ and the number of colony-sized regions on a plate N. Doing so we find $dV = \frac{-N}{r} \log(1 - \frac{\langle n \rangle}{N})$. We can substitute this into the Poisson estimator and find:

$$r_p = \frac{\langle n \rangle}{dV} = \frac{\langle n \rangle}{\frac{-N}{r} \ln\left(1 - \frac{\langle n \rangle}{N}\right)} = -r \frac{\frac{\langle n \rangle}{N}}{\ln\left(1 - \frac{\langle n \rangle}{N}\right)}. \tag{3.15}$$

Let us define the ratio of expected colony number to the number of colony-sized regions as $f = \frac{\langle n \rangle}{N}$. This ratio represents the amount of crowding, where a value of 1 is the maximum crowding and a value close to zero is in the uncrowded regime. Expressing the previous expression in terms of the crowding we see

$$\frac{r_p}{r} = -\frac{f}{\ln(1 - f)}. \tag{3.16}$$

This ratio indicates how close the estimated CFU concentration is to the true concentration. A ratio of 1 tells us that we have an unbiased estimator, whereas a ratio of less than 1 tells us we are underestimating the CFU density. We plot this expression in Figure 3.2 to show how the simple Poisson estimator underestimates the actual concentration as a function of crowding, f. After a crowding value of $f = 0.2$ the Poisson estimator starts to be significantly biased, undershooting the true value by about 10%. This has implications for the value used in the Poisson model with a cutoff. The cutoff should be chosen such that the bias is not greater than the experimenters targeted precision. For example, if a bias must be less than 10%, then a cutoff of about 20% of the total plate capacity should be used. In the case of a 10 cm plate with an estimated 5000 1mm diameter colony-sized regions, this corresponds to a cutoff of $M = 1000$, whereas the more typical cutoff of $M = 300$ provides an essentially unbiased estimate (bias 3%), but this results in a large statistical fluctuation

of 5.8%. In the case of a 6 by 6 mm grid on a 10cm by 10cm plate, there are roughly 200 grid regions in a plate. Thus an $M = 40$ would be appropriate to achieve bias less than 10%, and a threshold of $M = 12$ colonies is required to reduce bias to 3% for colonies of this size. At these thresholds, the statistical error would be 15.8%.

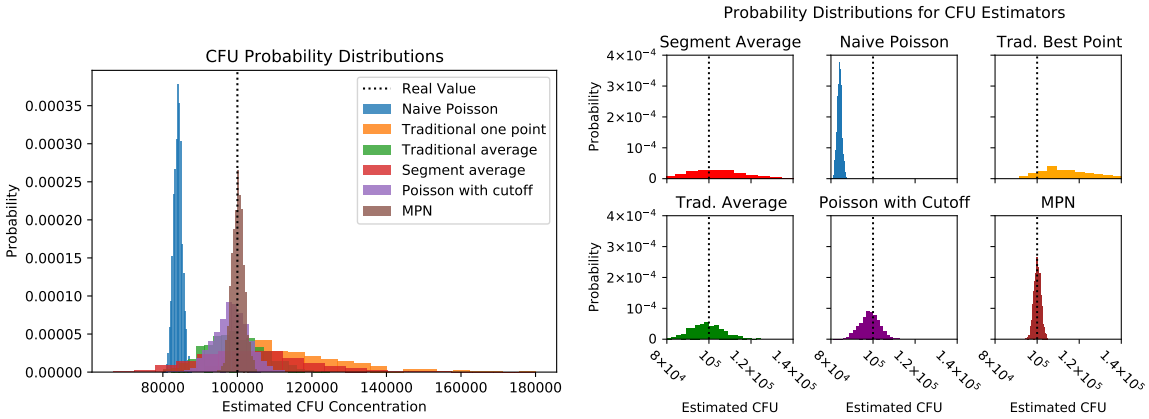

Figure 3.3: The probability distributions of estimated CFU concentrations from different estimators generated from 1000 independent numerical experiments with dilutions 0.1, 0.1, 0.01, 0.01, 0.001, 0.001, $r = 100000$, $V = 0.2$, $N = 5000$. Here the segmented-plate average (one-quarter of the plate is counted), naive Poisson, "pick the best", traditional average, Poisson with cutoff, and MPN methods are compared. The MPN method demonstrates the best combination of high precision and accuracy.

To compare the performance of the different estimators discussed here, we simulated 1000 experiments and applied each of our estimators to the resulting data. Data for each experiment was modeled using the binomial crowding model with $r = 10^5$, $V = 0.2$, $N = 5000$, and dilution values (0.1, 0.1, 0.01, 0.01, 0.001, 0.001). This corresponds to two replicates for each dilution in a tenfold dilution experiment. An example set of colony counts corresponding to these dilutions is (1705, 1629, 196, 181, 21, 21). The first two dilutions are in the over-crowded regime and the last two dilutions are in the dilute uncrowded regime. The traditional methods ("pick-the-best", averaging, segment averaging) and Poisson with a cutoff will discard the first two counts as too many to count, while the other methods will use their numeric values. The resulting distributions are plotted in Figure 3.3.

The results show that the MPN (most probable number) method is unbiased and has the highest degree of accuracy. The Poisson with a cutoff (which always discards counts from the least-diluted samples in these outputs) is nearly unbiased, whereas the naive Poisson (which unrealistically uses all colony counts and included here only for comparison) is biased down due to inclusion of "crowded" data. This illustrates the relative costs of discarding data and using these data inappropriately. The naive Poisson has a similar variance as that of the MPN because both are using all the data points. However, the measure around which the naive Poisson estimator varies is incorrect due to this bias. With the Poisson estimator, increasing accuracy comes at a cost in precision; the Poisson with cutoff has roughly twice the standard error of the MPN method due to the fact that it does not use all the data and throws out the first two counts of each experiment. Next, the traditional averaging method [131] has roughly five times the standard error of the MPN method, due to the fact that it gives lower-precision measurements the same weight as higher-precision large counts in the uncrowded regime. However, it is unbiased. If there are technical replicates, pick-the-best (choosing the largest number of counts in the countable range, over multiple technical replicates at each dilution) is a biased estimator (overestimating CFUs) and has a standard error roughly ten times that of the MPN method. Pick-the-best where the best count from *each* technical replicate is used is equivalent to Poisson with a cutoff, with some loss of precision due to discarding of small counts. Segment averaging (here, counting one-quarter of the plate, and assuming perfect segmenting such that exactly one-quarter of the colonies are counted) resulted in an unbiased estimator with the largest standard error, roughly 13 times the standard error of the MPN method.

These simulations show that the MPN method produces the most precise results and is unbiased. However, the Poisson with a cutoff is a close second, also with high accuracy and precision and with the advantage of being practical to calculate

by hand. The bias of the naive Poisson (using all data) serves as a warning: if counts are not in the uncrowded regime, the Poisson assumptions do not apply, and an estimator using only number of colonies counted at each dilution will under-estimate the CFU density in the original sample. Other standard estimators (averaging, segment averaging) using the same data required for the Poisson estimator show universally poorer precision than Poisson with a cutoff and cannot be recommended.

Estimator Name	Strengths and Weaknesses
Pick the Best	This traditional estimator is simple to understand and calculate but has large standard error.
Naive Poisson	The naive Poisson is valid at low crowding, but if used with high crowding data can produce a strong bias. It can combine data across multiple different dilutions.
Poisson with cutoff	The Poisson with a cutoff is easy to calculate by hand. It can combine data from different dilutions. The resulting bias of the estimator can be controlled by setting the cutoff and is sufficiently small when data is uncrowded.
MPN	The MPN method is valid across all crowding levels and uses all available data. It can combine multiple experiments. The same method can be used for colony counts on plates and in tubes, viewing patches of a plate as equivalent to individual tubes. The method requires either a computer program or table to calculate. It produces an unbiased estimator and has the smallest standard error of all discussed methods.

Table 3.1: Table summarizing the strengths and weaknesses of each estimator along with their appropriate regions of validity.

3.4 Discussion

We have discussed commonly-used point estimator methods for estimating CFUs in a single sample from dilution series data, and we have presented a new method based

on the Most Probable Number (MPN) framework. The methods overview given here, while far from comprehensive [117, 138, 139, 140, 141, 142], is intended as a practical introduction to sampling errors in count-based measurements, particularly for researchers outside environmental and food microbiological surveillance who are likely to have had little if any exposure to the existing literature.

We have focused here on technical rationales for choosing a point estimator for CFU density, but it is important to emphasize that the research question and the data taken must be suitable. We assume here that the researcher wishes to obtain a point estimate of bacterial density in each sample, with high accuracy and precision so that comparisons between samples can be made. The Poisson-based estimator used throughout this paper assumes well-mixed, homogeneous samples with high culturability, which may not be true even for shaken broth cultures. This assumption should be verified for the sample type to be used. Departures from the Poisson will appear as deviations from expected dispersal of counts [116, 121], as indicated in the text. If measurements across technical replicates are not Poisson, this may be correctable. For example, if bacteria are known or suspected to clump, proper shaking [104] and/or use of a surfactant like Tween 80 [143, 144] can help to disperse aggregates. As always, any such protocols should be validated under the conditions where they are to be used.

In practice, the choice of point estimator will depend on the precision required for the estimate of CFU density, as well as the tradeoffs between experimental repetition and analytical complexity that a researcher is willing to make. We have provided a summary of the strengths and weaknesses of all methods in Table 3.1. Traditional pick-the-best estimators are fine for quick imprecise measurements; however, this method has the largest standard error as it does not use a majority of the data collected. Other methods can use more of data collected to to provide more precise point estimates of the concentration with smaller standard error. For experiments

with reasonably large expected effect size, the simplest mathematically admissible method - the Poisson estimator with a cutoff - is perfectly valid, as long as the dilutions are chosen appropriately to ensure all measurements are in the countable range. Broadly speaking, addition of unbiased data will improve the precision of an estimator. Historically, technical replicates have been used for this purpose - even technical duplication is sufficient to markedly reduce variance of the estimated CFU density, although triplicate plating is preferred to safeguard against accidents and outliers [126] . The Poisson model allows data from technical replicates to be combined into a single mathematically interpretable point estimator with definable properties - specifically, a maximum likelihood estimator, which should be an unbiased and minimally variable estimator for the true value. This is as opposed to averaging [131], which produces an estimate whose properties are not well defined. The Poisson method also allows the investigator to incorporate data from dilutions with too few counts, *in addition to* (not in place of) data from countable wells in the same dilution series - by effectively re-weighting the contribution of these wells by the total volume of original suspension that they contain, these data can be used to improve the accuracy of the estimator even though their sampling variance is high. We have presented several methods for estimating CFUs and we have provided a calculator for these estimators available on `Hugging Face` spaces, named `CFUestimator` [128].

The correspondence shown here between using tubes and gridding a plate into subsections based on colony area allows the usage of estimator techniques typically used for quantal-based measurements of CFU density, specifically the MPN, where positive growth events (e. g., colonies) are explicitly considered to represent *one or more* originating cells. These techniques have a long history in environmental surveillance microbiology, and statistically well-founded techniques are readily available for analysis of such data [100, 145, 146]. If an experimentalist wants tighter bounds for an estimated CFU count, the MPN provides a very low-variance, unbiased estimator at

the cost of some extra steps. This estimator allows the experimentalist to incorporate data from normally uncountable (TMTC) plates as well as counts from uncrowded plates, maximizing the amount of information that can be gleaned from a dilution series.

The MPN model requires an estimate of the maximum number of colonies that can be packed into the growth area for each sample; we show that it is better to over-estimate this maximum than to under-estimate it. If the patch size on a plate is correctly chosen to be around the size of a typical colony, even a spot-plating assay on a 10 by 10 cm plate is equivalent to running hundreds of tubes in parallel. Further, it is necessary to estimate the number of occupied regions in the growth area. In or near the uncrowded regime, this will be equivalent to the number of counts. However, this method does not require that all colonies are individually countable - instead, image analysis[147, 148, 149] can be used to estimate both the size of an individual colony and the fraction of total area occupied by colony growth. The MPN estimator can therefore potentially provide accurate, precise estimates of CFU density for plates where exact counts cannot be obtained. However, colony size varies across different microorganisms as well as across culture conditions (media type, agar percentage, pad thickness, plate drying time and conditions, growth temperature and atmosphere, etc.) and incubation time on plates, meaning that the size range of colonies may be different even across plates within a single experiment [150, 151]. This added complication of properly choosing a grid size or determining the typical size of a colony means that application of the MPN will most likely require parameters estimated for the specific experiment being analyzed. Further, the fact that colony size can decrease under crowding means that heavily-crowded plates or plate regions, where few or no distinct colonies are visible, may have very different “average” colony sizes than the same microbes in a less-crowded area. While theory suggests that the MPN estimator will be most precise when the majority of colony-sized locations are

occupied ([152]), this practical limitation suggests that use of the MPN on plate count data will become less accurate with extremes of crowding, and that the best use of the MPN is likely to be in the liminal region between the technically uncrowded and the physically uncountable, where most to all growth is in the form of distinct, countable colonies but crowding produces a measurable bias in these counts.

Chapter 4

Variance in *C. elegans* gut bacterial load suggests complex host-microbe dynamics

This chapter is based on the work done in collaboration with K. Michael Martini, Ilya Nemenman and Nic Vega.

4.1 Summary

Variation in bacterial composition inside a host is a result of complex dynamics of microbial community assembly, but little is known about these dynamics. To deconstruct the factors that contribute to this variation, we used a combination of experimental and modeling approaches. We found that demographic stochasticity and stationary heterogeneity in the host carrying capacity or bacterial growth rate are insufficient to explain quantitatively the variation observed in our empirical data. Instead, we found that the data can be understood if the host-bacteria system can be viewed as stochastically switching between high and low growth rates phenotypes. This suggests the dynamics significantly more complex than logistic growth used in

canonical models of microbiome assembly. We develop mathematical models of this process that can explain various aspects of our data. We highlight the limitations of snapshot data in describing variation in host-associated communities and the importance of using time-series data along with mathematical models to understand microbial dynamics within a host.

4.2 Introduction

Microbiomes are complex, dynamic microbial communities [153, 13, 154, 15], the composition of which is known to vary within and between hosts [155, 156]. Many factors are thought to contribute to this variation, including: genotypic or phenotypic heterogeneity in hosts [157, 158], diversity in host-microbe and microbe-microbe interactions [8, 9] and stochasticity in the colonization process [10, 11].

Gut microbial composition is known to vary across host species, across individuals in a population, and within individuals over time [7, 6, 58]. Canonically, this variation is described in terms of the diversity of bacterial taxa comprising a microbiome. However, increasing evidence suggests that variability in total abundance - particularly within individuals over time - may also be relevant for understanding these systems [6, 94]. To better characterize variation in host-associated microbiome composition, we need to understand how different sources of variation contribute to the distributions observed in data.

The nematode *C. elegans* is a simple model host especially useful to study heterogeneity in microbial community assembly. The commonly used laboratory wild-type strain *C. elegans* N2 Bristol is androdiecious and reproduces primarily by self-fertilization, allowing production of highly homozygous populations under laboratory conditions. The short life cycle of this host facilitates generation of large numbers of age-synchronized adults on time scales convenient for laboratory experiments. This

ability to produce large, highly genetically homogeneous, age-synchronized populations with a shared physical environment and life history makes allows to generate sufficient data to make the worm a mathematically tractable model for studying variation.

This host assembles a characteristic intestinal microbiome from soil bacteria in its native habitat [55, 159]. For the gut colonization process, bacteria need to survive passage through the grinder in the worm's throat during ingestion and then attach themselves to the epithelial layer of the gut to grow inside the worm. The colonization process is stochastic [10], but composition of these communities is shaped by interactions among microbes [8] and between microbes and the host [160, 161], which can be viewed as more deterministic. As in other host-microbiome systems, there is substantial compositional variation in the gut microbiome among individuals. Interestingly, we observe this variation even in populations of isogenic, synchronized hosts colonized from a shared inoculum in a uniform, well-mixed environment [161, 162]. This result motivated us to investigate the drivers of community variation using the *C. elegans* model system.

In this paper, we used a combination of experimental data and mathematical modeling to understand what contributes to observed variation in microbial colonization within populations of hosts. In our previous work [161, 40], where worms were colonized with an eight-member minimal native microbiome, we observed large variation in microbiome community composition and total bacterial load among individual hosts of the same genotype. In the current experiments, we further simplified this system by mono-colonizing synchronized populations of *C. elegans* N2 Bristol with each of the single bacterial isolates from the minimal native gut microbiome. We found that high variation is still present in bacterial load of mono-colonized worms, indicating that microbe-microbe interactions are not required to produce inter-individual differences in microbial colonization of the worm intestine. Using a logistic type

neutral model to parameterize the colonization process for each bacterial isolate, we found that it is hard to explain the observed variation using the demographic noise and parametric differences among hosts. Next, by experimentally manipulating bacterial growth rate in the worms, we found emergence of alternative "phenotypic" states in bacterial load inside worms. The individual worm-bacteria dynamical systems then move between these states, suggesting that canonical models of bacterial growth cannot fully characterize the host-microbe system's dynamics. We find that the distributions observed can be qualitatively recapitulated by two distinct, more complex models, but that snapshot-type (not individual worm time series) data are insufficient to distinguish between these competing models.

4.3 Results

4.3.1 Large variation in total bacterial population size is observed in the host but not *in vitro*

We previously observed substantial variation in total bacterial load across individual worms colonized with a minimal native microbiome (species in the microbiome are listed in Table A.1) [161, 40]. Here we sought to determine the sources of this variation. First, we sought to determine whether colonization with a microbial community is required to produce expected distributions of bacterial load. For this, we colonized wild-type N2 worms with individual bacterial isolates from the minimal native microbiome. Specifically, wild-type N2 worms were mono-colonized in liquid culture according to standard protocols [58], with each bacterial isolate presented at a 10^8 CFU/ml concentration in the culture. Bacterial load in individual worms was quantified at specific time points (3…48 hours) after the start of colonization. For comparison, we also measured bacterial growth *in vitro* outside the host (as OD600) in a standard worm medium (liquid NGM).

While growth *in vitro* showed low variation across replicates, we observed considerable variation in bacterial load between bacterial isolates and across individual hosts colonized with each isolate (Fig. 4.1a). Different bacterial isolates grew to different final densities in both environments, but there was no obvious relationship between maximum density of a given bacteria *in vitro* and in the host. Standard deviations of bacterial load in hosts (colony forming units, CFUs, per host) scaled linearly with the mean in these data, suggesting that most of this variability is not due to demographic noise [163] (Appendix A Fig. A.1). Distributions of log-bacterial load in hosts tended to be long-tailed and left-hand skewed (Fig. 4.1b), typical for microbial load data in *C. elegans* [164].

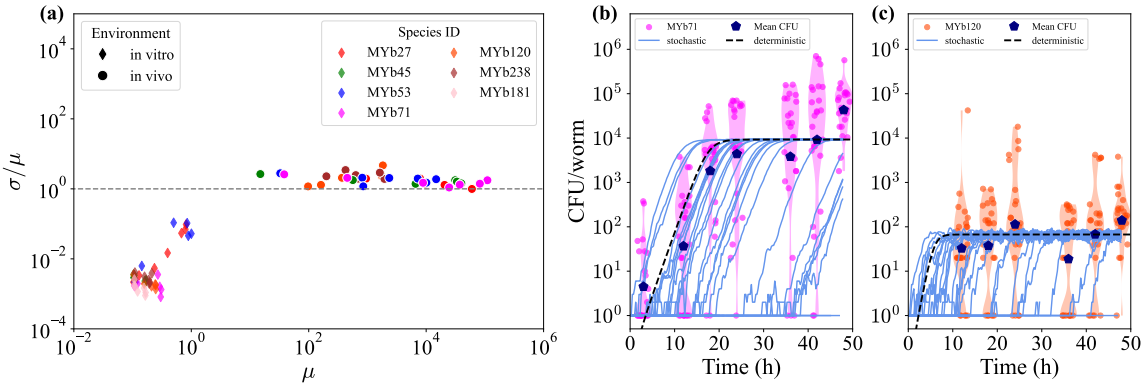

Figure 4.1: ***In vivo* bacterial populations exhibit high variation that is absent in *in vitro* populations.** (a) Seven bacterial isolates from a *C. elegans* native microbiome (Table A.1) were grown *in vitro* in NGM liquid medium at 25°C, measuring OD600 over 48 hours ($n = 6$ replicate wells). For *in vivo*, CFU/worm measurements were taken in individual wild-type N2 worms ($n = 24$) at time points 3…48 h during mono-colonization using the same set of bacteria. Comparison of standard deviation/mean to mean for both *in vitro* and *in vivo* across replicates or worms at different times is shown. (b-c) Bacterial load in samples of individual worms over time since the start of colonization. Experimental data are shown for one good colonizer (b, MYb71, *Ochrobactrum*) and one poor colonizer (c, MYb120, *Chryseobacterium*) to illustrate typical colonization dynamics; other bacterial species' data are shown in Appendix A Fig. A.1. Gillespie simulations (blue lines, $n = 30$) were carried out using parameters obtained from fitting CFU per worm data to the mean field model (Appendix A Table A.2). Mean log-CFU at each time point (large blue point) and the mean-field deterministic simulation (dashed black line) are also shown.

4.3.2 Demographic noise does not explain variation in bacterial load

To check if variation across hosts mono-colonized with a given bacteria could be attributed simply to demographic noise, we established a simple stochastic neutral model as our baseline model for these data. This model contains three rate parameters, which are assumed to be identical across all hosts and are specific to a colonizing bacterial isolate. Colonization (c_i) corresponds to the process of bacteria entering the worm gut from the environment, death (d_i) corresponds to loss of bacteria within the gut, and birth (b_i) corresponds to bacterial multiplication within the host. Total occupancy of the worm gut is limited by a constant carrying capacity (V_i); E corresponds to the number of empty sites in the worm gut (i. e., $E + N_i = V_i$ for each mono-colonized worm). Overall, the model is summarized as:

$$\begin{aligned} E &\xrightarrow{c_i} N_i, \\ N_i + E &\xrightarrow{b_i} 2N_i, \\ N_i &\xrightarrow{d_i} E. \end{aligned} \tag{4.1}$$

The mean-field equation for this model is single species special case of the model described in [40], see Appendix A A.3. It describes the mean population density, $\phi_i(t) = \left\langle \frac{N_i(t)}{V_i} \right\rangle$ as a function of time:

$$\frac{\partial \phi_i(t)}{\partial t} = (1 - \phi_i(t)) \left(b_i \phi_i(t) + c_i\right) - d_i \phi_i(t). \tag{4.2}$$

This model, in which bacteria grow according to a fixed set of parameters and all hosts are identical, provides a convenient null model for bacteria-host dynamics. In this model, the only source of variation is demographic noise due to spontaneous colonization/birth/death events. If this model is sufficient to describe the variation in

bacterial load that is observed within populations of worms, it implies that all worms are essentially identical to each other and share a fixed, time-and density-invariant set of parameters for host-bacteria interactions. Otherwise, one or more of these assumptions is incorrect and must be relaxed to find a sufficient model. To test this, bacteria-specific parameters inferred by fitting the model (see Materials and Methods) to log transformed mono-colonization data (Appendix A Table A.2) were used to initiate stochastic Gillespie simulations [165, 166]. As expected, the model adequately captured the central tendency of the log data but fell short in explaining the observed variance, particularly at later time points, when convergence to saturation density was expected (4.1b-c, Appendix A Fig. A.1). The parameterization of the model is not unique (birth and death partially compensate each other). However, this conclusion does not depend on the specific parameter set used. Thus, demographic noise alone was insufficient to account for differences in bacterial load between individual hosts.

4.3.3 Static host heterogeneity does not explain the variation in bacterial load

One way of explaining the high variation observed in the bacterial load among individual hosts is to allow individual hosts to have different parameters for interactions with bacteria. This assumption has some biological support: there is a well-established "hidden heterogeneity" within synchronized, isogenic populations of *C. elegans*, which can be seen in distributions of aging, mortality, and stress response [167, 168, 169, 170, 171]. We therefore next hypothesized that parameter(s) of the logistic growth for intestinal bacteria might differ across individual hosts.

We first sought to identify a single parameter which, if allowed to be heterogeneous across individual hosts, could explain the observed data. Measurement of rates for ingestion (as a proxy for colonization rate) and excretion of bacteria-sized inert particles indicated variation between individuals, but a single representative mean

rate across individual hosts was sufficient to describe these data, and no reasonable values for these inferred parameters produced multiple orders of magnitude in bacterial load at saturation if plugged into the logistic growth model (Appendix A Fig A.5). Therefore, we focused on the parameters that strongly determine the steady-state bacterial load in the intestine. In this model, these are capacity V_i or per-capita birth-death rates b_i, d_i.

Heterogeneous carrying capacity

We sought to determine if worm hosts significantly differ in their carrying capacity. To gain intuition about this scenario, we considered a model where hosts were allowed to differ only in capacity V. By changing migration rates (c_i) in the intestine, we expect at high migration rate to achieve the final distribution of carrying capacities earlier than when the migration rate is low.

In a scenario where carrying capacity V is the only difference across hosts and all other parameters are the same, average time to first colonist and early (exponential) growth of colonists should be the same regardless of capacity of individual hosts. If colonization rate is increased in this scenario, waiting time to the first colonist during early colonization should decrease, resulting in fewer uncolonized individuals at early time points. The number of uncolonized individuals should decrease over time, also as a function of this rate. Once an individual is successfully colonized above some threshold of stochastic extinction, growth of bacteria in the intestine should proceed until carrying capacity is reached.

Previous work [10] indicated that the density of bacteria provided in liquid media can be used to control the average migration rate into the worm intestine. Thus we mono-colonized worms with one of two isolates (MYb71 or MYb120) across three orders of magnitude in inoculum density to determine the effects of colonization rate on distributions of bacterial load. Colonization over time (CFU per worm) was

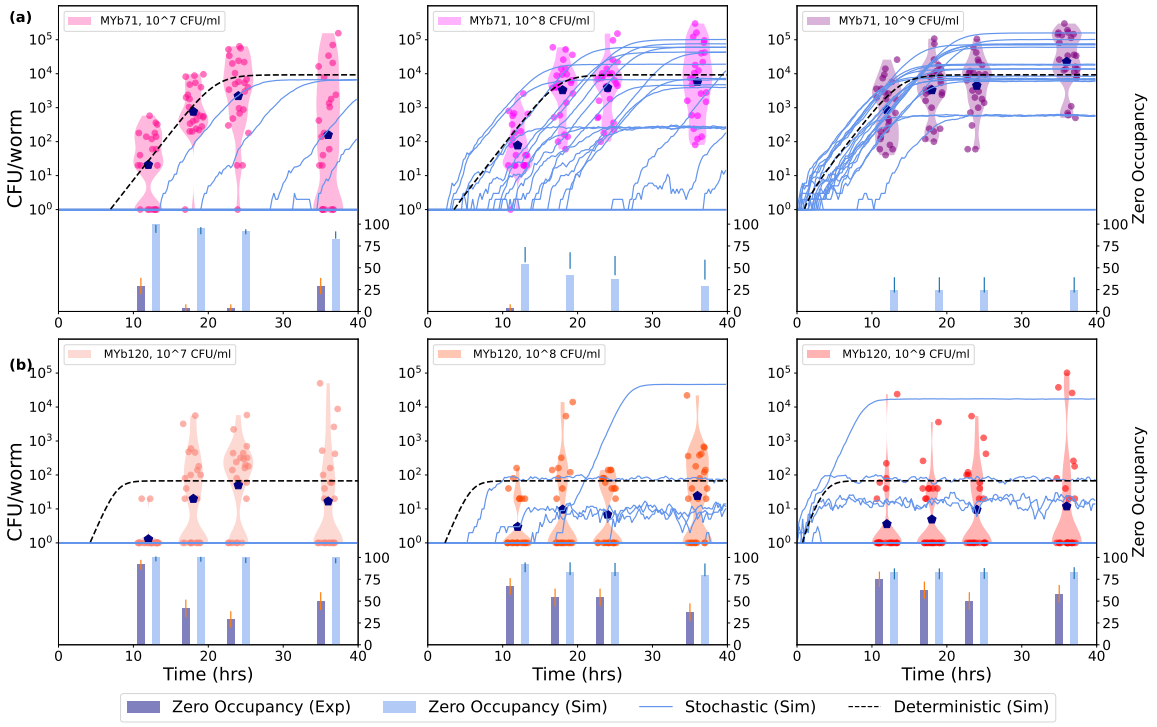

Figure 4.2: **A model with heterogeneous carrying capacity across worms is not sufficient to explain empirical variation in bacterial load.** Bacterial mono-colonization in wild type N2 worms by (a) MYb71 and (b) MYb120 as colonization rate is changed using bacterial densities in the inoculum: 10^7 CFU/ml (left), 10^8 CFU/ml (middle, same as Fig. 1) and 10^9 CFU/ml (right). Gillespie simulations (blue lines, $n = 24$) were carried out using birth and death parameters obtained from fitting single species log-CFU per worm data to the mean field model (Appendix A Table A.2), and distributions of carrying capacity V were established from data at 48 h post inoculation at the highest inoculation condition (far right). Colonization rates corresponding to the 10^8 CFU/ml condition were taken from Appendix A Table A.2 and adjusted down and up by 10 fold in the lowest and highest colonization conditions respectively. Mean log-CFU at each time point (large blue point) and the mean-field deterministic solution (dashed black line) are also shown. Fraction of cases with the zero CFU at all time points is shown in bottom panels for experiments (dark blue bars) and simulations (light blue bars) (See Materials and Methods for fitting and error bar calculations.)

quantified via destructive sampling as previously described.

As shown in Fig. 4.2, bacterial load varied across individual worms at all time points in all conditions. As expected, worms in the lowest-migration condition acquired colonists more slowly than worms in the highest-migration condition, with larger numbers of uncolonized worms at early time points. Distributions of bacterial

load changed minimally between 24 and 36 h time points, suggesting that steady states had been reached.

For the "strong" colonizer MYb71, we expected to observe evidence of logistic bacterial growth within hosts. The data are broadly consistent with this expectation. Increasing colonization rate reduced the number of uncolonized individuals and up-shifted distributions of bacterial load in the earliest time point (12 h), whereas maximum bacterial loads at 24-36 h were similar across colonization conditions, suggesting growth of bacteria to maximum capacity in the most heavily colonized hosts. However, bacterial load in the least-colonized individuals at 36 h was affected by colonization rate, with some individuals remaining below threshold of detection in the lowest-colonization condition.

For the "poor" colonizer MYb120, we expected a migration-forced scenario where bacterial load was determined by the balance between colonization and death in the intestine, such that increasing migration would increase the total load. This is not what we observed. Rather, while worms in the lowest-inoculum condition colonized more slowly, bacterial load was otherwise similar across conditions and time points. Recent work from another group suggests that this may be behavioral; MYb120 is mildly pathogenic, and worms exposed to high densities of a pathogen as a sole food source will stop feeding [172]. The result is that bacterial density in the inoculum has minimal effects on colonization, consistent with our data.

We next compared these results with predictions from a modified stochastic model, where individual hosts were allowed to have different carrying capacity V. Stochastic Gillespie simulations were initiated using the birth and death parameters from previous experiments (Fig. 4.2, Appendix A Table A.2), colonization rate that is scaled to the bacterial density outside the worm ($c/10$ for 10^7, c for 10^8 and $10c$ for 10^9), and carrying capacity randomly picked from 36 h data of the highest bacterial density condition. The predicted trend of the means and first colonization in all the

conditions agree with the observed data. Specifically, at 12 hours post colonization, the centers of the log transformed data move up with increase in colonization rate also agreeing with the deterministic prediction.

To compare simulations to the data, "zero occupancy" percentages (fraction of uncolonized worms) were calculated at each time point in each condition. For MYb71, the Gillespie simulations produced higher frequencies of zero occupancy (uncolonized worms) than observed in experiments under all conditions. For example, in the lowest condition (10^7) of MYb71 at the last timepoint (36 hours), we measured about 25% zeros in experiments, but the simulations predict about 75% zeros. This, in general, remained true for the poor colonizer MYb120: the expected and the observed fractions of uncolonized hosts were similar in the highest-migration condition and across conditions at the earliest time point, but simulations again over-predicted the fraction of uncolonized hosts at all later time points in moderate and low-migration conditions. This suggests that the null model with heterogeneous carrying capacity in a population of hosts is insufficient to capture the variation observed in the experimental data.

Heterogeneity in growth and colonization parameters

In order to try to explain the variation observed in the experimental data, we next considered an extension of the previous model where the birth and death rates of bacteria depend on the individual host. The intuition for this comes from our observation that bacteria loading can vary greatly between different worms and a small change in either birth or migration rate can result in exponential changes in the bacterial load. To test this hypothesis, we conducted Gillespie simulations of bacteria colonization in worms with different birth (b_i) and colonization (c_i) parameters. The birth rate parameters of bacteria for a given worm are drawn from a normal distribution with a given mean birth rate and variance. Similarly, the colonization rate is drawn for

each host from a normal distribution.

We found the best fit set of parameters (including the parameters characterizing the normal distribution of birth rate and colonization rate) that maximize the log-likelihood of data (see Materials and Methods for details). In Fig. 4.3 we observe that this modification of the model appears to be sufficient to explain the observed variation of the data for the strong colonizer MYb71. However, the model is not sufficient to explain the variation and data for the poor colonizer MYb120. Additionally, we expect that if we were to increase the resolution of our log-likelihood calculation, the model fits would become worse for both colonizers.

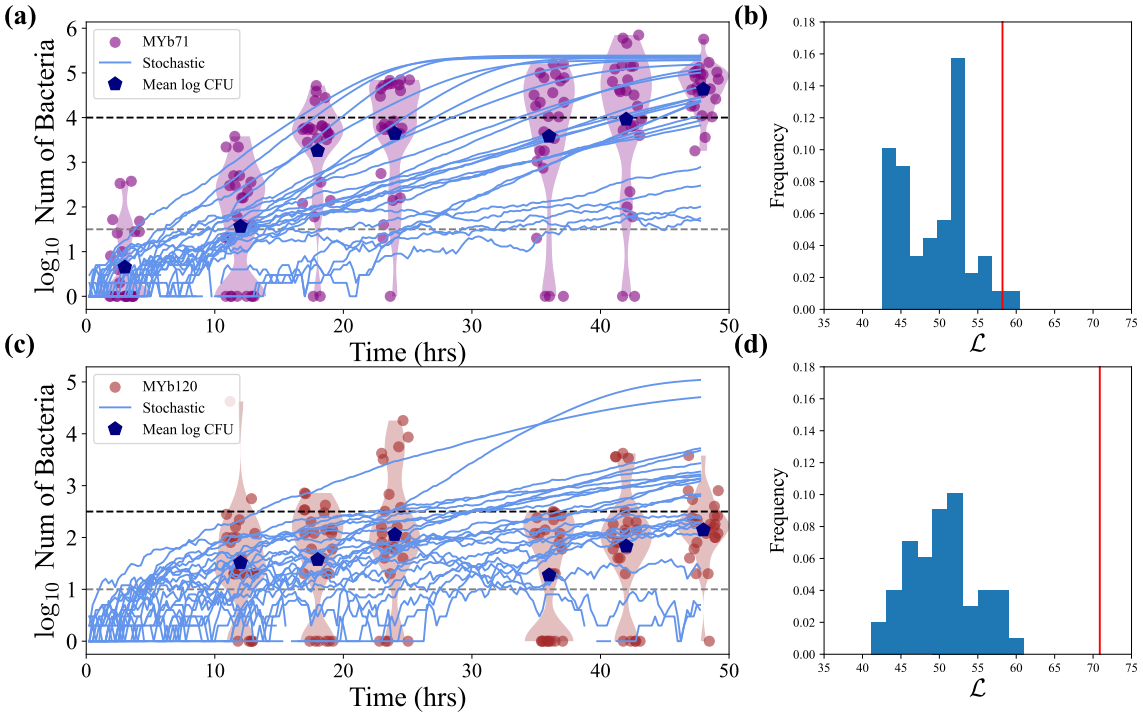

Figure 4.3: **Heterogeneous growth parameters generate large bacterial load variance, but the model is still insufficient.** Gillespie simulations (blue lines, $n = 24$) with heterogeneous growth parameters (colonization and birth rates) for a) MYb71 and c) MYb120 in comparison with the data previously shown in Fig. 4.1. The upper bound of the low bacterial count bin and the lower bound of the high bin, which were used to determine the best fit parameters, are shown in dotted lines (see Materials and Methods). Distribution of the negative log-likelihoods ($\mathcal{L}$) of the simulations ($n = 50$ with 24 simulations each) using the best parameters for the model for b) MYb71 and d) MYb120. Negative log-likelihood of the experiment (red line) given the best parameters is also shown.

Heterogeneity in growth and death parameters under growth inhibition

In our earlier experiments, total bacterial load consistently varied over orders of magnitude between individual hosts within synchronized, isogenic populations when colonized with single bacterial taxa under shared conditions. However, the results thus far did not indicate that individual worms had different total capacity for bacterial colonization. Nor did we find evidence that individual worms had different parameters for colonization or excretion rates (see Appendix A Fig. A.5). It was, therefore, reasonable to ask whether differences in net bacterial growth (birth-death) could explain differences in bacterial load among hosts. To clarify this, we next sought to isolate these within-host processes after an initial intestinal population was established.

As the host presents a responsive, biotic environment capable of controlling bacterial load, we hypothesized that different hosts might be differently able to exercise this control, and that this might correspond to differences in bacterial death rate in the intestine. Therefore, we modified our null model to allow bacteria-specific death rates inside the host to be heterogeneous across individual hosts. For simplicity, growth rates and carrying capacities in this model were bacteria-specific and constant across hosts within a population. In the absence of migration ($c_i = 0$) and at steady-state ($\frac{\partial \phi}{\partial t} = 0$, we can solve Eq. (4.2) to get an effective steady state value of N_i^*. In this model, high-load worms have bacterial birth rates much higher than death rates, resulting in an effective steady-state capacity for bacteria of species i close to the true capacity V_i. If $b_i > d_i$, this capacity is:

$$N_i^* = V_i \frac{b_i - d_i}{b_i} = V_i \left(1 - \frac{d_i}{b_i}\right). \tag{4.3}$$

From this model, some simple, qualitative predictions are possible for the effective steady state value N_i^*. If growth in the intestine b_i were decreased while d_i remained unchanged, effective steady state capacity should decrease.

To test this model, we used a bacteriostatic antibiotic to decrease growth of bacteria inside pre-colonized hosts. For these experiments, N2 adults were pre-colonized with fluorescently labeled *Ochrobactrum* MYb14, a member of the native worm microbiome closely related to the "strong" colonizer MYb71. Like its relative, MYb14 is a well-tolerated commensal and colonizes to high densities in the worm intestine. After pre-colonization, worms were exposed to a gradient of the static antibiotic chloramphenicol, including low drug concentrations sufficient to impair growth of MYb14 in the supernatant but not inside the host. Heat-killed OP50 was used as an inert food source during antibiotic treatment. Pre-colonized worms were divided across antibiotic treatments at random, so that all treatment groups represented draws from the original population of worms. Worms were measured, washed, and re-fed with fresh inert food and antibiotic every 24 h. Confirming the utility of fluorescence as a proxy for bacterial load, the relationship between bacterial load and fluorescence in individual worms was monotonic (Appendix A Fig. A.8). Notably, this colonist showed a threshold of detection of roughly 100 CFU per worm, and fluorescence saturated at high bacterial densities (above 10^6 CFU per worm), indicating a "ceiling" effect for highly colonized worms (Appendix A Fig A.8). The auto-fluorescence of *C. elegans* limits the ability to detect low bacterial loads inside the worm guts. Worms below the auto-fluorescence line in Fig. 4.4 are not necessarily uncolonized worms as can be seen in Appendix A Fig. A.8. This resulted in a nonlinear mapping between the fluorescence signal and the CFU measurements, which needed to be addressed in the models below.

The lowest concentrations of drug used here (25 and 100 μg/mL chloramphenicol) are sufficient to inhibit bacterial growth outside the host, preventing new colonization, but do not inhibit growth within the host. This is expected, as antibiotic concentrations required to inhibit growth in the *C. elegans* intestine are typically 5-10X higher than the *in vitro* MIC [173]. Accordingly, in both of these conditions we observed

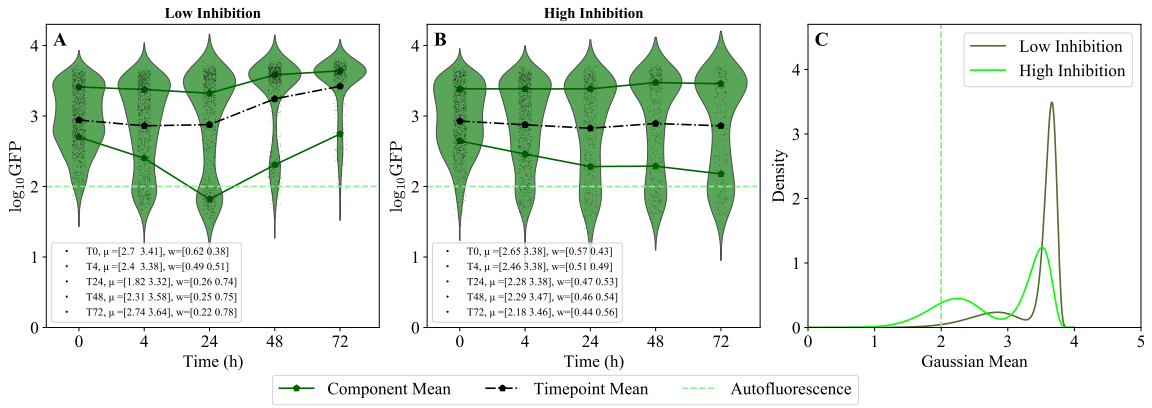

Figure 4.4: **Distributions of bacterial load under low vs. high inhibition of growth within hosts.** Green fluorescence in MYb14-GFP-KmR pre-colonized worms over 72 hours of inhibition at (a) low (25μg/ml) or (b) high (500μg/ml) concentrations of chloramphenicol. Centers and weights of high and low GFP modes at each time point from the transformed Gaussian mixture model fits are shown in the legend. Mean GFP (black dots, dashed lines) for the entire population at each time point is shown. Mean autofluorescence (light green, dashed lines) calculated using the data from uncolonized worms is also shown. CFU to GFP mapping is shown in Appendix A Fig A.8. (c) Probability density fits modeled as a Gaussian mixture with two components fit on CFU transformed data and then transformed back to GFP, at T72 for low and high inhibition (See Appendix A A.7.1).

substantial growth of bacteria in the worm gut over 72 h; this was visible in total bacteria-associated fluorescence per host and in direct measurements of bacterial load (Fig. 4.4, Appendix A Fig. A.6). At higher concentrations (250-500 μg/mL antibiotic), growth of bacteria within the host was partially inhibited, as can most easily be seen by comparing bacterial load after 72 hours on antibiotic (Fig. 4.4, Appendix A Fig. A.6). Maximum intestinal populations increased over time overall even at the highest concentration of drug, indicating that growth was not reduced to 0 (Fig. 4.4 , Appendix A Fig. A.6). This was observed in bacterial load taken from a sub-sample of worms as well as in GFP fluorescence, again indicating the utility of bacterial fluorescence as a proxy for bacterial populations in the host (Appendix A Fig. A.8).

However, differences between treatments indicated substantial growth suppression at the highest levels of drug — at 72 hours, median CFU/worm was 5.5 logs at low drug vs 3.8-4 logs at high drug (Appendix A Fig. A.8). Under partial inhibition

of growth within the host (high drug), by the final time point, we observed fewer worms at a very highly colonized state (5.5-6 log CFU/worm) and a larger fraction of individuals in the low colonization state (∼3.5 log) as compared to populations where only migration into the host was suppressed (low drug).

In the $c_i = 0$ regime, where migration is absent, the effective steady state is specifically given by Eq. (4.3). From the heterogeneous models presented thus far, we expected to see steady state values near the carrying capacity, as $d \ll b$ for this bacterial colonist. When bacterial growth is reduced by antibiotic treatment, we would expect that the steady state bacterial load would be reduced accordingly. However, we do not observe this (Fig. 4.4). This could be due to the fact that the death rate is much smaller than the birth rate which would result in $N_i = V_i$ and we cannot observe the small downward shift due to biological variance masking this shift.

Further, these data indicated multiple modes of bacterial density within populations of hosts. For example, in the high drug condition at 72 hours, the weights of the sub population of worms are comparable. While we know that the GMM analysis (see Materials and Methods) can be tricky, there are clear signatures of multiple subpopulations. Furthermore, changes in population weight (fraction of worms in each of the modes) across modes of the GFP fluorescence data cannot be explained by sampling effects. The entire population of worms is measured at each time point, and all of the same worms (minus losses to handling) are present across time points. One possible hypothesis is that there could be two sub-populations of worms, where intrinsic birthrate $(b - d)$ is either high or low. If this were true, we would expect to see bacterial load in the "high" sub-population to stay high over time, and vice versa for worms in the "low" sub-population. However in Fig. 4.4A, we also observed that the "low" subpopulation at 24 hours does not continue to stay low. Although it is not possible to determine trajectories of individual worms from these data, it is

difficult to explain the observed redistribution of population weights across the modes without some corresponding transitioning of individual worms between them.

subsectionData suggest multiple worm subpopulations, with individuals transitioning between them on scales of hours We, therefore, next sought to isolate worms that differed in initial bacterial load, to determine whether the redistribution of individuals seen in Fig. 4.4 across states implied by these data was actually occurring.

From the logistic model, we expected that if net growth of bacteria in the host was different in high- and low-bacterial load worms, these groups would respond differently when an initially high rate of colonization was reduced to 0 after establishment of a bacterial population. High-load worms, where presumably initial birth is much larger than death during early colonization, should be well out of the migration-forced regime (where bacterial load is heavily dependent on migration) and should be minimally responsive to any change in colonization after the initial population is acquired. Low-load worms, where presumably these rates are more similar, may drop slightly in bacterial load or even decrease toward extinction (if death is larger than birth, such that bacterial load in these worms is entirely dependent on migration). Removing colonization should, therefore, increase separation between modes, with high-load individuals remaining highly colonized and low-load individuals settling at a level determined by the relative contributions of death and migration.

To establish initial populations, N2 adults were pre-colonized for 24 h on fluorescently labeled *Ochrobactrum* MYb14. After pre-colonization, worms were sorted into "high" and "low" GFP bins based on total fluorescence, with a narrow gap between bins to minimize overlap in bacterial load. (Note that these broad bins were expected to have considerable internal variation, from the machine or across experiments.) Worms were then split evenly between treatments, with half of the worms from each bin returning to the original condition (10^8 CFU/mL live MYb14-GFP provided in the media, denoted below as "Migration"), and half moving to a condition where

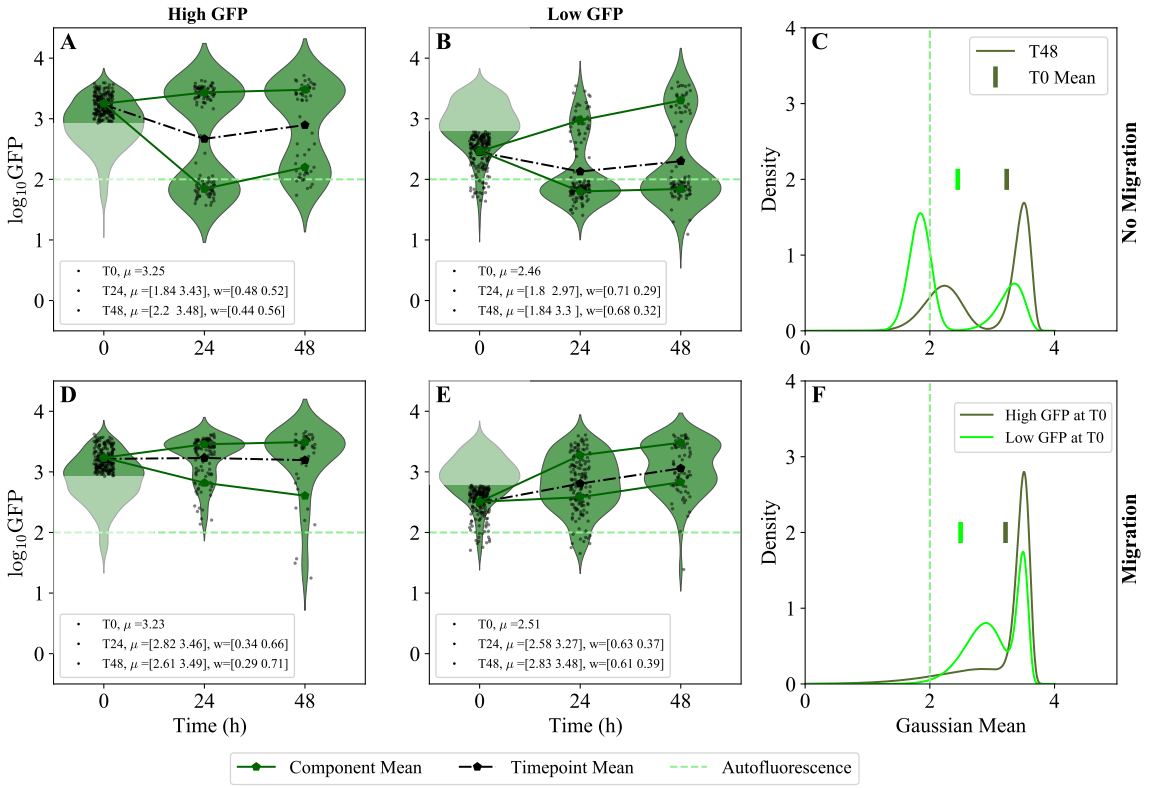

Figure 4.5: **Worm switch between high and low colonization states** Green fluorescence over 48 hours after MYb14-GFP-KmR pre-colonized worms were separated based on high (a,d) and low (b,e) GFP under conditions of a-c) No Migration (top) or e-f) Migration (bottom). Full T0 distribution (pale green) in fluorescence is shown in the background. Mean GFP (black dots, dash-dotted lines) for the entire population at each timepoint is shown. Mean auto-fluorescence (Light green, dashed lines) calculated using the data from uncolonized worms is also shown. c,f) PDFs using the transformed GMM fits at T48 for worms starting at low (light green) and high (dark green) fluorescence in no migration (top) and migration (bottom) conditions (Appendix A, Transformation of GFP measurements to estimates for bacterial load in individual worms)

new colonization is prevented (heat-killed OP50 for inert food + chloramphenicol to prevent cross-inoculation among hosts, denoted below "No Migration"). Populations were measured at 24 and 48 h, so that each data set represents repeated measurement of the same population of individuals (minus individuals lost during handling).

We observed that individuals could transition out of their original bins, moving from "high" to "low" and vice versa. For example, in the absence of continuous colonization (no migration), worms starting from the "high" condition produce a "low"

mode (Fig. 4.5A) and vice versa (B). Allowing continuous colonization (migration) (Fig. 4.5D-E) changed the distribution of individuals but did not prevent moving between bins. This can be seen in distributions of GFP fluorescence (Fig. 4.5, right most column) as well as in CFU/worm measurements from destructive sampling (Appendix A Fig. A.8). Similar to before, worms below the auto-fluorescence line could have low bacterial loads instead of true zeros. We observed a similar pattern in N2 hosts colonized with a different bacteria, the pathogen *Salmonella enterica LT2* (Appendix A A.14). Existence of two host subpopulations and individuals transitioning between them on scales of just a few hours is not consistent with the simple logistic model or with any host-sub-population model considered thus far. Instead, this indicates the need for a model capable of producing alternate states within individual hosts.

4.3.4 Modeling multiple states in the worm-bacteria system

There are several possible ways to achieve multi-stable populations of bacteria within the guts of *C. elegans*. Here we will examine two of them. The first model considers a system where multistability arises due to density-dependent population dynamics within the host, such that each stable population of bacteria has a basin of attraction characterized by a specific mean value. We can model this kind of multi-stability using multiwell-potential models from classical mechanics, where the potential ($U(\phi)$) contains multiple troughs corresponding to stable states in the population of the bacteria. Transitions between these states are driven by random white noise η, with zero mean $\langle\eta\rangle = 0$, and variance $\langle\eta(t)\eta(t')\rangle = D\delta(t,t')$. This model has the following expression:

$$\frac{\partial\phi}{\partial t} = f(\phi) + \eta = -\frac{\partial U(\phi)}{\partial\phi} + \eta \tag{4.4}$$

where $f(\phi)$ has roots at the fixed points, or alternately, the potential $U(\phi)$ has troughs (stable fixed points) and peaks (unstable fixed points).

We chose to fit the multiwell-potential model to the modes of the 24-hour time point in the low-inhibition data set in Fig. 4.4. This time point is 72 hours after the *C. elegans* were initially colonized and is, therefore, on the same day of adulthood as the 48 hour time point of the no migration condition of figure 4.5. This will allow us to avoid fitting transient behavior and to simulate and compare to the no migration condition of Fig. 4.5 (see Appendix A).

Log(GFP) (denoted as ϕ') is a nonlinear monotonic function of the underlying bacterial population size inside the gut of *C. elegans*. It also depends on properties of the measuring device. This poses a challenge for modeling as the transformation between the fluorescence and the bacterial load is not obvious. To build a more reliable model, we transform the log(GFP) measurements to the log(CFU), denoted as ϕ) a more accurate measurement of the bacterial load, using a nonlinear transformation inferred in Appendix A Transformation of GFP measurements to estimates for bacterial load in individual worms.

The transformed data shows two large modes in the log(CFU) bacterial load ϕ, which correspond to two troughs in the potential (Fig. 4.6A). To have the two modes, the potential $U(\phi)$ must be at least 4th order or higher; or equivalently, that $f(\phi)$ must be 3rd order or higher. However, the fits of the potential using a procedure outlined in the Appendix A showed that, while the 4th order potential is able to capture the means of the two modes of the bacterial load distribution, it struggles to capture the widths of the two main peaks Appendix A Fig A.11). In contrast, the 6th order potential (equivalently, 5th order f, can do both. A plot of the simulation of the 6th order potential model is compared to data in Fig 4.6B. Crucially, even though the fits are done only using the snapshot data, the model also produces the dynamics of switching that are qualitatively similar (but not identical) to those seen in the experiments. In particular, using parameters determined from the 24 hour mark of Fig. 4.4 to predict the no migration condition of Fig. 4.5 we see in Appendix

A Fig. A.12 that the locations of the two main peaks are well predicted but the bacterial loads are not. Qualitatively the relaxation to the stationary distribution is similar between experiment and simulation. For example, when initialized in the high peak, some of the bacterial load transitions to the low peak with time.

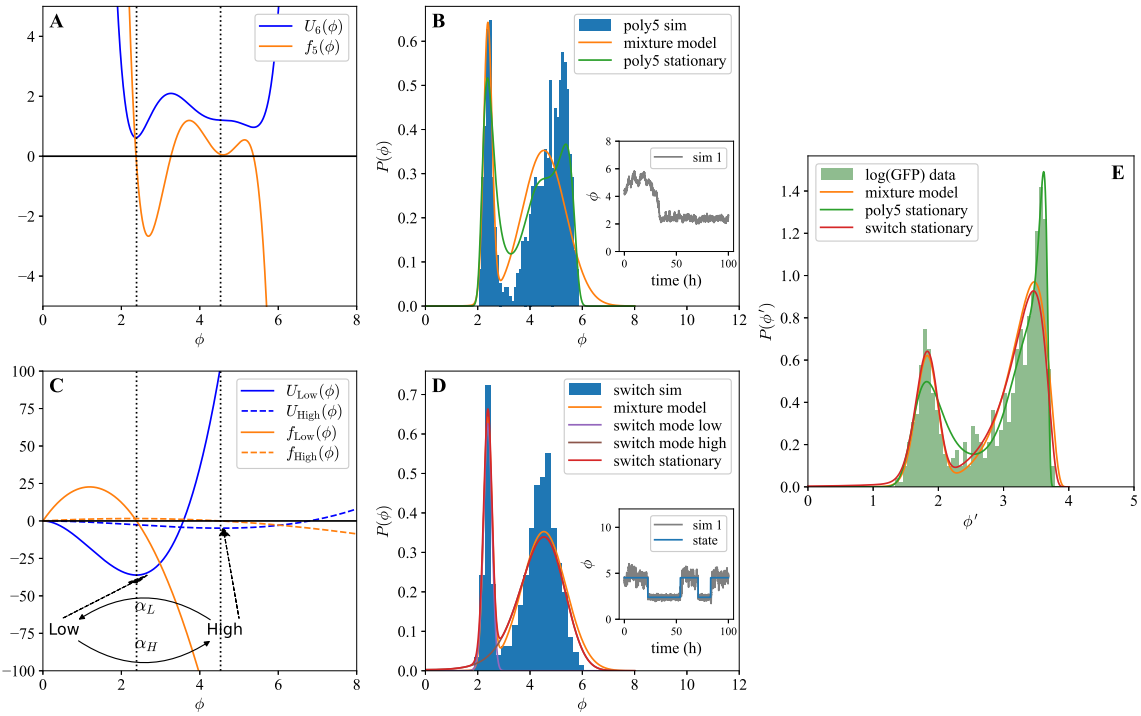

Figure 4.6: **Multi-stable population models** A) Potential $U(\phi)$ and $f(\phi)$ for potential model fit to 24h low inhibition data from Fig. 4.4. B) Probability distribution from 1000 simulations of the potential model, as well as the model's stationary state. Label poly5 corresponds to the fifth order force f_5 in panel (A). We also show the Gaussian mixture mdoel fit for comparison. Inset shows one sample simulation. C) Schematics of the state switching model switching between Low and High states and the corresponding logistic growth functions f for worms in the low (f_{low}) and the high (f_{high}) state and their corresponding potentials, U_{low} and U_{high}. D) Probability distribution from 1000 simulations of the switching model as well as the model's low and high state distribution and the distribution in the stationary state. We also show the Gaussian mixture model fit for comparison. Inset shows a sample simulation and its corresponding state (high or low). E) Probability distribution of log(GFP) (ϕ') data and best fit theory curves (all transformed to the log(GFP) state) for the Gaussian mixture model, the sixth order potential model, and the state switching model.

The second type of model is one where each *C. elegans*-microbiome system switches between states. We consider a model with two states, corresponding to "high" and

"low" bacterial loads. We denote the state variable as s, and it can take two values $\{s_{\text{low}}, s_{\text{high}}\}$. The system randomly switches between the states with α_H being the rate of low-to-high transition, and α_L the rate of the high-to-low one (Fig. 4.6C). In each state, the bacteria grow logistically within the host intestine according to state-dependent parameters (Fig. 4.6C).

$$\frac{\partial \phi}{\partial t} = r_s \phi (C_s - \phi) + \eta(s) \tag{4.5}$$

where $\langle \eta \rangle = 0$, $\langle \eta(t)\eta(t') \rangle = D_s \delta(t, t')$.

For comparison to the first model, the carrying capacity in the high state (C_{High}) corresponds to the highest root of f and the carrying capacity of the low state C_{low} corresponds to the lowest root of f. The rates of transition between states can be independent of the potential function describing each state. The state switching model results in a probability distribution very close to that of a Gaussian mixture model (Fig. 4.6D), making it straightforward to fit based on the estimated parameter of the GMM. Additionally, we are able to directly measure the switching rates between states and find the transition from low to high to be $\alpha_h = 0.08$ (1/h), and from high to low to be $\alpha_l = 0.02$ (1/h) (see Appendix A).

A comparison of the Gaussian mixture model, the potential model, and the switching model is shown in Fig. 4.6E. All the models were fit in log(CFU) space and then transformed back to the log(GFP) space for direct comparison to experiment. The Gaussian mixture model and the switching model are functionally identical in terms of their ability to fit the data. This is because each peak can be fit independent of the other. Both of these models struggle, however, to fit the right most part of the observed distribution. The potential model is better capable of fitting the right most part of the distribution of bacterial loads, but at low order it struggles to quickly transition between peaks. Clearly, as the order of the potential model is increased it

becomes better able to fit the empirical bacterial load distribution.

While the two models are very similar, they do make some distinct predictions. Thus, in principle, experimental data can be used to detect which of the models is a better representation of the reality. However, in practice, the data we have is not statistically powerful enough for this purpose. For example, the independence of state transition rates and local fluctuations is one of the key predictions of the state switching model compared to the high-order potential model, where these features are dependent. However, to detect if the local fluctuations and the state transitions are independent or not with high accuracy requires single-host time series with sufficient temporal resolution to measure both features. For our population-wide "snapshot" data, these models are functionally equivalent as long as the potential is of high enough order. Indeed, we can see this from simulations of how these models behave when initialized as in Fig. 4.5: both display qualitatively similar features as they approach their long time-steady state behavior (see Appendix A Fig. A.12 and A.13).

4.4 Discussion

In this work, we show that there exists innate heterogeneity in colonization density within a population of individual hosts, with total bacterial load consistently varying over more than an order of magnitude between individuals. This heterogeneity was not apparent in *in vitro* bacterial populations, consistent with the expectation that bacteria grow *in vitro* in a approximately logistic manner and that cultures inoculated simultaneously from a single parent culture should exhibit low variation [174, 42]. This observation suggested an important role for the host, but the data were not well described by simple models of host colonization. First, using Gillespie simulations assuming all the parameters involved in colonization are the same for all worms, we show that the demographic noise is insufficient to explain the variation we observe

in our experimental data. Alternate models of the same form but with a stationary worm-to-worm heterogeneity in various population dynamics parameters were also insufficient to explain the data. Further, when new colonization was stopped after establishment of the intestinal population, the data indicated two distinct modes in the distribution of bacterial load across worms, with apparent transitioning of individual worms between these modes.

We concluded that a simple logistic type model was not sufficient to explain the population dynamics in the microbiome in the worm-microbe system, and that a suitable minimal model must allow multiple stable states even during mono-colonization of the host. Here we explored two such models: a state-switching model where the parameters of logistic growth are determined by a state variable, and a multiwell-potential model, where bacterial growth within the host is a higher order polynomial function of bacterial density. We show that both of these models are capable of reproducing the salient features of the bimodal distribution of the colonization data at different timepoints. Furthermore, while the models are distinguishable in pricniple, we cannot distinguish between them in practice with the data available from our experiments. Such disambiguation would require time series of bacterial load in individual worms, rather than dynamics of the distributions of the load over the worms, which we collect. These data can be collected using fluorescence microscopy with labeled bacterial strains [175, 176, 177]. A sufficiently granular time series should show whether changes in bacterial load behave more as expected for dynamical state transitions (movement between steady states on a more or less fixed landscape) or for an underlying system-level state switch (such that one primary state is available for each host-microbiome system at a given time, and the available state(s) change depending on some hidden process).

The drivers of bacterial load variation and "switching" in this system remain to be determined. In these experiments, we used isogenic, age-synchronized popula-

tions of hosts with a shared life history; genetic and developmental variation between individual hosts is minimal. While it is well known that worms within isogenic, synchronized populations are physiologically heterogeneous [171, 167, 170, 169], we found that "hidden" host-side heterogeneity was not sufficient to explain these data. The range of bacterial loads per individual host [162, 161] and the kinetics of bacterial accumulation over time (Fig. 4.1, Appendix A Fig. A.1) vary across different colonizing bacteria, and for a given bacteria or community across worm genotypes, but these properties are generally consistent within a combination of host genotype and microbial colonist(s). This suggests that variation in the host-microbe system cannot be explained by variation in its constituent parts (worm alone or microbe alone). The more complicated, multistate models considered here are best interpreted as representing different forms of feedback within the system, where the available states in bacterial load are some function of the bacterial load (possibly as interpreted by the host immune response, by changes in intestinal function, etc.) or manifestations of an underlying system state (in the simplest case, from a history-independent process such as a stochastic toggle switch). As the host appears to play a crucial role in controlling bacterial populations, and probably in transitions between states, it is plausible that an examination of host transcriptional and/or translational responses within different states would shed some light on plausible mechanisms of the observed multi-modal bacterial populations. This is a goal for future work.

Chapter 5

Summary

This dissertation covers the experimental and mathematical approaches I applied to understand complex dynamics of microbial interactions with the host, *Caenorhabditis elegans*. My research focuses on quantifying bacterial load in individual worms, developing new tools for estimating colony forming units (CFUs), and understanding the variability and dynamics in gut bacterial composition across isogenic worm populations. By using mono-colonization techniques and integrating experimental data with quantitative modeling, I uncovered the role of host background in microbiome dynamics and emphasize that host-microbe as a unit is an integral part of those dynamics. Additionally, I also highlight the importance of acquiring high temporal resolution in data coupled with higher order modeling approaches to fully understand microbiome dynamics. This chapter is a summary of these studies and some final thoughts for future work.

In Chapter 2, I described a 96-well disruption protocol for quantifying bacterial load in *C. elegans* , which enhances throughput compared to existing methods. The surface bleaching method used in this protocol minimizes cuticle-associated bacteria and allows isolation of gut communities. These findings underscore the heterogeneity in bacterial abundance within worm guts, highlighting the limitations of batch-based

measurements and the advantages of quantification of bacterial load at a single-worm level.

In Chapter 3, I presented an overview of various estimation methods for colony forming units (CFUs) within homogeneous samples. This study also introduces a method based on the Most Probable Number (MPN) approach, while addressing crowding and sampling fluctuations. This approach brings attention to selection of appropriate estimation methods tailored to specific experimental conditions that aids in precise quantification of bacterial abundance.

Based on these two studies, I shifted my focus to understanding where the heterogeneity in bacterial load in *C. elegans* comes from using methods discussed in Chapter 2. In Chapter 4, I showed that experimental data revealed significant variability in bacterial loads among individual worms. Upon exploring whether random colonization events could explain this variance, it became clear that stochastic population dynamics processes alone could not account for the wide range of variation observed. Later experiments, in which I manipulated the colonization parameters, showed signs of multistability in bacterial loads. This dynamic stable state in the worm-microbe system cannot be replicated using conventional logistic growth models. Furthermore, I concluded this study advocating for more sophisticated, higher-order models that are able to accommodate multiple stable states or density-dependent growth dynamics to accurately explain observed variance in gut bacterial load. To fully specify such models, snapshot data that we collect is not enough. While the data used in this work emphasizes the importance of host-bacteria association, it is limited in understanding the full picture of the host microbiome dynamics. In this regard, future directions of host-associated microbiome studies should be towards acquiring auto-correlated, high temporal resolution in data.

This dissertation is combination of hands-on experimental techniques, data collection and estimation methods, and quantitative model approaches that have helped un-

derstanding microbial interactions within *C. elegans*. Together, these studies deepen our understanding of how microbes interact with a host and highlight the complexity of host-microbe dynamics. This work emphasizes the dynamic and multistate nature of microbial communities within host organisms which will shape future research on host-microbe systems.

However, several questions remain to be answered: What are the underlying mechanisms that lead to multistability in bacterial loads? How do gut bacterial communities change over time within individual worms? What specific host factors influence the variability in bacterial load? Addressing these questions will require future research to focus on acquiring high temporal resolution data and advanced modeling to further unravel the complexities of host-microbiome dynamics.

Appendix A

Chapter 3 Supplemental Information

A.1 Materials and Methods

A.1.1 Bacterial Strains

Bacterial strains shown in Table A.1 were inoculated from glycerol stocks and individually grown for 48 hours in 1ml LB cultures at 25°C with shaking at 300 rpm. All bacterial strains are from the MYb collection of native *C. elegans* gut isolates maintained by the Schulenburg lab [55]. Strain MYb56 (*Bacillus*) from the minimal native microbiome used in [161] was excluded from these experiments due to its spreading colony morphology on solid agar, which limited the precision of counts. The fluorescent strain MYb14-KmR-GFP, bearing the broad host range plasmid pBTK519-KmR-GFP, was used for measurement of bacterial load via green fluorescence [178].

A.1.2 Worm Maintenance

Worm strains N2 and *exp-1(sa6)* II were obtained from *Caenorhabditis* Genetic Center, which is funded by NIH Office of Research Infrastructure Programs (P40 OD010440).

Strain ID	**Bacterial species**
MYb14	*Ochrobactrum* sp. strain BS30
MYb27	*Arthrobacter aurescens*
MYb45	*Microbacterium oxydans*
MYb53	*Rhodococcus erythropolis* PR4
MYb71	*Ochrobactrum pecoris*
MYb120	*Chryseobacterium* sp. strain CHNTR56
MYb181	*Sphingobacterium faecium*
MYb238	*Stenotrophomonas* sp.

Table A.1: **Bacterial strains used in our experiments.**

Standard protocols were used to maintain and cultivate worms for experiments [79]. Briefly, worms were maintained at 25°C on NGM plates with OP50 and synchronized using Bleach/NaOH protocols. Eggs were kept in M9 worm buffer overnight at 25°C with shaking at 200 RPM to hatch. L1 worms were then washed thoroughly in M9 buffer containing 0.1% Triton-X (henceforth M9TX01) and moved to NGM plates with *E. coli pos-1* RNA interference (RNAi) to produce reproductively sterile adults. After 60-72 hours at 25°C, reproductively sterile adult worms were moved to liquid S medium with 2X heat-killed OP50 (HKOP50), 200μg/ml gentamycin, and 100μg/ml chloramphenicol for 48 hours (25°C with shaking at 200 RPM) to remove any live bacteria that may have accumulated in the gut during growth. Germ-free adults were then used for bacterial colonization experiments.

A.1.3 Single Species Colonization

Bacteria were grown individually to prepare inocula for mono-colonization of worms. Cultures were diluted to 10^8 CFU/ml by suspension in S medium + 1% AXN (axenic medium), centrifuging them for 2 minutes at 10000 rpm and resuspension in the same medium.

Germ-free adult worms were sucrose washed prior to bacterial colonization to remove heat-killed bacteria, dead worms, and other debris. After sucrose wash, 100

worms per colonizing bacterium and time point were sorted into individual wells of a 96-well plate using a large object sorter (BioSorter, Union Biometrica). Each set of worms was washed 2-3 times with 1ml M9TX01, then suspended in 100 μl S medium + 1% AXN and 100 μl 10^8 CFU/ml of individually-grown bacteria from Table A.1. At indicated time points (3, 12, 18, 24, 36, 42, 48 hours), worms were removed from wells and washed to remove the bulk of external bacteria, halting colonization. Pre-colonized worms were incubated in S medium + 2X HKOP50 for 30-60 minutes to purge non-adhered bacteria, then rinsed 2X with 1 mL M9TX01 to remove OP50 biomass.

A.1.4 Single Worm Digests

Single-worm digests were carried out according to standard protocols for this laboratory [58]. Briefly, after purging on HKOP50, pre-colonized worms were chilled to halt peristalsis and lightly surface bleached (1:2000 v/v) in cold M9 worm buffer on ice for 20 minutes to kill any remaining external bacteria. Worms were then rinsed 3X in cold M9TX01 to remove bleach and sorted individually into wells of an Axygen 96-well plate pre-filled with a small quantity of silicon carbide grit and 198 μl M9TX01 for mechanical disruption. Plates were chilled for one hour at 4°C, then sealed with a layer of parafilm and an Axygen square-well sealing lid to create a water-tight seal on individual wells. Plates were then shaken on a TissueLyser II to mechanically break up worm tissues (90 seconds at 30 hz; rotate plates 180°; 60 seconds at 30 hz). After mechanical disruption, released gut contents were serially diluted in 1X PBS and plated onto salt-free nutrient agar (per L: 3g yeast extract, 5g tryptone, 15g agar), on which different bacterial colony morphologies can be easily distinguished . After 48 hours at 25°C, colony counts were recorded.

A.1.5 Biosorter - Green Fluorescence Experiments

Inhibition

Worms were pre-colonized on 10^9 CFU/ml of MYb14-GFP-KmR for 48 hours as in Single Species Colonization. Upon sorting, worms were suspended in S medium + 2X heat-killed OP50 along with varying concentrations of chloramphenicol (25-500 μg/ml). At selected time points (6, 24, 48, and 72 hours), green fluorescence was recorded across all conditions. At selected time points, sub-samples of worms were separated for digestion and plating in order to map CFU counts to the recorded green fluorescence signal in individual worms.

State separation

Worms were pre-colonized on 10^9 CFU/ml of MYb14-GFP-KmR for 24 hours as in Single Species Colonization. A small sub-sample of pre-colonized worms (n=100-200) were measured on Biosorter to establish gate boundaries for "high"" and "low" fluorescence bins. The measured Green range from the Biosorter for "high" was around $850-3950$ and for "low", it was $45-620$ (arbitrary units). The bulk remaining worms were then sorted into high and low bins based on the measured fluorescence signals ($n = 150$). Worms from each bin were then moved into each of two conditions: one where the original density of live fluorescent bacteria was provided, and one where worms were moved to an inert food source (S medium + 2X HKOP50 + 25 μg/ml chloramphenicol to prevent bacterial growth and re-inoculation). At 24 and 48 hours, worms were rinsed with M9TX01 to remove bacterial biomass, and green fluorescence was recorded on Biosorter for all individuals in the population. At 24 hours, all adult worms were retrieved after measurement (>99 % sorting retrieval efficiency), lightly surface bleached to prevent transfer of any contamination from the sorter, then returned to the originating condition until 48 hours. At 48 hours, green fluorescence

was recorded on Biosorter, and a sub-sample of individual worms ($n = 24 - 36$ per condition) were sorted into individual wells for disruption as in Single Worm Digests.

Accumulation and loss of inert fluorescent particles

In these experiments, germ-free adult N2 and *exp-1(sa6)* II worms were prepared according to standard protocols, then exposed to fixed concentrations of Fluoro-Max green fluorescent polymer microspheres (0.21 μm diameter, particle density in aqueous solution 1.05 g/cm^3, cat. G200) in M9 worm buffer + 0.01% Triton X-100 to help prevent clumping of microspheres.

A.1.6 Simulations and computational methods

The mean-field simulations (dashed black lines) in Figure 4.1 and Figure 4.2 were performed using python's scipy odeint solver [179]. The odeint solver was used to numerically integrate Eq. 4.2. Best fit parameters were found using scipy's curve_fit function to fit the log transformed simulations to log transformed data (Appendix A Table A.2). The fits were done in the log transformed space since the fluctuations were empirically more symmetric in the log space as compared to the real space. The chemical reaction like equations of the stochastic model (Eq. 4.1) were simulated using the Gillespie algorithm [165, 166]. The simulations were coded in python and were initialized using the best fit parameters from the mean field model. 30 Stochastic Gillespie simulations were performed per condition in Fig. 4.1. The stochastic simulations in Fig. 4.2 ($n = 24$, 10 repetitions) were initiated using the birth and death parameters from Table A.2, but using a colonization rate c that is scaled to the bacterial density outside the worm (scale factors: 1/10, 1, 10) and carrying capacity randomly picked from 48 hour data of the highest bacterial density condition. For stochastic simulations, error bars in zero occupancy at each timepoint are found by calculation means and standard deviations for zero occupancies across 10 repetitions.

For experimental data, the error bars are calculations using binomial standard deviation ($\sqrt{N \cdot p \cdot (1-p)}$, where p is the fraction of zeros at that timepoint and $N = 24$). These are then expressed in percentages (Fig. 4.2) for convenience.

In Fig. 4.3, we performed a grid search for best fit parameters for variable colonization and birth rates. We found the best fit by minimizing the negative log-likelihood of the data. We evaluated the log-likelihood of the data given a model by discretizing both the experimental data and the simulation data into three levels of bacterial load: low (0-$10^{1.5}$ for MYb71, 0-10 for MYb120), medium ($10^{1.5}$ - 10^4 for MYb71, 10-$10^{2.5}$ for MYb120), and high (above 10^4 for MYb71, above $10^{2.5}$ for MYb120) and calculating their relative probabilities. The negative log-likelihood is $\mathcal{L} = -\sum_{ij} n_{ij} \log(P_{i,j})$, where $n_{i,j}$ is the number of observed worms with bacteria at level i at time j, and $P_{i,j}$ is the corresponding probability within the model as measured using Gillespie simulations with $n = 24$ worms. We performed these simulations 50 times to produce the distribution of log-likelihoods shown in Fig. 4.3 b and d.

A Gaussian mixture model with two components was fit to log(GFP) data transformed into log(CFU) data in Figs. 4.4 and 4.5 using python's sklearn package [180]. Once fitted in the log(CFU) space, the distributions were then transformed back to log(GFP) (see Appendix A Transformation of GFP measurements to estimates for bacterial load in individual worms). The best fit parameters of the mixture model are reported in tables under each panel.

For Fig. 4.6, she stochastic differential equation of the potential model (Eq. 4.4) was simulated in python using the Euler-Maruyama method with a time step of 0.01. Similarly, the switching model Eq. 4.5 was also simulated in python using the Euler-Maruyama method along with a random state switching given by the transition rates α_H and α_L. Parameters for these simulations were set as described in Appendix A Probability distributions in the state switching model.

A.2 Logistic Model Fits for single species colonization

As previously described, bacterial load in worms was measured by destructive sampling at 3, 12, 18, 24, 36, 42, and 48 hours after initial colonization. Data for MYb71 and MYb120 are shown in Fig. 4.1. Here, we show the mono-colonization data for the other bacterial species in the minimal microbiome (Table A.1). We also show the respective Gillespie simulations ($n = 30$) using the parameters (Appendix 1 Table A.2) from mean-field equation fits.

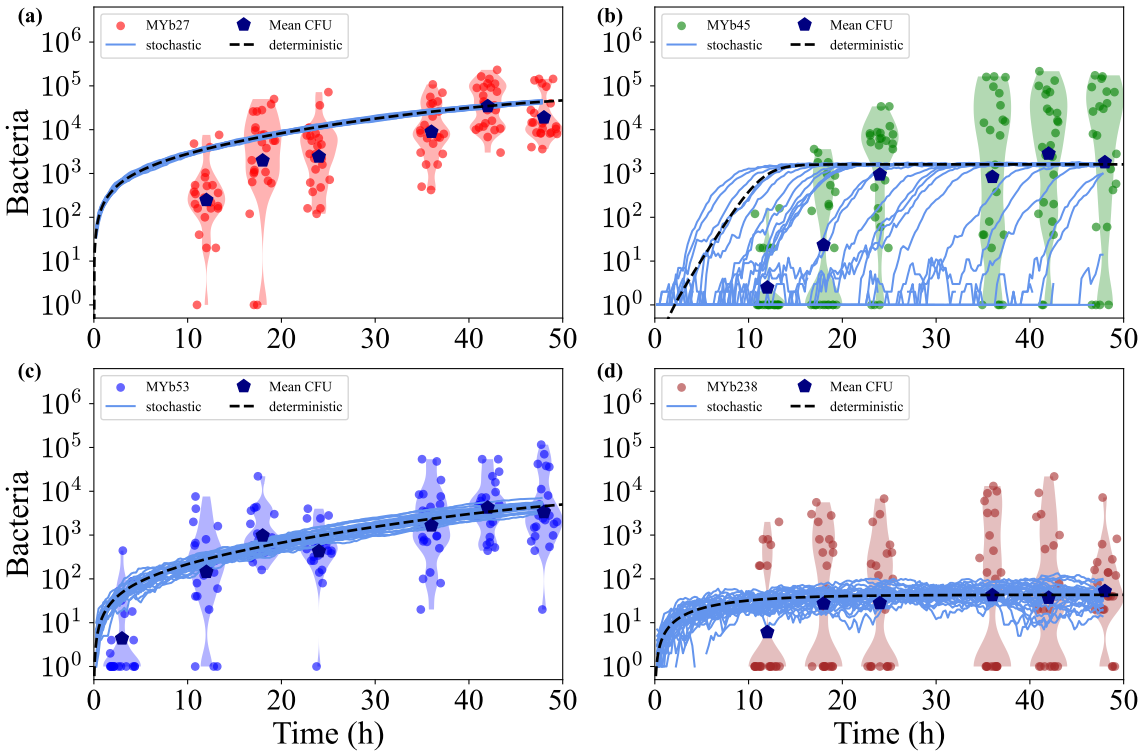

Figure A.1: **Bacterial load in individual worms over time.** Data are shown for bacterial species: a) MYb27 (red), b) MYb45 (green), c) MYb53 (blue), d) MYb238 (brown) to illustrate colonization dynamics. Gillespie simulations (blue lines, n=30) were carried out using parameters obtained from fitting CFU per worm data to the mean field model. Mean CFU at each time point (large blue point) and the mean-field deterministic solution (dashed black line) are also shown.

Species	V	c	b	d
MYb27	$1.02x10^6$	191.70	1.04	0.97
MYb45	$5.9x10^4$	0.19	2.80	2.04
MYb53	$1.38x10^4$	14.43	1.07	1.00
MYb71	$1.76x10^4$	0.07	1.23	0.58
MYb120	$1.47x10^2$	0.09	2.58	1.40
MYb238	$2.60x10^6$	5.85	0.85	0.99

Table A.2: **Parameters from logistic model fits to bacterial load data during mono-colonization of N2 worms** (Fig. 4.1, Appendix A Figure A.1)

A.3 Demographic noise model

The null model of bacterial birth, death, and migration described in the main text (Eq. 4.1) is a one species special case of the multi-species model described in our previous work [40]. The equation for the mean population density (ϕ_i) and its variance is derived via a system size expansion [181] of a master equation governing the probability of the number of bacteria within the gut as a function of time. The expansion results in a Fokker Planck equation governing the probability of the population density, from which it is possible to find an equivalent Langevin equation governing the mean population density and fluctuations around the mean. For a more detailed derivation, refer to the appendix of [40]. The resulting mean population density is described by the following differential equation (same as Eq. 4.2):

$$\frac{\partial \phi_i}{\partial t} = (1 - \phi_i)\left(b_i \phi_i + c_i\right) - d_i \phi_i, \tag{A.1}$$

where ϕ_i is the mean population density (X_i/V_i), and the parameters b_i, c_i, and d_i are the birth rate, migration rate, and death rate respectively. The predicted variance is:

$$C_{ii} = \frac{1}{V_i}\left[(1 - \phi_i(t))\left(b_i \phi_i(t) + c_i\right) + d_i \phi_i(t)\right], \tag{A.2}$$

where V_i is assumed to be the carrying capacity for each bacterial species and is also the well mixed volume governing the fluctuations.

A.4 Estimation of Ingestion and Excretion Rates

Ingestion rate The *C. elegans* intestine is colonized by ingested bacteria that survive transit through the pharyngeal grinder and enter the intestine as live cells. Colonization rate is a function of the density of bacteria in the colonizing inoculum [10] and is an easily-accessible experimental knob in this system, as well as a potential source of variation between individuals. We therefore sought to understand individual variation in ingestion rate among adult worms exposed to a shared environment.

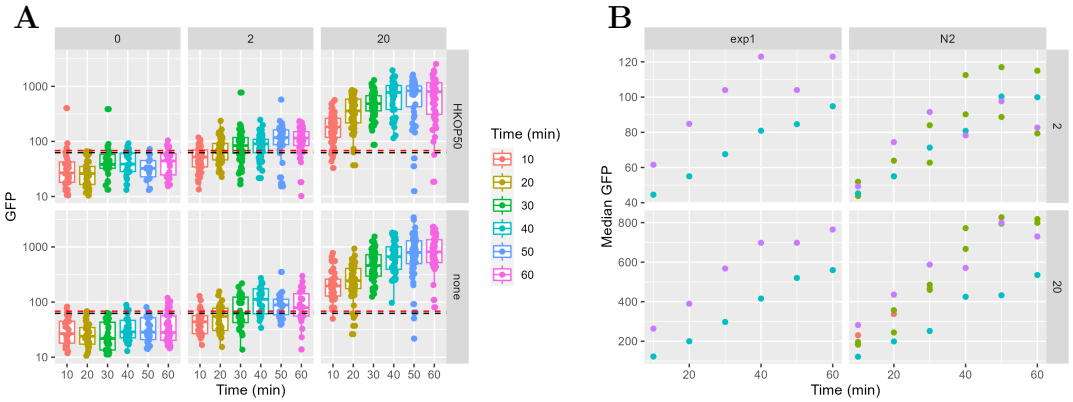

Figure A.2: **Fluorescent bead accumulation in adult worms.** (A) Raw data. Worms were exposed to high (20) or low (2) concentrations of beads (top labels). Additional nutrient source (heat-killed OP50 or none) is shown on the vertical labels. Samples were taken 10-60 minutes after exposure to beads, and total green fluorescence was measured on BioSorter. Each point represents one individual worm. Horizontal lines represent 90th percentile GFP in bead-free worms (red, HKOP50; black, no nutrient source). (B) Median GFP bead accumulation in N2 wild-type and *exp-1* defecation mutant. Each color represents one independent run of the experiment, carried out on different days.

To this end, we provided synchronized adult N2 (wild-type) or *exp-1* (defecation cycle mutant) worms with *E. coli* sized fluorescent beads (0.21 µm) suspended in worm buffer and monitored acquisition of beads over time. Beads were provided at a high (20 µL per 1 mL buffer) or low (2 µL) concentration; bead-free worms (0

beads) were used as controls to determine auto-fluorescence thresholds. During bead ingestion, worms were either provided with heat-killed OP50 ("HKOP50") as an inert but nutritious food source to encourage pumping, or given only the indigestible beads in suspension.

Worms accumulated fluorescent beads over time at an apparently constant mean rate (Appendix A Fig. A.2). There was much more bead accumulation in the high-bead condition (20 µL/mL) than in the low-bead condition (2 µL/mL), as expected. Across conditions, bead signal in the worm intestine begins to saturate by 40-50 minutes, prior to which there is a linear regime; this is consistent across experimental runs (Appendix A Fig. A.2B). Further, no-food and heat-killed-food conditions are very similar in overall bead accumulation. This is more consistent with an input-output balance than with the worm gut filling to capacity, and not consistent with the idea that worms can distinguish between different types of particles when feeding in liquid [182].

To examine the underlying distribution of ingestion rates, we turn to a null model where acquisition rate in the linear regime is a first-order function of encounters between worms and beads, and where there are no differences between individual worms. This model suggests that the fraction of worms with detectable bead load over time can be approximated as:

$$-\ln\left(\frac{S(t)}{S_0}\right) = \beta G t. \tag{A.3}$$

Here, $S(t)$ and S_0 are the number of non-fluorescent individual worms at time t and at the start of the run respectively, G is the bead density, and β is the rate constant representing average bead uptake in the population. This model further indicates that movement to the "fluorescent" state should be 10X faster in the high bead condition than in the low bead condition. Fitting this model to the high-bead condition data, we obtain estimates $\beta G = -0.009$ min-1 (± 0.002) for N2 and -0.014

min-1 ($\pm$0.003) for *exp-1*, indicating a slightly greater accumulation rate in the exp mutant than in wild-type. Both hosts show the expected linear relationship between signal acquisition and time. Further, simply dividing these estimates by 10 provides a good fit to the data from the low-bead conditions, consistent with the ten-fold lower concentration of beads used in these samples (Appendix A Fig. A.3). Collectively, this indicates that the population-wide mean is broadly representative for ingestion in worms, suggesting that individual heterogeneity in this rate represents draws from a single underlying distribution.

These data do not indicate the existence of sub-populations of worms with distinct parameters for ingestion, and a model with individual heterogeneity performs best at describing the observed variation. Variation in green bead fluorescence among individual worms (Appendix A Fig. A.4) is substantially in excess of that predicted by a simple null model in which bead input is proportional to bead concentration in the buffer (G) and bead excretion is proportional to concentration in the gut (N):

$$\frac{dN}{dt} = mG - eN. \tag{A.4}$$

Here, all worms are identical and have the same values for ingestion rate m and excretion rate e. Under this null model ("Null"), we expect that the coefficient of variation of bead load across individuals will decrease as gut load N increases and will be lower at higher bead concentrations G. In the data, we observe that CV is nearly constant over a wide range of bead loads (GFP signal per worm) and that this relationship does not change substantially across an order of magnitude in bead concentration, contrary to the null model expectation. Allowing worms to differ from one another by drawing parameters from a common underlying distribution weakens the relationship between mean and CV of bead load; the qualitative trends in the data are recapitulated by assuming uniform distributions (both m and e vary across

[0.5X, 2X] of the central values) but not Gaussian (both rates drawn from $\mathcal{N}$(rate, sqrt(rate)). These distributions were chosen to reflect wide vs narrow parameter ranges rather than for any specific features. Adding white (technical) noise to the simulated data does not materially alter these observations.

Excretion These experiments were extended to estimate excretion rates for non-adhered particles in the worm intestine. These values are not intended to reflect loss of microbiome community bacteria, which are adhered to the intestine. Instead, these observations provide insight into total fluid movement and loss of detached, free-moving particles in a crowded gut.

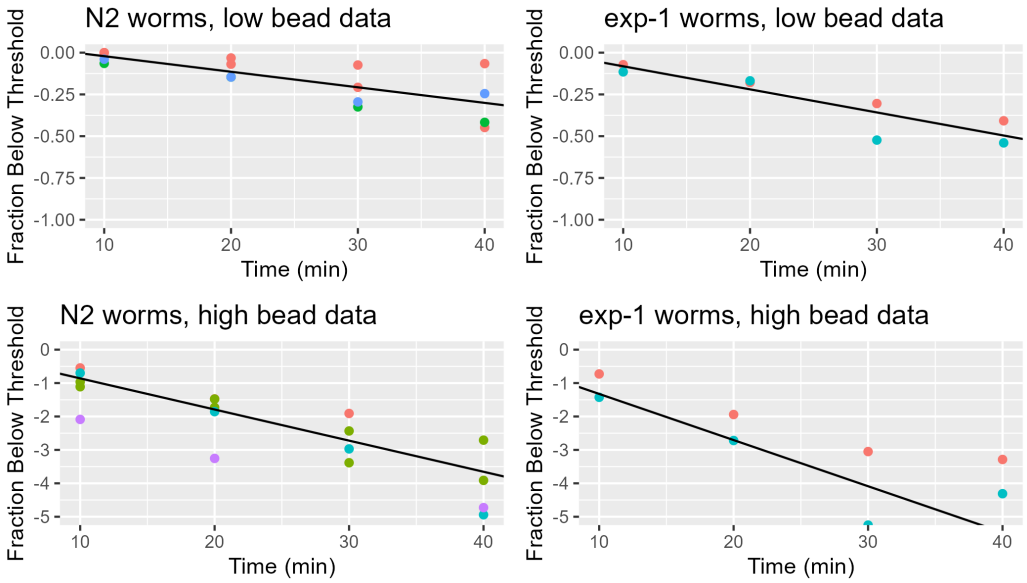

Figure A.3: **A model assuming homogeneous, density-dependent ingestion of beads is adequate to describe population-level data.** The linear "susceptibility" model was fitted to high-bead data in the linear regime, and the resulting rate was divided by 10 to recapitulate observations in the low-bead data (1/10 bead concentration).

Briefly, worms were allowed to accumulate beads under the high-bead condition for 75 minutes, chilled to stop pumping, rinsed to remove external beads, and divided randomly across wells with S medium + 1X HKOP50 in a 96-well plate to allow bead excretion. At each time point, worms were put through BioSorter to measure GFP

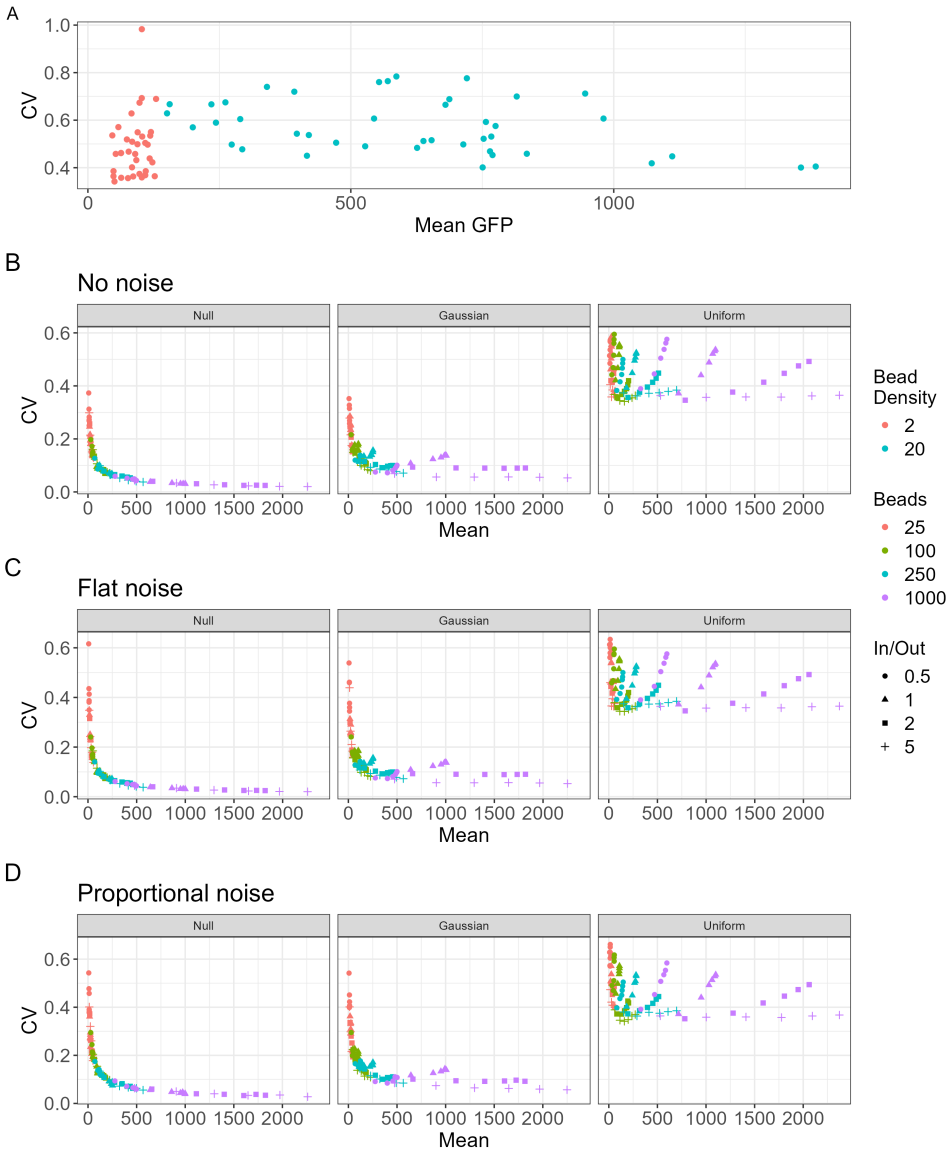

Figure A.4: **Variation in bead load is best explained by a model with wide individual heterogeneity.** (A) In the data, we observe that CVs of GFP/worm measurements within samples vary little if at all with the mean. (B) Gillespie simulations ($n = 100$ "worms" per "sample") show a marked relationship between mean and CV in the simple input/output model, which is altered slightly with Gaussian worms (narrow individual heterogeneity). When allowing uniform worms (wider heterogeneity), the CV and mean are nearly uncorrelated over a wide parameter space. "Beads" refers to the numeric value given for bead concentration in the external reservoir; rate parameters m and e vary over [0.04, 0.1]; "In/Out" is the ratio m/e. Adding white technical noise to the simulated data does not alter these observations when imposing either (C) constant "flat" machine noise $\mathcal{N}(0, \sqrt{10})$ or (D) "proportional" noise $\mathcal{N}(\text{GFP}, \sqrt{\text{GFP}})$.

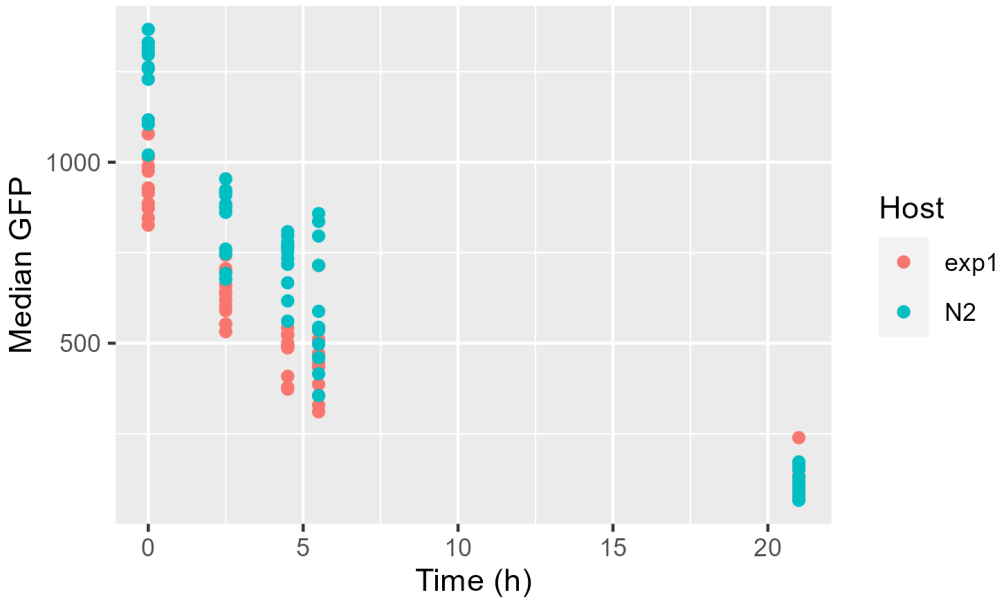

Figure A.5: **Excretion of GFP beads follows an exponential curve on a population level.** Each data point represents median GFP of one well (10-50 worms).

fluorescence; as many worms as possible from each well were recovered by sorting, so that the same worms are being measured over time within each well. We confirmed that repeated passage through the sorter does not damage the worms or photo-bleach the bead contents (data not shown).

The resulting trajectories indicate roughly exponential decay of luminal fluorescence over time, with a slightly higher rate constant for N2 than for the defecation cycle-defective mutant *exp-1* (-0.1 vs -0.08 h-1) (Appendix A Fig. A.5). As with the data for accumulation of beads, these data do not indicate sub-populations of individuals with fundamentally different excretion rates.

A.5 Additional Conditions for Inhibition of Bacterial Growth in the Intestine

MYb14-GFP-KmR pre-colonized wild-type worms were moved to 100μg/ml and 250μg/ml chloramphenicol, in addition to the conditions previously described in Fig. 4.4 in the

main text. These additional inhibition conditions show similar trends as in the conditions shown in the main text, where higher inhibition resulted in more worms in the "low" fluorescence sub-population. This result further indicates the emergence of sub-populations in total bacterial load.

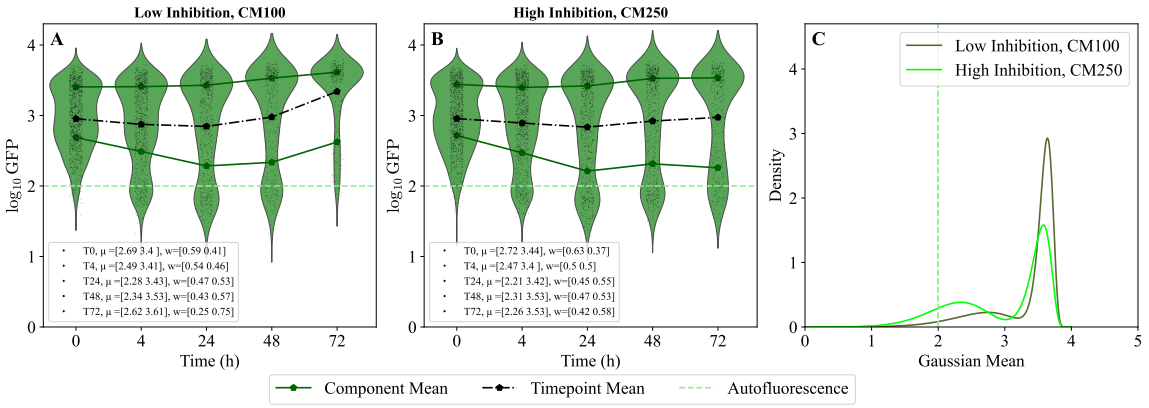

Figure A.6: **Bacterial load distributions under additional levels of inhibition of growth within hosts.** Green fluorescence in MYb14-GFP-KmR pre-colonized worms over 72 hours of inhibition at (a) 100μg/ml or (b) 250μg/ml concentrations of chloramphenicol (CM). Centers and weights of high and low GFP modes at each time point from the transformed Gaussian mixture model fits are shown in the legend. Mean GFP (black dots, dashed lines) for the entire population at each time point is shown. Mean autofluorescence (Light green, dashed lines) calculated using the data from uncolonized worms is also shown. (c) Probability density fits modeled as a Gaussian mixture with two components fit on CFU transformed data and then transformed back to GFP, at T72 for CM100 and CM250 inhibition.

A.6 Run to run variation

Wild type worms were colonized with MYb14-GFP-KmR for 24 hours before being separated into high and low bins, as described before. Green fluorescence was measured 24 and 48 hours post separation. While the experimental setup was similar to that of Fig. 4.5 in the main text, there was higher loss of worms (through washing in protocols) by 48 hours. Despite the smaller number of worms, we see similar trends as in the other run, with re-distribution of individual worms between apparent states in total bacterial load as measured by GFP fluorescence.

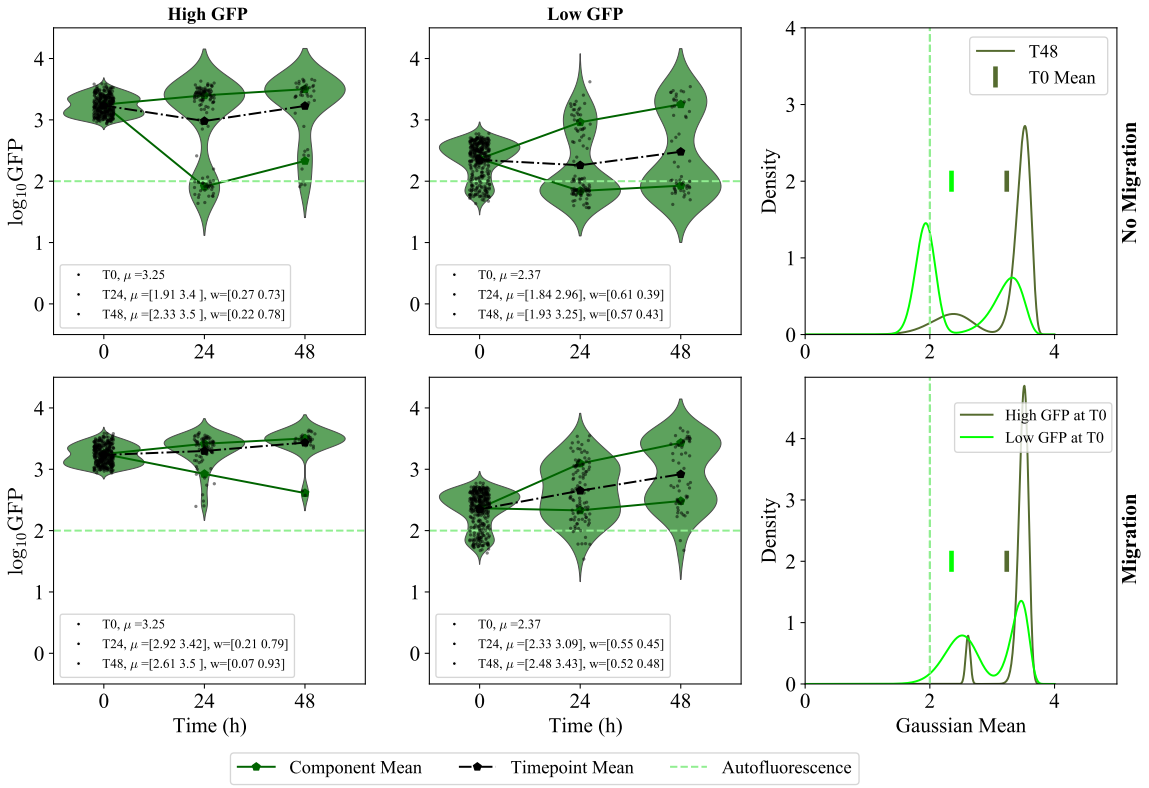

Figure A.7: **Additional run of Migration rate experiment .** Green fluorescence over 48 hours after MYb14-GFP-KmR pre-colonized worms were separated based on high (a,e) and low (b,f) GFP under conditions of a-c) No Migration (top) or e-f) Migration (bottom). Full T0 distribution (pale green) in fluorescence is shown in the background. Mean GFP (black dots, dashed lines) for the entire population at each time point is shown. Mean auto-fluorescence (Light green, dashed lines) calculated using the data from uncolonized worms is also shown. c,f) PDFs using transformed GMM fits at T48 for worms starting at low (light green) and high (dark green) fluorescence in no migration (top) and migration (bottom) conditions.

A.7 CFU to GFP Mapping

Wild type worms were colonized with MYb14-GFP-KmR for 24 hours as before, then run through Biosorter to measure the GFP fluorescence. During the sorter run, individual worms were sorted out for quantification of bacterial load according to standard protocols for this lab [58]. Plotting of GFP fluorescence vs bacterial load for individual adult worms indicated an approximately monotonic GFP to CFU mapping (Appendix A Fig. A.8C) which further facilitated our analysis of experimental data

and modeling approaches. The log CFU to log GFP mapping was fit to a hyperbolic tangent function of the form:

$$y(x) = a \cdot \tanh((x - b)/c), \tag{A.5}$$

and best fit parameters were found to be $a = 4.00$, $b = 0.884$, and $c = 3.064$.

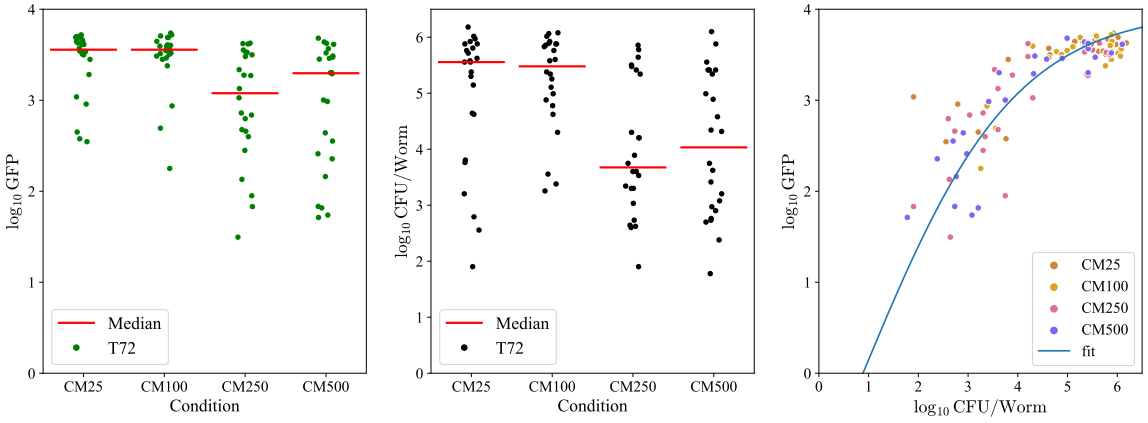

Figure A.8: **Comparison of GFP and CFU distribution** a) Green fluorescence in worms ($n = 24$) measured in Biosorter at different inhibition conditions. b) CFU/worm for the same set of worms measured through destructive sampling in all four inhibition conditions. Medians (red) for each condition for both Green and CFU/worm are also show. c) Green vs CFU/worm mapping for each worm colored by inhibition condition.

A.7.1 Transformation of GFP measurements to estimates for bacterial load in individual worms

As shown in Appendix A Figure A.8, the relationship between the concentration of bacteria and the amount of fluorescence detected is not linear. In particular, near the maximum threshold for the machine, the reported GFP becomes more non-linear, compressing large CFUs measurements into a smaller range of reported GFP. This has a consequence of making a bacterial load distribution that was originally symmetrical skewed in the GFP space, as the right side of the distribution is more compressed

than the left.

In our models, all fits are done in the log(CFU) space, where we expect the relationship between the true bacterial load and the measurement to be more linear. Thus we transform the data into log(CFU) space before fitting. The transformation from log(GFP) (y) to log(CFU) (x) is given by

$$x(y) = \frac{c}{2} \ln\left(\frac{1 + y/a}{1 - y/a}\right) + b, \tag{A.6}$$

where a, b, and c are the same parameters fitted earlier. The data in the log(CFU) space is more symmetric than in log(GFP) space and can be fitted well by a Gaussian mixture model with just two Gaussian components.

It is possible to transform probability distributions back to the log GFP space via a change of variables:

$$P(y) = P(x(y)) \left|\frac{\partial x}{\partial y}\right| = P\left(\frac{c}{2} \ln\left(\frac{1 + y/a}{1 - y/a}\right) + b\right) \frac{c/a}{1 - (y/a)^2}, \tag{A.7}$$

where $P(x)$ is a distribution fitted in the log(CFU) space. Appendix A Fig. A.9A shows an example fit of a Gaussian mixture model of two components to data from Fig. 4.4 at 24 hours, fitted to log(CFU) data transformed using Eq. A.6. Panel B shows the same data in log(GFP) space and the pdf of the transformed GMM model using Eq. A.7. Tables A.3 and A.4 show the means, standard deviations, and weights of a two component GMM model fit to transformed log(CFU) data.

A.7.2 Modeling in the log(CFU) space

As described in the previous section, we chose to model our experiments in the log(CFU) space, which we consider to be more easily related to real bacterial loads. Additionally, the fluctuations in log(CFU) space are more symmetric, making fitting models easier.

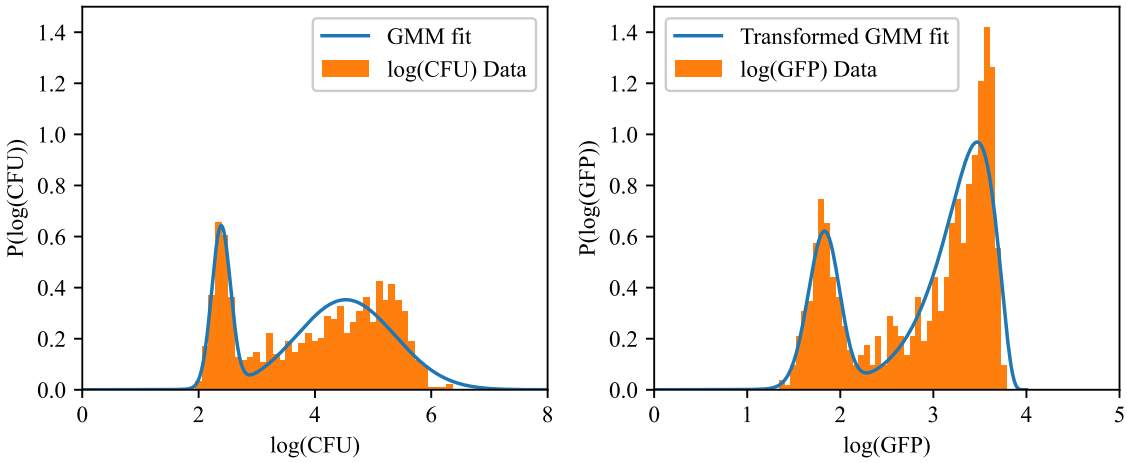

Figure A.9: **Probability distributions of GFP and CFU data.** Left: log(CFU) probability distribution using transformed log(GFP) from Fig. 4.4 at 24 hours. A Gaussian mixture model (GMM) with two components is fitted to the log(CFU) data. Right: The GMM distribution fitted in the log(CFU) space is transformed back to the log(GFP) space.

Condition	Time (h)	Mean 1	Mean 2	Std 1	Std 2	Weight 1	Weight 2
CM25	0	3.40	4.76	0.47	0.49	0.62	0.38
CM25	4	3.01	4.66	0.53	0.55	0.49	0.51
CM25	24	2.39	4.53	0.16	0.84	0.26	0.74
CM25	48	2.90	5.33	0.37	0.47	0.25	0.75
CM25	72	3.46	5.56	0.56	0.40	0.22	0.78
CM500	0	3.32	4.69	0.48	0.53	0.57	0.43
CM500	4	3.08	4.69	0.54	0.55	0.51	0.49
CM500	24	2.87	4.69	0.56	0.56	0.47	0.53
CM500	48	2.88	4.95	0.54	0.51	0.46	0.54
CM500	72	2.75	4.89	0.43	0.57	0.44	0.56

Table A.3: **Raw parameters from the Gaussian mixture model in the log(CFU) space fitted to data in Fig. 4.4.**

The question then arises what the equivalent model in the CFU (not logarithmic) space is. This is answered by performing a stochastic change of variables using Ito's lemma. Equation 4.4 of the main text undergoes a transformation under the change of variables $w = exp(\phi)$ becoming:

$$\frac{\partial w}{\partial t} = f\left(\ln(w)\right) \cdot w + \frac{Dw}{2} + \sqrt{D} w \eta, \tag{A.8}$$

Condition	Time (h)	Mean 1	Mean 2	Std 1	Std 2	Weight 1	Weight 2
High -	0	4.36	4.36	0.40	0.40	1.00	1.00
High -	24	2.41	4.82	0.15	0.34	0.48	0.52
High -	48	2.78	4.96	0.33	0.42	0.44	0.56
Low -	0	3.09	3.09	0.32	0.32	1.00	1.00
Low -	24	2.37	3.82	0.11	0.54	0.71	0.29
Low -	48	2.41	4.47	0.17	0.51	0.68	0.32
High +	0	4.32	4.32	0.41	0.41	1.00	1.00
High +	24	3.57	4.89	0.41	0.26	0.34	0.66
High +	48	3.27	5.00	0.84	0.33	0.29	0.71
Low +	0	3.14	3.14	0.28	0.28	1.00	1.00
Low +	24	3.23	4.41	0.45	0.49	0.63	0.37
Low +	48	3.59	4.97	0.48	0.28	0.61	0.39

Table A.4: **Raw parameters from the Gaussian mixture model in the log(CFU) space fitted to data in Fig. 4.5.**

where the $Dw/2$ is a drift term and η is a Gaussian white noise. This transformed equation has multiplicative noise and, as long as f is a polynomial, it prohibits any kind of pure migration term in the traditional sense of a constant growth rate. Our best fit models thus need to be interpreted accordingly.

A.8 Probability distributions in the state switching model

Bacteria populations in both the explicit state switching model and the potential model have transitions between two distinct states, visible in these data as modes in the distribution of the total bacterial load. For each class of models, a master equation describes the probability of a system being in the high or low bacterial load state as well as the transition rates between states. For the explicit state switching model, these transition rates are parameters of the model. In contrast, in the potential model, the transition rates between states is given by properties of the potential of each state.

In the simplest case of the state switching model, transition rates are assumed to be constant. Given a set of transition rates between states $s_{\text{low}} \xrightarrow{\alpha_H} s_{\text{high}}$ and $s_{\text{high}} \xrightarrow{\alpha_L} s_{\text{low}}$ the corresponding master equation for the probabilities of being in the high $P(s_H)$ and low state $P(s_L)$ are:

$$\frac{\partial P(s_H)}{\partial t} = \alpha_H P(s_L) - \alpha_L P(s_H) \tag{A.9}$$

$$\frac{\partial P(s_L)}{\partial t} = -\alpha_H P(s_L) + \alpha_L P(s_H) \tag{A.10}$$

Assuming that an individual worm must be in one of the two states at any given time, $P(s_H) + P(s_L) = 1$, the probability of being in the low state can be expressed as the complement of being in the high state: $P(s_L) = 1 - P(s_H)$. Using this together with Eq. A.9 one can solve for the probability of being in the high state as a function of time.

$$\frac{\partial P(s_H)}{\partial t} = \alpha_H - (\alpha_H + \alpha_L)P(s_H). \tag{A.11}$$

This is solved as:

$$P(s_H, t) = Ae^{-(\alpha_H+\alpha_L)t} + \frac{\alpha_H}{\alpha_H + \alpha_L}, \tag{A.12}$$

resulting in steady state values $P(s_H) = \frac{\alpha_H}{\alpha_H+\alpha_L}$ and $P(s_H) = \frac{\alpha_L}{\alpha_H+\alpha_L}$. Best fit results of Eq. A.12 to the weights of a Gaussian mixture model fit to MYb14-GFP-KmR precolonized worms at low inhibition result in transition rates $\alpha_H = 0.082(1/\text{h})$ and $\alpha_L = 0.025$ (1/h) (Fig 4.4, Appendix A Fig A.10).

We can use these results together with the stationary probability distributions of each state separately to predict the stationary probability distribution of the the full ensemble. In this model, states can be considered in isolation as they are uncoupled except through transitions. The stationary distribution for an individual state in the absence of the other is $A_s \exp(-U_s(\phi)/D(s))$, where A_s is a normalization constant and $U_s(\phi) = -r_s\phi^2(C_s/2 - \phi/3)$ is a potential corresponding to the force $-\frac{\partial}{\partial\phi}U_s(\phi) =$

$r_s\phi(C-\phi)$.

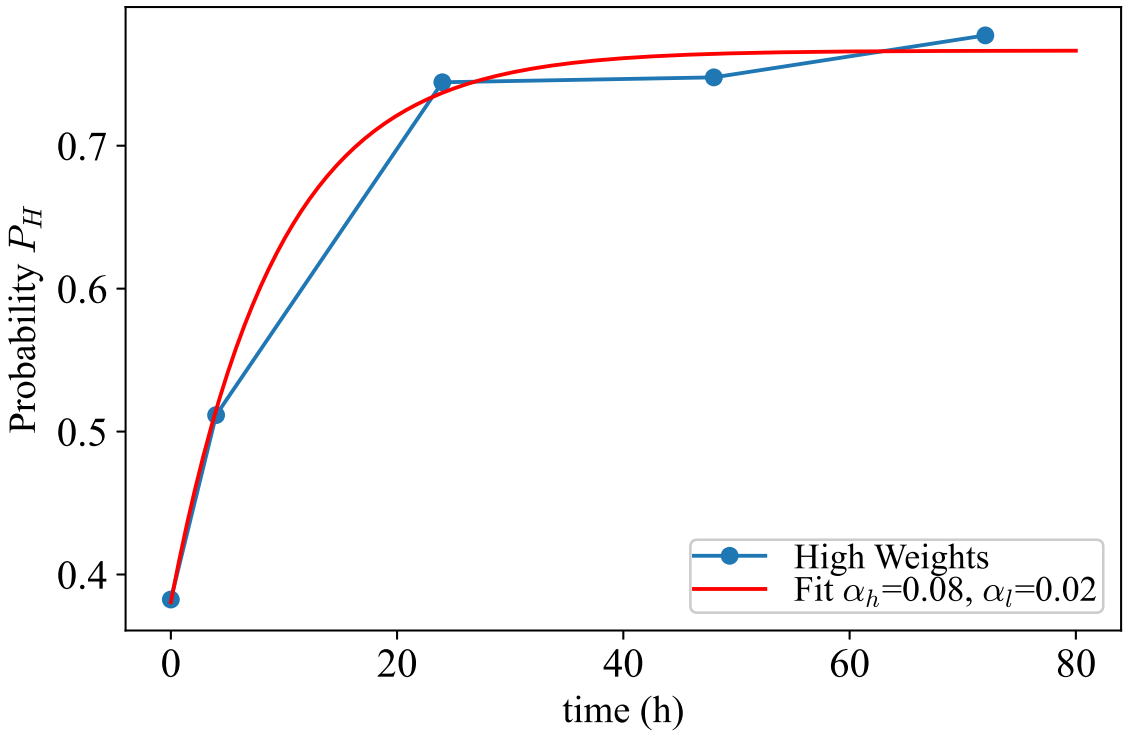

Figure A.10: **Weights of the high mode in a Gaussian mixture model** fit to the Green fluorescence transformed CFU data in MYb14-GFP-KmR precolonized worms over 72 hours of at low inhibition concentrations of chloramphenicol (Fig. 4.4). The weights serve as a proxy for $P(s_H)$ and a fit of Eq. A.12 results in transition rates $\alpha_H = 0.08$ (1/h) and $\alpha_L = 0.02$ (1/h).

The full stationary probability distribution can be thus approximated as:

$$P(\phi) = \frac{\alpha_H A_H}{\alpha_H + \alpha_L} \exp(r_H\phi^2(C_H/2 - \phi/3)/D_H) + \frac{\alpha_L A_L}{\alpha_H + \alpha_L} \exp(r_L\phi^2(C_L/2 - \phi/3)/D_L) \tag{A.13}$$

as long as transitions between states happens very fast compared to the other timescales in this problem.

A.9 Probability distributions in the potential model

There exists a set of well known results from statistical mechanics for the transition rate of a particle from a potential well to another over an energy barrier. This problem is known as Kramer's[183], problem and it obeys an Arrhenius like equation:

$$\alpha_L = \frac{\sqrt{K_H K_M}}{2\pi} \exp\left(\frac{-(U(C_M) - U(C_H))}{D}\right), \tag{A.14}$$

$$\alpha_H = \frac{\sqrt{K_L K_M}}{2\pi} \exp\left(\frac{-(U(C_M) - U(C_L))}{D}\right), \tag{A.15}$$

where $K_L = |U''(C_L)| = |f'(C_L)| \approx \frac{D}{\sigma_L^2}$, $K_M = |U''(C_M)| = |f'(C_M)|$, and $K_H = |U''(C_H)| = |f'(C_H)| \approx \frac{D}{\sigma_L^2}$. C_L is the lower stable state, C_H is the higher stable state, and C_M is the location of the peak between these two states. Additionally, at equilibrium the stationary distributions should have a form:

$$P(\phi) = A \exp\left(\frac{-U(\phi)}{D}\right). \tag{A.16}$$

One feature of Kramer's result is that the switching rates depend on the variance, curvature, values of the peaks and troughs, and other features of the potential. In the switching model, these rates could in theory be independently set and be independent of the variance around each fixed point.

We can fit models for the potential to an effective potential determined directly from data.

$$\frac{U_{\text{eff}}(\phi)}{D} = R(\phi) = -\ln(P(\phi)) \tag{A.17}$$

where $P(\phi)$ is a histogram approximation of the probability distribution of the log transformed CFU data. In Appendix A Fig. A.11, best fits are found for a 6th order potential and a 4th order potential. The Gaussian mixture model can also be viewed as generating its own effective potential as the negative log of the mixture distribution.

For comparison, this effective potential its corresponding force are also plotted.

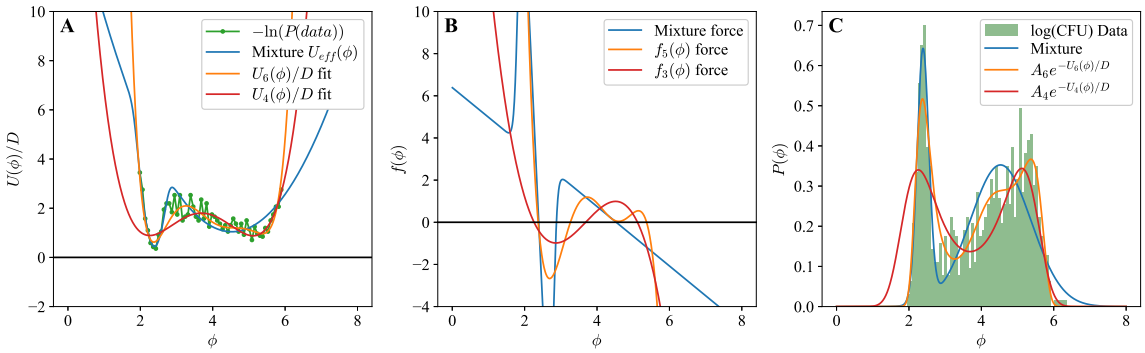

Figure A.11: **Effective potentials and forces of different models.** A) Fits to the effective potential $-\log(P(\phi))$ for the Gaussian mixture model, a 6th order polynomial potential $U_6(\phi)$ and a 4th order potential $U_4(\phi)$. B) The corresponding force functions for the Gaussian mixture model, the 6th order potential (f_5 5th order force), and the 4th order potential (f_3 3rd order force). C) The corresponding fits of the probability distributions for all three models.

It is possible to further solve for D in terms of the ratio of the effective potential to D, denoted via R, its second derivative, and the measured transition rates from equation A.14:

$$D = \frac{\alpha_L 2\pi}{\sqrt{R''(C_H)R''(C_M)}} \exp\left(R(C_M) - R(C_H)\right) \tag{A.18}$$

In Figs. A.12 and A.13, both the potential model and the switching model are simulated and compared to the Gaussian mixture model fit to data. The parameters for the Gaussian Mixture model and Potential models were fit directly to data and the parameters for the switching model were inferred from the means, variances, and weights of a Gaussian mixture model fit to one data set. For this fit, we used the 24 hour time point in the low inhibition experiment of figure 4.4. This time point is 72 hours after the *C. elegans* were initially colonized and is, therefore, on the same day of adulthood as the 48 hour time point of the no migration condition of Fig. 4.5. In this context, the main difference between these two time points is that in Fig. 4.5 the population is filtered to separate *C. elegans* with high or low populations of bacteria.

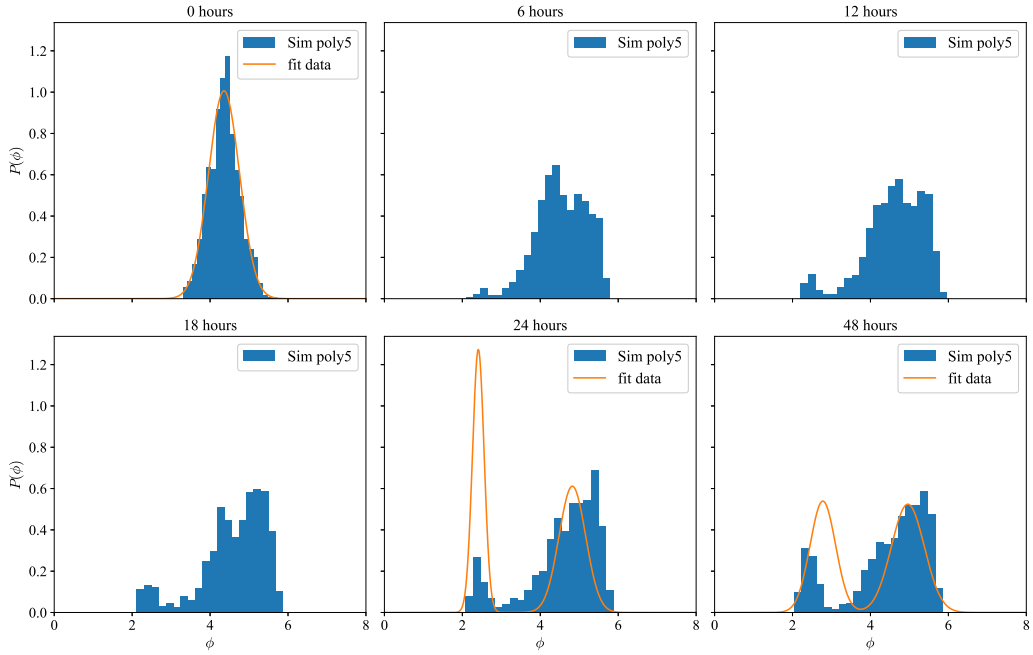

Figure A.12: **Simulations of the 6th order potential model using parameters that were initialized from the Gaussian mixture model fits to data from Fig. 4.4 at 24 hours.** The initial starting density distribution was taken from the no migration initial condition of the High GFP condition of Fig. 4.5. The simulation is shown every 6 hours and is compared to data fit at points (0, 24, 48 hours) of Fig. 4.4.

This allows us to compare the observed re-distribution of individuals across states in Fig. 4.5 with predictions from simulations initialized using the same distributions of individuals. In both simulations, the low sub-population quickly recovers to the original distribution that was fit. The simulations reach steady state at a faster time scale than observed in the experimental data. The simulations do, however, capture the means and the qualitative dynamics observed from the experiment.

The main distinction between the state switching and the potential models has to do with their dynamics. For the state switching model, the rates of switching are parameters, which can be tuned independently of the curvatures of the potentials. For the multistable potential model, the curvatures of the potential (and hence the variance of the fluctuations) contribute to controlling the switching rate. Measuring the switching rate and observing its relationship to the fluctuations about a state in

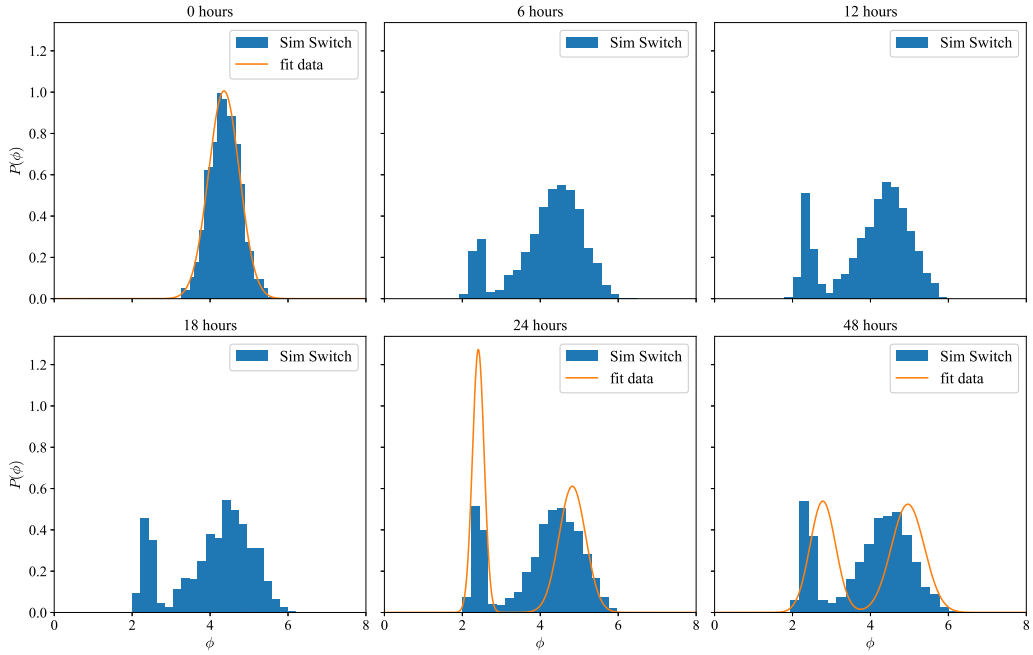

Figure A.13: **Simulations of the switching model using parameters that were initialized from the Gaussian mixture model fits to data from Fig. 4.4 at 24 hours**. The initial starting density distribution was taken from the no migration initial condition of the High GFP condition of Fig. 4.5. (Top Row) The simulation is compared to data fit at points (0, 24, 48 hours) of Fig. 4.4. The simulation has dynamics in the first 9 hours and then remains in steady state (bottom row).

longitudinal data would be one way to distinguish between these models.

A.10 State switching with other bacteria

Although the focus of our experiments was on the commensal MYb14-GFP, state switching in total bacterial load can be observed in worms colonized with other bacterial species as well. For example, in an unrelated experiment [162], N2 worms colonized with GFP labeled *Salmonella enterica* LT2 were separated into high- and low-fluorescence bins, surface bleached, and transferred individually into wells of a 96-well plate containing S medium + heat-killed OP50 + kanamycin for selection. In parallel, a sample of worms from each gate was treated according to standard protocols (see Materials and Methods) and individual worms were mechanically disrupted

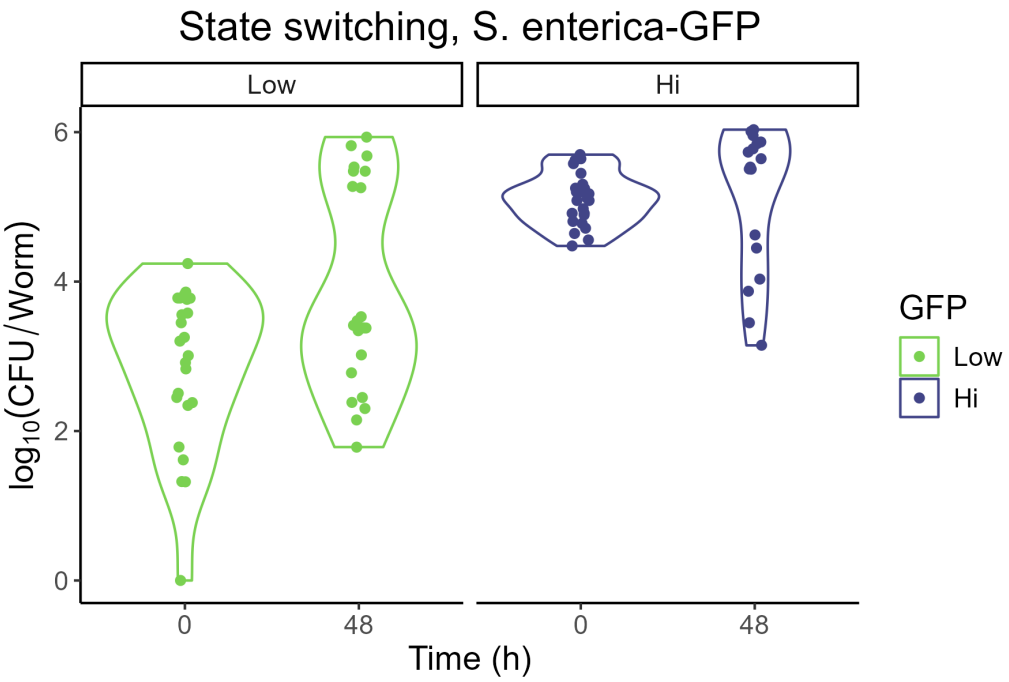

Figure A.14: **State switching in N2 adults colonized with *Salmonella enterica* LT2.** Adult worms were allowed to feed on lawns of *S. enterica*-GFP for 48 hours, then purged and sorted into bins based on GFP fluorescence as before. Individual worms were distributed into wells of a 96-well plate containing S medium + 1X heat-killed OP50 + 50 μg/mL each kanamycin (for selection) and chloramphenicol (to prevent re-inoculation) for 48 hours. Individual worms (n=24) were digested at the start (time 0) and end (time 48) of the experiment.

for measurement of bacterial load. After 48 hours, worms were retrieved from wells, and bacterial load was measured from these individuals. We observed that, as with MYb14-colonized worms, distributions of bacterial load shifted over time, with some low-GFP individuals transitioning to a highly-colonized state and vice versa (Fig. A.14).

Bibliography

[1] Emiley A Eloe-Fadrosh and David A Rasko. The human microbiome: from symbiosis to pathogenesis. *Annual review of medicine*, 64(1):145–163, 2013.

[2] Sambhawa Priya and Ran Blekhman. Population dynamics of the human gut microbiome: change is the only constant. *Genome biology*, 20:1–4, 2019.

[3] Simon Bahrndorff, Tibebu Alemu, Temesgen Alemneh, and Jeppe Lund Nielsen. The microbiome of animals: implications for conservation biology. *International journal of genomics*, 2016(1):5304028, 2016.

[4] Tanya Yatsunenko, Federico E Rey, Mark J Manary, Indi Trehan, Maria Gloria Dominguez-Bello, Monica Contreras, Magda Magris, Glida Hidalgo, Robert N Baldassano, Andrey P Anokhin, et al. Human gut microbiome viewed across age and geography. *nature*, 486(7402):222–227, 2012.

[5] Emily R Davenport, Orna Mizrahi-Man, Katelyn Michelini, Luis B Barreiro, Carole Ober, and Yoav Gilad. Seasonal variation in human gut microbiome composition. *PloS one*, 9(3):e90731, 2014.

[6] Elisa Maritan, Andrea Quagliariello, Enric Frago, Tomaso Patarnello, and Maria Elena Martino. The role of animal hosts in shaping gut microbiome variation. *Philosophical Transactions of the Royal Society B*, 379(1901):20230071, 2024.

[7] Gwen Falony, Marie Joossens, Sara Vieira-Silva, Jun Wang, Youssef Darzi, Karoline Faust, Alexander Kurilshikov, Marc Jan Bonder, Mireia Valles-Colomer, Doris Vandeputte, et al. Population-level analysis of gut microbiome variation. *Science*, 352(6285):560–564, 2016.

[8] Anthony Ortiz, Nicole M Vega, Christoph Ratzke, and Jeff Gore. Interspecies bacterial competition regulates community assembly in the c. elegans intestine. *The ISME Journal*, 15(7):2131–2145, 2021.

[9] Deepika Sundarraman, Edouard A Hay, Dylan M Martins, Drew S Shields, Noah L Pettinari, and Raghuveer Parthasarathy. Higher-order interactions dampen pairwise competition in the zebrafish gut microbiome. *MBio*, 11(5):10–1128, 2020.

[10] Nicole M Vega and Jeff Gore. Stochastic assembly produces heterogeneous communities in the caenorhabditis elegans intestine. *PLoS Biology*, 15(3):e2000633, 2017.

[11] Jason Z Chen, Zeeyong Kwong, Nicole M Gerardo, and Nic M Vega. Ecological drift during colonization drives within-host and between-host heterogeneity in an animal-associated symbiont. *Plos Biology*, 22(4):e3002304, 2024.

[12] Rachel D Moloney, Lieve Desbonnet, Gerard Clarke, Timothy G Dinan, and John F Cryan. The microbiome: stress, health and disease. *Mammalian genome*, 25:49–74, 2014.

[13] Ilseung Cho and Martin J Blaser. The human microbiome: at the interface of health and disease. *Nature Reviews Genetics*, 13(4):260–270, 2012.

[14] Maria Gloria Dominguez-Bello, Filipa Godoy-Vitorino, Rob Knight, and Martin J Blaser. Role of the microbiome in human development. *Gut*, 68(6):1108–1114, 2019.

[15] Nabil Bosco and Mario Noti. The aging gut microbiome and its impact on host immunity. *Genes & Immunity*, 22(5):289–303, 2021.

[16] Maayan Levy, Eran Blacher, and Eran Elinav. Microbiome, metabolites and host immunity. *Current opinion in microbiology*, 35:8–15, 2017.

[17] Nicholas M Vogt, Robert L Kerby, Kimberly A Dill-McFarland, Sandra J Harding, Andrew P Merluzzi, Sterling C Johnson, Cynthia M Carlsson, Sanjay Asthana, Henrik Zetterberg, Kaj Blennow, et al. Gut microbiome alterations in alzheimer's disease. *Scientific reports*, 7(1):13537, 2017.

[18] Yan Wang and Lloyd H Kasper. The role of microbiome in central nervous system disorders. *Brain, behavior, and immunity*, 38:1–12, 2014.

[19] Jane A Foster and Karen-Anne McVey Neufeld. Gut–brain axis: how the microbiome influences anxiety and depression. *Trends in neurosciences*, 36(5):305–312, 2013.

[20] Livia H Morais, Henry L Schreiber IV, and Sarkis K Mazmanian. The gut microbiota–brain axis in behaviour and brain disorders. *Nature Reviews Microbiology*, 19(4):241–255, 2021.

[21] Emeran A Mayer, Kirsten Tillisch, Arpana Gupta, et al. Gut/brain axis and the microbiota. *The Journal of clinical investigation*, 125(3):926–938, 2015.

[22] Robert F Schwabe and Christian Jobin. The microbiome and cancer. *Nature Reviews Cancer*, 13(11):800–812, 2013.

[23] Erica V Harris, Jacobus C de Roode, and Nicole M Gerardo. Diet–microbiome–disease: Investigating diet's influence on infectious disease resistance through alteration of the gut microbiome. *PLoS pathogens*, 15(10):e1007891, 2019.

[24] Ruth E Ley, Fredrik Bäckhed, Peter Turnbaugh, Catherine A Lozupone, Robin D Knight, and Jeffrey I Gordon. Obesity alters gut microbial ecology. *Proceedings of the national academy of sciences*, 102(31):11070–11075, 2005.

[25] Anna M Seekatz, Johannes Aas, Charles E Gessert, Timothy A Rubin, Daniel M Saman, Johan S Bakken, and Vincent B Young. Recovery of the gut microbiome following fecal microbiota transplantation. *MBio*, 5(3):10–1128, 2014.

[26] Seon-Kyun Kim, Robin B Guevarra, You-Tae Kim, Joongi Kwon, Hyeri Kim, Jae Hyoung Cho, Hyeun Bum Kim, and Ju-Hoon Lee. Role of probiotics in human gut microbiome-associated diseases. *Journal of microbiology and biotechnology*, 29(9):1335–1340, 2019.

[27] Aymé Spor, Omry Koren, and Ruth Ley. Unravelling the effects of the environment and host genotype on the gut microbiome. *Nature Reviews Microbiology*, 9(4):279–290, 2011.

[28] Peter J Turnbaugh, Ruth E Ley, Micah Hamady, Claire M Fraser-Liggett, Rob Knight, and Jeffrey I Gordon. The human microbiome project. *Nature*, 449(7164):804–810, 2007.

[29] Rasnik K Singh, Hsin-Wen Chang, DI Yan, Kristina M Lee, Derya Ucmak, Kirsten Wong, Michael Abrouk, Benjamin Farahnik, Mio Nakamura, Tian Hao Zhu, et al. Influence of diet on the gut microbiome and implications for human health. *Journal of translational medicine*, 15:1–17, 2017.

[30] Lawrence A David, Arne C Materna, Jonathan Friedman, Maria I Campos-Baptista, Matthew C Blackburn, Allison Perrotta, Susan E Erdman, and Eric J Alm. Host lifestyle affects human microbiota on daily timescales. *Genome biology*, 15:1–15, 2014.

[31] Thomas Gensollen, Shankar S Iyer, Dennis L Kasper, and Richard S Blumberg. How colonization by microbiota in early life shapes the immune system. *Science*, 352(6285):539–544, 2016.

[32] The Human Microbiome Project Consortium. Structure, function and diversity of the healthy human microbiome. *nature*, 486(7402):207–214, 2012.

[33] Alan Aderem. Systems biology: its practice and challenges. *Cell*, 121(4):511–513, 2005.

[34] Xing Chen, Chenggang Clarence Yan, Xiaotian Zhang, Xu Zhang, Feng Dai, Jian Yin, and Yongdong Zhang. Drug–target interaction prediction: databases, web servers and computational models. *Briefings in bioinformatics*, 17(4):696–712, 2016.

[35] Samuel Chaffron, Hubert Rehrauer, Jakob Pernthaler, and Christian Von Mering. A global network of coexisting microbes from environmental and whole-genome sequence data. *Genome research*, 20(7):947–959, 2010.

[36] Georg K Gerber, Andrew B Onderdonk, and Lynn Bry. Inferring dynamic signatures of microbes in complex host ecosystems. *Plos Computational Biology*, 2012.

[37] Robert Marsland III, Wenping Cui, and Pankaj Mehta. A minimal model for microbial biodiversity can reproduce experimentally observed ecological patterns. *Scientific reports*, 10(1):3308, 2020.

[38] Megan Taylor and Nic Vega. Batching inflates error rates in microbial colonization of caenorhabditis elegans: an empirical investigation of the statistical properties of count-based data. *bioRxiv*, pages 2022–07, 2022.

[39] Mehdi Layeghifard, David M Hwang, and David S Guttman. Disentangling interactions in the microbiome: a network perspective. *Trends in microbiology*, 25(3):217–228, 2017.

[40] K Michael Martini, Satya Spandana Boddu, Megan N Taylor, Ilya Nemenman, and Nic M Vega. Correlations in microbial abundance data reveal host-bacteria and bacteria-bacteria interactions jointly shaping the c. elegans microbiome. *bioRxiv*, pages 2024–06, 2024.

[41] Georgii Frantsevich Gause. Experimental studies on the struggle for existence: I. mixed population of two species of yeast. *Journal of experimental biology*, 9(4):389–402, 1932.

[42] Yoav Ram, Eynat Dellus-Gur, Maayan Bibi, Kedar Karkare, Uri Obolski, Marcus W Feldman, Tim F Cooper, Judith Berman, and Lilach Hadany. Predicting microbial growth in a mixed culture from growth curve data. *Proceedings of the National Academy of Sciences*, 116(29):14698–14707, 2019.

[43] Katharine Z Coyte, Jonas Schluter, and Kevin R Foster. The ecology of the microbiome: networks, competition, and stability. *Science*, 350(6261):663–666, 2015.

[44] Jonathan Friedman, Logan M Higgins, and Jeff Gore. Community structure follows simple assembly rules in microbial microcosms. *Nature ecology & evolution*, 1(5):0109, 2017.

[45] Einat Nestor, Gal Toledano, and Jonathan Friedman. Interactions between culturable bacteria are predicted by individual species' growth. *Msystems*, 8(2):e00836–22, 2023.

[46] Joshua E Goldford, Nanxi Lu, Djordje Bajić, Sylvie Estrela, Mikhail Tikhonov, Alicia Sanchez-Gorostiaga, Daniel Segrè, Pankaj Mehta, and Alvaro Sanchez.

Emergent simplicity in microbial community assembly. *Science*, 361(6401):469–474, 2018.

[47] Alicia Sanchez-Gorostiaga, Djordje Bajić, Melisa L Osborne, Juan F Poyatos, and Alvaro Sanchez. High-order interactions distort the functional landscape of microbial consortia. *PLoS Biology*, 17(12):e3000550, 2019.

[48] Megan Taylor and NM Vega. Host immunity alters community ecology and stability of the microbiome in a caenorhabditis elegans model. *Msystems*, 6(2):10–1128, 2021.

[49] Adam R Burns, W Zac Stephens, Keaton Stagaman, Sandi Wong, John F Rawls, Karen Guillemin, and Brendan JM Bohannan. Contribution of neutral processes to the assembly of gut microbial communities in the zebrafish over host development. *The ISME journal*, 10(3):655–664, 2016.

[50] Ann K Corsi, Bruce Wightman, and Martin Chalfie. A transparent window into biology: a primer on caenorhabditis elegans. *Genetics*, 200(2):387–407, 2015.

[51] Arnaud Labrousse, Sophie Chauvet, Carole Couillault, C Léopold Kurz, and Jonathan J Ewbank. Caenorhabditis elegans is a model host for salmonella typhimurium. *Current biology*, 10(23):1543–1545, 2000.

[52] Lianne B Cohen and Emily R Troemel. Microbial pathogenesis and host defense in the nematode c. elegans. *Current opinion in microbiology*, 23:94–101, 2015.

[53] Laura C Clark and Jonathan Hodgkin. Commensals, probiotics and pathogens in the c aenorhabditis elegans model. *Cellular microbiology*, 16(1):27–38, 2014.

[54] Verónica Donato, Facundo Rodríguez Ayala, Sebastián Cogliati, Carlos Bauman, Juan Gabriel Costa, Cecilia Lenini, and Roberto Grau. Bacillus subtilis

biofilm extends caenorhabditis elegans longevity through downregulation of the insulin-like signalling pathway. *Nature communications*, 8(1):14332, 2017.

[55] Philipp Dirksen, Sarah Arnaud Marsh, Ines Braker, Nele Heitland, Sophia Wagner, Rania Nakad, Sebastian Mader, Carola Petersen, Vienna Kowallik, Philip Rosenstiel, et al. The native microbiome of the nematode caenorhabditis elegans: gateway to a new host-microbiome model. *BMC biology*, 14:1–16, 2016.

[56] Maureen Berg, Xiao Ying Zhou, and Michael Shapira. Host-specific functional significance of caenorhabditis gut commensals. *Frontiers in microbiology*, 7:1622, 2016.

[57] Buck S Samuel, Holli Rowedder, Christian Braendle, Marie-Anne Félix, and Gary Ruvkun. Caenorhabditis elegans responses to bacteria from its natural habitats. *Proceedings of the National Academy of Sciences*, 113(27):E3941–E3949, 2016.

[58] Megan N Taylor, Satya Spandana Boddu, and Nic M Vega. Using single-worm data to quantify heterogeneity in caenorhabditis elegans-bacterial interactions. *JoVE (Journal of Visualized Experiments)*, (185):e64027, 2022.

[59] David W Armitage and Stuart E Jones. How sample heterogeneity can obscure the signal of microbial interactions. *The ISME journal*, 13(11):2639–2646, 2019.

[60] Jessica F Stephenson, Kyle A Young, Jordan Fox, Jukka Jokela, Joanne Cable, and Sarah E Perkins. Host heterogeneity affects both parasite transmission to and fitness on subsequent hosts. *Philosophical Transactions of the Royal Society B: Biological Sciences*, 372(1719):20160093, 2017.

[61] Kimberly L VanderWaal and Vanessa O Ezenwa. Heterogeneity in pathogen transmission. *Functional Ecology*, 30(10):1606–1622, 2016.

[62] Greg Dwyer, Joseph S Elkinton, and John P Buonaccorsi. Host heterogeneity in susceptibility and disease dynamics: tests of a mathematical model. *The American Naturalist*, 150(6):685–707, 1997.

[63] Deqing Wu, Shane L Rea, Anatoli I Yashin, and Thomas E Johnson. Visualizing hidden heterogeneity in isogenic populations of c. elegans. *Experimental gerontology*, 41(3):261–270, 2006.

[64] Anatoli I Yashin, James W Cypser, Thomas E Johnson, Anatoli I Michalski, Sergei I Boyko, and Vasili N Novoseltsev. Heat shock changes the heterogeneity distribution in populations of caenorhabditis elegans: does it tell us anything about the biological mechanism of stress response? *The Journals of Gerontology Series A: Biological Sciences and Medical Sciences*, 57(3):B83–B92, 2002.

[65] Yuan Zhao, Ann F Gilliat, Matthias Ziehm, Mark Turmaine, Hongyuan Wang, Marina Ezcurra, Chenhao Yang, George Phillips, David McBay, William B Zhang, et al. Two forms of death in ageing caenorhabditis elegans. *Nature communications*, 8(1):15458, 2017.

[66] D Mark Eckley, Salim Rahimi, Sandra Mantilla, Nikita V Orlov, Christopher E Coletta, Mark A Wilson, Wendy B Iser, John D Delaney, Yongqing Zhang, William Wood, et al. Molecular characterization of the transition to mid-life in caenorhabditis elegans. *Age*, 35:689–703, 2013.

[67] Shane L Rea, Deqing Wu, James R Cypser, James W Vaupel, and Thomas E Johnson. A stress-sensitive reporter predicts longevity in isogenic populations of caenorhabditis elegans. *Nature genetics*, 37(8):894–898, 2005.

[68] Holly E Kinser, Matthew C Mosley, Isaac B Plutzer, and Zachary Pincus. Global, cell non-autonomous gene regulation drives individual lifespan among isogenic c. elegans. *Elife*, 10:e65026, 2021.

[69] Matthew A Churgin, Sang-Kyu Jung, Chih-Chieh Yu, Xiangmei Chen, David M Raizen, and Christopher Fang-Yen. Longitudinal imaging of caenorhabditis elegans in a microfabricated device reveals variation in behavioral decline during aging. *Elife*, 6:e26652, 2017.

[70] Marcos Francisco Perez, Mirko Francesconi, Cristina Hidalgo-Carcedo, and Ben Lehner. Maternal age generates phenotypic variation in caenorhabditis elegans. *Nature*, 552(7683):106–109, 2017.

[71] Simon Baeriswyl, Médéric Diard, Thomas Mosser, Magali Leroy, Xavier Maniere, François Taddei, and Ivan Matic. Modulation of aging profiles in isogenic populations of caenorhabditis elegans by bacteria causing different extrinsic mortality rates. *Biogerontology*, 11(1):53–65, 2010.

[72] S Anaid Diaz and Olivier Restif. Spread and transmission of bacterial pathogens in experimental populations of the nematode caenorhabditis elegans. *Applied and environmental microbiology*, 80(17):5411–5418, 2014.

[73] Kwame Twumasi-Boateng, Maureen Berg, and Michael Shapira. Automated separation of c. elegans variably colonized by a bacterial pathogen. *JoVE (Journal of Visualized Experiments)*, (85):e51090, 2014.

[74] Maureen Berg, David Monnin, Juhyun Cho, Lydia Nelson, Alex Crits-Christoph, and Michael Shapira. Tgfβ/bmp immune signaling affects abundance and function of c. elegans gut commensals. *Nature communications*, 10(1):604, 2019.

[75] Cynthia Portal-Celhay and Martin J Blaser. Competition and resilience between founder and introduced bacteria in the caenorhabditis elegans gut. *Infection and immunity*, 80(3):1288–1299, 2012.

[76] Euan Scott, Lindy Holden-Dye, Vincent O'Connor, and Matthew E Wand. Intra strain variation of the effects of gram-negative eskape pathogens on intestinal colonization, host viability, and host response in the model organism caenorhabditis elegans. *Frontiers in Microbiology*, 10:496344, 2020.

[77] RS Kamath. Effectiveness of specific rna-mediated interference through ingested double-stranded rna in caenorhabditis elegans. *Genome Biology*, 16:1, 2015.

[78] Nicole M Vega, Kyle R Allison, Amanda N Samuels, Mark S Klempner, and James J Collins. Salmonella typhimurium intercepts escherichia coli signaling to enhance antibiotic tolerance. *Proceedings of the National Academy of Sciences*, 110(35):14420–14425, 2013.

[79] Theresa Stiernagle. Maintenance of c. elegans. *WormBook: The online review of C. elegans biology [Internet]*, 2006.

[80] Hiroaki Tabara, Madathia Sarkissian, William G Kelly, Jamie Fleenor, Alla Grishok, Lisa Timmons, Andrew Fire, and Craig C Mello. The rde-1 gene, rna interference, and transposon silencing in c. elegans. *Cell*, 99(2):123–132, 1999.

[81] Julie Ahringer. Reverse genetics. In *WormBook: The Online Review of C. elegans Biology [Internet]*. WormBook, 2006.

[82] Jean-François Rual, Julian Ceron, John Koreth, Tong Hao, Anne-Sophie Nicot, Tomoko Hirozane-Kishikawa, Jean Vandenhaute, Stuart H Orkin, David E Hill, Sander van den Heuvel, et al. Toward improving caenorhabditis elegans phenome mapping with an orfeome-based rnai library. *Genome research*, 14(10b):2162–2168, 2004.

[83] Alexey V Revtovich, Elissa Tjahjono, Kavindra V Singh, Blake M Hanson, Barbara E Murray, and Natalia V Kirienko. Development and characterization of

high-throughput caenorhabditis elegans–enterococcus faecium infection model. *Frontiers in Cellular and Infection Microbiology*, 11:667327, 2021.

[84] Quinton L Anderson, Alexey V Revtovich, and Natalia V Kirienko. A high-throughput, high-content, liquid-based c. elegans pathosystem. *JoVE (Journal of Visualized Experiments)*, (137):e58068, 2018.

[85] Monika Scholz, Aaron R Dinner, Erel Levine, and David Biron. Stochastic feeding dynamics arise from the need for information and energy. *Proceedings of the National Academy of Sciences*, 114(35):9261–9266, 2017.

[86] Taihong Wu, Fengyun Duan, Wenxing Yang, He Liu, Antonio Caballero, Diana Andrea Fernandes de Abreu, Abdul Rouf Dar, Joy Alcedo, QueeLim Ch'ng, Rebecca A Butcher, et al. Pheromones modulate learning by regulating the balanced signals of two insulin-like peptides. *Neuron*, 104(6):1095–1109, 2019.

[87] Tsui-Ting Ching and Ao-Lin Hsu. Solid plate-based dietary restriction in caenorhabditis elegans. *JoVE (Journal of Visualized Experiments)*, (51):e2701, 2011.

[88] Alyssa C Walker, Rohan Bhargava, Alfonso S Vaziriyan-Sani, Amanda S Brust, and Daniel M Czyz. Quantification of bacterial loads in caenorhabditis elegans. *Bio-protocol*, 12(2):e4291–e4291, 2022.

[89] Jacob R Manjarrez and Roger Mailler. Stress and timing associated with caenorhabditis elegans immobilization methods. *Heliyon*, 6(7), 2020.

[90] Sihui Zhang, Diya Banerjee, and Jeffrey R Kuhn. Isolation and culture of larval cells from c. elegans. *PloS one*, 6(4):e19505, 2011.

[91] Danielle A Garsin, Jacinto M Villanueva, Jakob Begun, Dennis H Kim, Costi D Sifri, Stephen B Calderwood, Gary Ruvkun, and Frederick M Ausubel. Long-

lived c. elegans daf-2 mutants are resistant to bacterial pathogens. *Science*, 300(5627):1921–1921, 2003.

[92] Shashi Thutupalli, Sravanti Uppaluri, George WA Constable, Simon A Levin, Howard A Stone, Corina E Tarnita, and Clifford P Brangwynne. Farming and public goods production in caenorhabditis elegans populations. *Proceedings of the National Academy of Sciences*, 114(9):2289–2294, 2017.

[93] Kien Ly, Suzanne J Reid, and Russell G Snell. Rapid rna analysis of individual caenorhabditis elegans. *MethodsX*, 2:59–63, 2015.

[94] Julia Johnke, Philipp Dirksen, and Hinrich Schulenburg. Community assembly of the native c. elegans microbiome is influenced by time, substrate and individual bacterial taxa. *Environmental Microbiology*, 22(4):1265–1279, 2020.

[95] Leah Gulyas and Jennifer R Powell. Cold shock induces a terminal investment reproductive response in c. elegans. *Scientific Reports*, 12(1):1338, 2022.

[96] Wei Jiang, Yuehua Wei, Yong Long, Arthur Owen, Bingying Wang, Xuebing Wu, Shuo Luo, Yongjun Dang, and Dengke K Ma. A genetic program mediates cold-warming response and promotes stress-induced phenoptosis in c. elegans. *Elife*, 7:e35037, 2018.

[97] Joseph D Robinson and Jennifer R Powell. Long-term recovery from acute cold shock in caenorhabditis elegans. *BMC cell biology*, 17:1–11, 2016.

[98] K Michael Martini, Satya Spandana Boddu, Ilya Nemenman, and Nic M Vega. Maximum likelihood estimators for colony-forming units. *Microbiology Spectrum*, 12(9):e03946–23, 2024.

[99] Mac H McCrady. The numerical interpretation of fermentation-tube results. *The Journal of Infectious Diseases*, pages 183–212, 1915.

[100] William G Cochran. Estimation of bacterial densities by means of the" most probable number". *Biometrics*, 6(2):105–116, 1950.

[101] Robert S Breed and WD Dotterrer. The number of colonies allowable on satisfactory agar plates. *Journal of bacteriology*, 1(3):321–331, 1916.

[102] RA Fisher, HG Thornton, and WA Mackenzie. The accuracy of the plating method of estimating the density of bacterial populations: With particular reference to the use of thornton's agar medium with soil samples. *Annals of Applied Biology*, 9(3-4):325–359, 1922.

[103] HO Halvorson and NR Ziegler. Application of statistics to problems in bacteriology: I. a means of determining bacterial population by the dilution method. *Journal of Bacteriology*, 25(2):101–121, 1933.

[104] Marshall W Jennison and George P Wadsworth. Evaluation of the errors involved in estimating bacterial numbers by the plating method. *Journal of Bacteriology*, 39(4):389–397, 1940.

[105] PCT Jones, JE Mollison, and MH Quenouille. A technique for the quantitative estimation of soil micro-organisms: With a statistical note by. *Microbiology*, 2(1):54–69, 1948.

[106] FA Skinner, PCT Jones, and JE Mollison. A comparison of a direct-and a plate-counting technique for the quantitative estimation of soil micro-organisms. *Microbiology*, 6(3-4):261–271, 1952.

[107] Eugene A Johnson and Byron Wm Brown Jr. The spearman estimator for serial dilution assays. *Biometrics*, pages 79–88, 1961.

[108] J Taylor. The estimation of numbers of bacteria by tenfold dilution series. *Journal of Applied Bacteriology*, 25(1):54–61, 1962.

[109] RF Harris and LE Sommers. Plate-dilution frequency technique for assay of microbial ecology. *Applied microbiology*, 16(2):330–334, 1968.

[110] Harold A Thomas Jr and Richard L Woodward. Estimation of coliform density by the membrane filter and the fermentation tube methods. *American Journal of Public Health and the Nations Health*, 45(11):1431–1437, 1955.

[111] Wesley O Pipes, Pamela Ward, and SH Ahn. Frequency distributions for coliform bacteria in water. *Journal (American Water Works Association)*, pages 664–668, 1977.

[112] Daniel G Horvitz and Donovan J Thompson. A generalization of sampling without replacement from a finite universe. *Journal of the American statistical Association*, 47(260):663–685, 1952.

[113] Margaret A Hurley and ME Roscoe. Automated statistical analysis of microbial enumeration by dilution series. *Journal of applied bacteriology*, 55(1):159–164, 1983.

[114] D Kirchman, J Sigda, R Kapuscinski, and R Mitchell. Statistical analysis of the direct count method for enumerating bacteria. *Applied and Environmental Microbiology*, 44(2):376–382, 1982.

[115] Avishai Ben-David and Charles E Davidson. Estimation method for serial dilution experiments. *Journal of microbiological methods*, 107:214–221, 2014.

[116] Charles N. Haas, Joan B. Rose, and Charles P. Gerba. Exposure Assessment. In *Quantitative Microbial Risk Assessment*, pages 159–234. John Wiley & Sons, Ltd, 2014. Section: 6 _eprint: https://onlinelibrary.wiley.com/doi/pdf/10.1002/9781118910030.ch6.

[117] J Andrés Christen and Albert E Parker. Systematic statistical analysis of microbial data from dilution series. *Journal of Agricultural, Biological and Environmental Statistics*, 25(3):339–364, 2020.

[118] CHARLES N Haas and BARBARA Heller. Averaging of tntc counts. *Applied and environmental microbiology*, 54(8):2069–2072, 1988.

[119] Alan J Hedges. Estimating the precision of serial dilutions and viable bacterial counts. *International journal of food microbiology*, 76(3):207–214, 2002.

[120] Janet EL Corry, Basil Jarvis, Sue Passmore, and Alan Hedges. A critical review of measurement uncertainty in the enumeration of food micro-organisms. *Food microbiology*, 24(3):230–253, 2007.

[121] AH El-Shaarawi, SR Esterby, and BJ Dutka. Bacterial density in water determined by poisson or negative binomial distributions. *Applied and Environmental Microbiology*, 41(1):107–116, 1981.

[122] A. H. Havelaar, W. M. Hogeboom, V. M. Sekhuis, and E. H. W. VAN Erne. Proficiency testing of water microbiology laboratories in The Netherlands. *Journal of Applied Bacteriology*, 62(6):555–564, 1987.

[123] Salvador E Luria and Max Delbrück. Mutations of bacteria from virus sensitivity to virus resistance. *Genetics*, 28(6):491, 1943.

[124] CHARLES N Haas and B Heller. Test of the validity of the poisson assumption for analysis of most-probable-number results. *Applied and Environmental Microbiology*, 54(12):2996–3002, 1988.

[125] Basil Jarvis, Alan J Hedges, and Janet EL Corry. The contribution of sampling uncertainty to total measurement uncertainty in the enumeration of microorganisms in foods. *Food microbiology*, 30(2):362–371, 2012.

[126] G. H. Weenk. Microbiological assessment of culture media: comparison and statistical evaluation of methods. *International Journal of Food Microbiology*, 17(2):159–181, October 1992.

[127] Scott Sutton. Accuracy of plate counts. *Journal of validation technology*, 17(3):42–46, 2011.

[128] K. Michael Martini. Calculate colony forming units (cfus), 2023.

[129] Robert Blodgett. Bam appendix 2: Most probable number from serial dilutions, 2020.

[130] Churchill Eisenhart and Perry W Wilson. Statistical methods and control in bacteriology. *Bacteriological Reviews*, 7(2):57–137, 1943.

[131] USDA. Quantitative analysis of bacteria in foods as sanitary indicators, 2015.

[132] Robert A. Canales, Amanda M. Wilson, Jennifer I. Pearce-Walker, Marc P. Verhougstraete, and Kelly A. Reynolds. Methods for Handling Left-Censored Data in Quantitative Microbial Risk Assessment. *Applied and Environmental Microbiology*, 84(20):e01203–18, October 2018. Publisher: American Society for Microbiology.

[133] Irène Gijbels. Censored data. *WIREs Computational Statistics*, 2(2):178–188, 2010. _eprint: https://onlinelibrary.wiley.com/doi/pdf/10.1002/wics.80.

[134] CESER EPA. Evaluation of Options for Interpreting Environmental Microbiology Field Data Results having Low Spore Counts. Technical Report EPA/600/R-14/331, Environmental Protection Agency, 2014.

[135] Martin Alexander. Most probable number method for microbial populations. *Methods of Soil Analysis: Part 2 Chemical and Microbiological Properties*, 9:815–820, 1983.

[136] KR Clarke and NJP Owens. A simple and versatile micro-computer program for the determination of 'most probable number'. *Journal of Microbiological Methods*, 1(3):133–137, 1983.

[137] Ibrahim A. Salama, Gary G. Koch, and Dennis H. Tolley. On the estimation of the most probable number in a serial dilution experiment. *Communications in Statistics - Theory and Methods*, 7(13):1267–1281, January 1978. Publisher: Taylor & Francis _eprint: https://doi.org/10.1080/03610927808827710.

[138] Sarah C Tremaine and Aaron L Mills. Tests of the critical assumptions of the dilution method for estimating bacterivory by microeucaryotes. *Applied and environmental microbiology*, 53(12):2914–2921, 1987.

[139] Andrew D Gronewold and Robert L Wolpert. Modeling the relationship between most probable number (mpn) and colony-forming unit (cfu) estimates of fecal coliform concentration. *Water research*, 42(13):3327–3334, 2008.

[140] Basil Jarvis, Alan J Hedges, and Janet EL Corry. Assessment of measurement uncertainty for quantitative methods of analysis: comparative assessment of the precision (uncertainty) of bacterial colony counts. *International journal of food microbiology*, 116(1):44–51, 2007.

[141] B Jarvis, JEL Corry, and AJ Hedges. Estimates of measurement uncertainty from proficiency testing schemes, internal laboratory quality monitoring and during routine enforcement examination of foods. *Journal of applied microbiology*, 103(2):462–267, 2007.

[142] Basil Jarvis. *Statistical aspects of the microbiological examination of foods*. Academic Press, 2016.

[143] Frank Fenner. The Enumeration of Viable Tubercle Bacilli by Surface Plate

Counts. *American Review of Tuberculosis*, 64(4):353–380, October 1951. Publisher: American Thoracic Society - AJRCCM.

[144] A. N Hassan and J. F Frank. Influence of surfactant hydrophobicity on the detachment of Escherichia coli O157:H7 from lettuce. *International Journal of Food Microbiology*, 87(1):145–152, October 2003.

[145] Wallace E Garthright. Bias in the logarithm of microbial density estimates from serial dilutions. *Biometrical Journal*, 35(3):299–314, 1993.

[146] Milton W. Loyer and Martin A. Hamilton. Interval estimation of the density of organisms using a serial-dilution experiment. *Biometrics*, 40(4):907–916, December 1984. MAG ID: 2317336612.

[147] Pei-Ju Chiang, Min-Jen Tseng, Zong-Sian He, and Chia-Hsun Li. Automated counting of bacterial colonies by image analysis. *Journal of microbiological methods*, 108:74–82, 2015.

[148] Silvio D Brugger, Christian Baumberger, Marcel Jost, Werner Jenni, Urs Brugger, and Kathrin Mühlemann. Automated counting of bacterial colony forming units on agar plates. *PloS one*, 7(3):e33695, 2012.

[149] JM Bewes, N Suchowerska, and DR McKenzie. Automated cell colony counting and analysis using the circular hough image transform algorithm (chita). *Physics in Medicine & Biology*, 53(21):5991, 2008.

[150] George M. Savage and H. O. Halvorson. The Effect of Culture Environment on Results Obtained with the Dilution Method of Determining Bacterial Population. *Journal of Bacteriology*, 41(3):355–362, March 1941. MAG ID: 108945167.

[151] Jeremy M. Chacón, Wolfram Möbius, and William R. Harcombe. The spatial

and metabolic basis of colony size variation. *The ISME Journal*, 12(3):669–680, March 2018.

[152] Leo WG Strijbosch, Wim A Buurman, Ronald JMM Does, Piet H Zinken, and Gerard Groenewegen. Limiting dilution assays: experimental design and statistical analysis. *Journal of immunological methods*, 97(1):133–140, 1987.

[153] Georg K Gerber. The dynamic microbiome. *FEBS letters*, 588(22):4131–4139, 2014.

[154] Kathryn J Pflughoeft and James Versalovic. Human microbiome in health and disease. *Annual Review of Pathology: Mechanisms of Disease*, 7(1):99–122, 2012.

[155] J Gregory Caporaso, Christian L Lauber, Elizabeth K Costello, Donna Berg-Lyons, Antonio Gonzalez, Jesse Stombaugh, Dan Knights, Pawel Gajer, Jacques Ravel, Noah Fierer, et al. Moving pictures of the human microbiome. *Genome biology*, 12:1–8, 2011.

[156] June L Round and Sarkis K Mazmanian. The gut microbiota shapes intestinal immune responses during health and disease. *Nature reviews immunology*, 9(5):313–323, 2009.

[157] Travis J Wiles, Matthew Jemielita, Ryan P Baker, Brandon H Schlomann, Savannah L Logan, Julia Ganz, Ellie Melancon, Judith S Eisen, Karen Guillemin, and Raghuveer Parthasarathy. Host gut motility promotes competitive exclusion within a model intestinal microbiota. *PLoS biology*, 14(7):e1002517, 2016.

[158] Marc Jan Bonder, Alexander Kurilshikov, Ettje F Tigchelaar, Zlatan Mujagic, Floris Imhann, Arnau Vich Vila, Patrick Deelen, Tommi Vatanen, Melanie Schirmer, Sanne P Smeekens, et al. The effect of host genetics on the gut microbiome. *Nature genetics*, 48(11):1407–1412, 2016.

[159] Maureen Berg, Ben Stenuit, Joshua Ho, Andrew Wang, Caitlin Parke, Matthew Knight, Lisa Alvarez-Cohen, and Michael Shapira. Assembly of the Caenorhabditis elegans gut microbiota from diverse soil microbial environments. *The ISME Journal*, 10(8):1998–2009, August 2016.

[160] Maureen Berg, Xiao Ying Zhou, and Michael Shapira. Host-Specific Functional Significance of Caenorhabditis Gut Commensals. *Frontiers in Microbiology*, 7, 2016.

[161] Megan N. Taylor and N. M. Vega. Host Immunity Alters Community Ecology and Stability of the Microbiome in a Caenorhabditis elegans Model. *mSystems*, 6(2), April 2021.

[162] Nic M. Vega. Heterogeneous shedding and susceptibility in a Caenorhabditis elegans transmission model, June 2024.

[163] A. M. Kilpatrick and A. R. Ives. Species interactions can explain Taylor's power law for ecological time series. *Nature*, 422(6927):65–68, March 2003.

[164] Megan N. Taylor and N. M. Vega. Sample pooling inflates error rates in between-sample comparisons: an empirical investigation of the statistical properties of count-based data, February 2024.

[165] Daniel T Gillespie. A general method for numerically simulating the stochastic time evolution of coupled chemical reactions. *Journal of computational physics*, 22(4):403–434, 1976.

[166] Daniel T Gillespie. Exact stochastic simulation of coupled chemical reactions. *The journal of physical chemistry*, 81(25):2340–2361, 1977.

[167] Hitoshi Suda, Tetsuji Shoyama, and Yuka Shimizu. Analyzing observed or

hidden heterogeneity on survival and mortality in an isogenic C. elegans cohort. *Biophysics*, 5:59–66, 2009.

[168] Gunalan Natesan, Timothy Hamilton, Eric J. Deeds, and Pavak K. Shah. Novel metrics reveal new structure and unappreciated heterogeneity in Caenorhabditis elegans development. *PLOS Computational Biology*, 19(12):e1011733, December 2023. Publisher: Public Library of Science.

[169] Nadia Vertti-Quintero, Simon Berger, Xavier Casadevall i Solvas, Cyril Statzer, Jillian Annis, Peter Ruppen, Stavros Stavrakis, Collin Y. Ewald, Rudiyanto Gunawan, and Andrew J. deMello. Stochastic and Age-Dependent Proteostasis Decline Underlies Heterogeneity in Heat-Shock Response Dynamics. *Small*, 17(30):2102145, 2021. _eprint: https://onlinelibrary.wiley.com/doi/pdf/10.1002/smll.202102145.

[170] Deqing Wu, Shane L. Rea, Anatoli I. Yashin, and Thomas E. Johnson. Visualizing hidden heterogeneity in isogenic populations of C. elegans. *Experimental Gerontology*, 41(3):261–270, March 2006.

[171] Anatoli I. Yashin, James W. Cypser, Thomas E. Johnson, Anatoli I. Michalski, Sergei I. Boyko, and Vasili N. Novoseltsev. Heat Shock Changes the Heterogeneity Distribution in Populations of Caenorhabditis elegans Does It Tell Us Anything About the Biological Mechanism of Stress Response? *The Journals of Gerontology Series A: Biological Sciences and Medical Sciences*, 57(3):B83–B92, March 2002.

[172] Liyang Zhang, Vyshnavi Gade, and Natalia V. Kirienko. Pathogen-induced dormancy in liquid limits gastrointestinal colonization of Caenorhabditis elegans. *Virulence*, 14(1):2204004, December 2023.

[173] Terence I. Moy, Anthony R. Ball, Zafia Anklesaria, Gabriele Casadei, Kim

Lewis, and Frederick M. Ausubel. Identification of novel antimicrobials using a live-animal infection model. *Proceedings of the National Academy of Sciences*, 103(27):10414–10419, July 2006.

[174] Marcel H Zwietering, Ida Jongenburger, Frank M Rombouts, and KJAEM Van't Riet. Modeling of the bacterial growth curve. *Applied and environmental microbiology*, 56(6):1875–1881, 1990.

[175] Michael J Taormina, Matthew Jemielita, W Zac Stephens, Adam R Burns, Joshua V Troll, Raghuveer Parthasarathy, and Karen Guillemin. Investigating bacterial-animal symbioses with light sheet microscopy. *The Biological Bulletin*, 223(1):7–20, 2012.

[176] Vittorio Viri, Matteo Cornaglia, Huseyin Baris Atakan, Thomas Lehnert, and Martin AM Gijs. An in vivo microfluidic study of bacterial transit in c. elegans nematodes. *Lab on a Chip*, 20(15):2696–2708, 2020.

[177] Vittorio Viri, Maël Arveiler, Thomas Lehnert, and Martin AM Gijs. An in vivo microfluidic study of bacterial load dynamics and absorption in the c. elegans intestine. *Micromachines*, 12(7):832, 2021.

[178] Sean P Leonard, Jiri Perutka, J Elijah Powell, Peng Geng, Darby D Richhart, Michelle Byrom, Shaunak Kar, Bryan W Davies, Andrew D Ellington, Nancy A Moran, et al. Genetic engineering of bee gut microbiome bacteria with a toolkit for modular assembly of broad-host-range plasmids. *ACS synthetic biology*, 7(5):1279–1290, 2018.

[179] Pauli Virtanen, Ralf Gommers, Travis E. Oliphant, Matt Haberland, Tyler Reddy, David Cournapeau, Evgeni Burovski, Pearu Peterson, Warren Weckesser, Jonathan Bright, Stéfan J. van der Walt, Matthew Brett, Joshua Wilson, K. Jarrod Millman, Nikolay Mayorov, Andrew R. J. Nelson, Eric Jones,

Robert Kern, Eric Larson, C J Carey, İlhan Polat, Yu Feng, Eric W. Moore, Jake VanderPlas, Denis Laxalde, Josef Perktold, Robert Cimrman, Ian Henriksen, E. A. Quintero, Charles R. Harris, Anne M. Archibald, Antônio H. Ribeiro, Fabian Pedregosa, Paul van Mulbregt, and SciPy 1.0 Contributors. SciPy 1.0: Fundamental Algorithms for Scientific Computing in Python. *Nature Methods*, 17:261–272, 2020.

[180] F. Pedregosa, G. Varoquaux, A. Gramfort, V. Michel, B. Thirion, O. Grisel, M. Blondel, P. Prettenhofer, R. Weiss, V. Dubourg, J. Vanderplas, A. Passos, D. Cournapeau, M. Brucher, M. Perrot, and E. Duchesnay. Scikit-learn: Machine learning in Python. *Journal of Machine Learning Research*, 12:2825–2830, 2011.

[181] Nicolaas Godfried Van Kampen. *Stochastic processes in physics and chemistry*, volume 1. Elsevier, 1992.

[182] Yuya Kiyama, Kohji Miyahara, and Yasumi Ohshima. Active uptake of artificial particles in the nematode Caenorhabditis elegans. *Journal of Experimental Biology*, 215(7):1178–1183, April 2012.

[183] H. Risken. *The Fokker-Planck Equation: Methods of Solution and Applications*. Springer Science & Business Media, 1996.